Solid-state NMR Spectroscopic, X-Ray Diffraction and Quantum Chemical Investigations of the Crystalline Cancer Drug Paclitaxel and Paclitaxel incorporated into Polymer Micelles

Dissertation zur Erlangung des naturwissenschaftlichen Doktorgrades der Julius-Maximilians-Universität Würzburg

vorgelegt von

Marvin Grüne

aus Münster (Westfalen)

Würzburg 2020

Eingereicht bei der Fakultät für Chemie und Pharmazie am

21.12.2020

Gutachter der schriftlichen Arbeit

1. Gutachter: _____
2. Gutachter: _____

Prüfer des öffentlichen Promotionskolloquiums

1. Prüfer: _____
2. Prüfer: _____
3. Prüfer: _____

Datum des öffentlichen Promotionskolloquiums

_____

Doktorurkunde ausgehändigt am

_____

Acknowledgements

At the very beginning and most of all, I would like to thank Jun.-Prof. Dr. Ann-Christin Pöppler for giving me the opportunity to investigate this fascinating topic during the last years. I really appreciate your trust in me to support you and contribute to build up the research group as your first PhD student. At all times, you have given me the freedom to choose the thematic and scientific direction for my work and was always there with advice and support when I needed help or discussion again. I am also very grateful for all the opportunities you have given me to attend numerous conferences and workshops and to participate in collaborations both in Germany and abroad.

Furthermore, I would like to express my great thanks to Prof. Dr. Robert Luxenhofer. From the very beginning, you enthusiastically supported me as a second supervisor with words and deeds. Over the years, you have followed each of my new findings with fascination, critically questioned them and, with the discussions, again laid down new signposts.

Many thanks also to my colleagues in the working group with whom I had the opportunity to work over the last few years. Coming to the office or the lab was a pleasure every day because of you. Special thanks to Sebastian Endres and Sebastian Scheidel, we were the best team together since day one.

A big thank you also goes to Prof. Dr. Steven Brown and Dr. Dinu Iuga from the University of Warwick, UK. During the scientific exchange with you over the last years, I have learned a lot in the field of research, publishing, and solid-state NMR. Also, thank you for patiently teaching me how to use all the new equipment and taking care of me during my multiple visits to your labs, be it the matters of 1.3 mm MAS rotor size or of the hardware of large high field NMR spectrometers.

Furthermore, I would like to thank Dr. Michael Lübtow for providing the different formulations which I was joyfully investigating. You always had time and an ear for dicussions regarding the evaluations.

I also want to say thank you to Dominik Heuler. The cooperation with you regarding the PTX project has always been a great enrichment.

Finally, I would like to thank from the bottom of my heart my girlfriend, my family, and my friends for their endless support!

Contents

Introduction

Currently, one of the most important and relevant drugs to combat breast and ovarian cancer is paclitaxel (PTX, $C_{47}H_{51}NO_{14}$, also named Taxol, see **Scheme 1**), which is known since the 1960s.[1] While its efficiency to combat breast and ovarian cancers is already established, it is currently also undergoing clinical trials for use against other types of cancer.[2] The mechanism of action of PTX includes blocking of the attacked cell in the mitotic phase by stabilizing the microtubule cytoskeleton.[3] Like many anti-cancer drugs, its poor aqueous solubility has been limiting its use.[4] Therefore, an efficient mechanism has to be found to bring PTX in sufficient concentration to the tumour. Several basic ideas and concepts exist to transport a drug to its site of action, which are summarized chronologically below in the form of a "History of drug delivery".
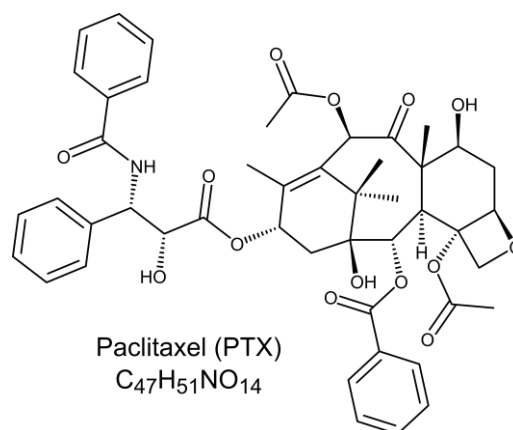
Scheme 1: Structural formula of paclitaxel (PTX).

History of drug delivery

Since 1980, the field of drug delivery research has grown exponentially until it reached its peak in 2013 with more than 450.000 publications per year (Google Scholar). Since then, the number of publications per year has been declining at almost the same rate as the previous increase. Another interesting aspect in this respect is the number of patents per year regarding drug delivery. Both the "number of publications" and the "number of publications per patent applied for" are shown in **Figure 1** for each year. The question now is:

"Are we on a downward trend? Is the field of drug delivery no longer of interest for research?"
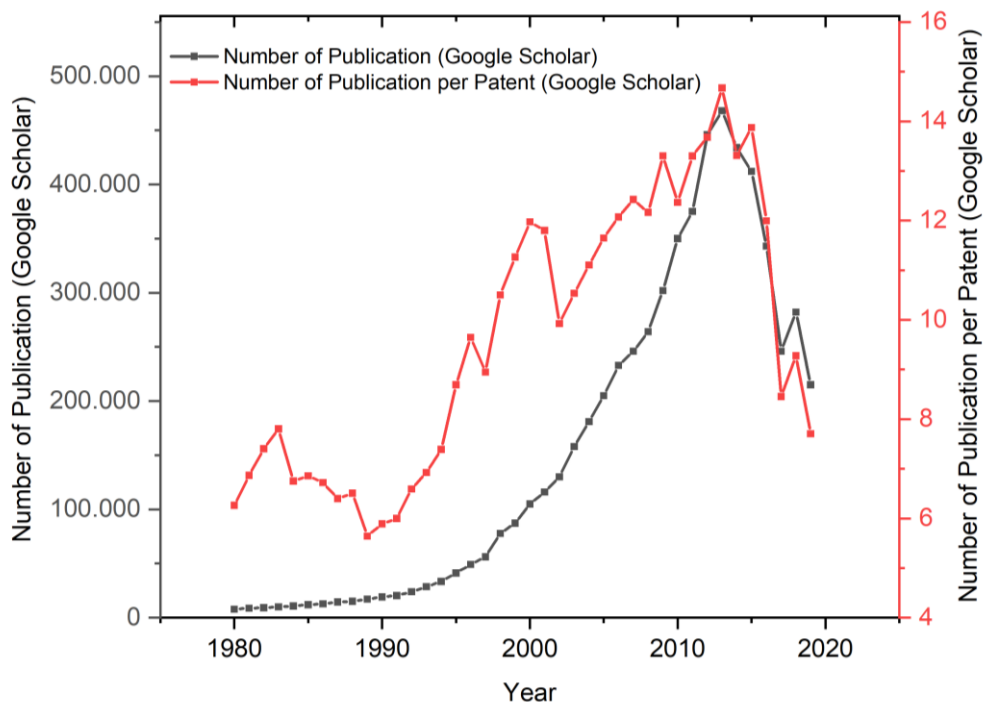
Figure 1: Graphic representation of the course of the number of publications (black) as well as the number of publications per patent (red) per year in the field of drug delivery. The results are based on a Google Scholar search (October 2020) with the terms "drug delivery" and "drug delivery patent".

Despite the declining trend, in 2018 the FDA has broken its record of the year 1996 (53 approved drugs) with 59 newly approved drugs.[5] However, as can be seen from the reference, the number of approved drugs fluctuates between 20 and 60.

This introductory chapter is intended to present the "history of drug delivery" from a starting point around the 4th century. This should lead to show why, despite the figures just presented, work on an anti-cancer drug, namely PTX, incorporated into polymeric micelles is even more important and the field of research more topical than ever.

The long evolution of nanomaterials for drug delivery

Figure 2: Historical timelines of important developments and milestones in the field of nanomaterials. Reprinted with permission from ref [6]. Copyright 2007 Elsevier.
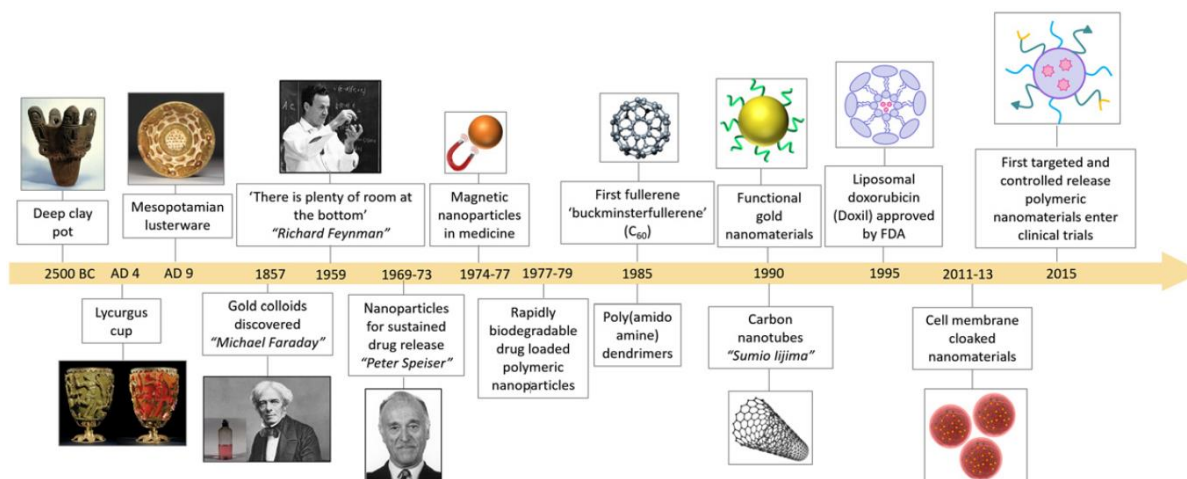
Approximately 40 % of the currently marketed drugs[7] and even up to 75 % of the compounds under development[8] display poor aqueous solubility.[9] It is therefore obvious that one of the main focuses of research must be to circumvent this problem of low water solubility of the hydrophobic components by means of suitable excipients to increase the bioavailability of these drugs. To overcome this issue, a variety of approaches have been developed including amorphous forms, polymorphs, salts and co-crystals.[10] Other promising possibilities to improve the solubility or alter physicochemical properties are the use of polymer-drug conjugates, liposomes, dendrimers and micelles.[11] A common property of these materials is their size in the order of nanometres. Therefore, they are part of a field of drug delivery in the superordinate term of "nanomedicine".

The first mention by name of this concept dates back to a publication in 1999.[12] However, the fascination for nanomaterials goes back to the 25th century before Christ and is shown in **Figure 2** which illustrates a timeline with several important developments in the field of nanomedicine.[6] Back in the 4th century AD, the Romans created the famous Lycurgus cup. The glass of the cup is dichroic, which means for this special case that if the cup is held perpendicular to direct light it resembles a jade colour but when light shines through the glass, the transmitted light turns ruby. They achieved this unique effect by incorporating gold particles into the material. New findings show that these were particles with a diameter of 50-100 nm.[13] The gold nanoparticles have a lower energy of plasmon resonances compared to the bulk gold of the cup which induces this colour change. The artisans weren't aware during the production that they were using gold nanoparticles, but with these gold colloids, they built the basis for gold nanoparticles being used as visible/near infrared diagnostics in the field of na-

nomedicine more than 1500 years later.[14] In the 9th century AD, Mesopotamians introduced silver and copper glazed ceramics which also obtained colloids of nanometre size.[15] Their colloidal texture of copper and silver plays a crucial role in the diffuse colouration.[16] This Mesopotamia lusterware can nowadays be considered as an historical example of controlled nanotechnology – back in the ninth century.[17]

Another large leap of time (1000 years) later, in 1959, Richard Feynman made his famous statement in his eponymous talk "there is a plenty of room at the bottom".[18] In this speech, he presented the concept of how to write all the information of all the books in the world in a cube of material with 1/200 of an inch wide, which would be the smallest piece of dust that a human eye can see. This statement brought nanotechnology back on stage in the scientific world. 15 years later, the word "nanotechnology" was used for the first time in literature.[19] In the late 1960s, Peter Speiser pioneered miniaturised drug delivery by developing first nano-particles for this purpose, as well as for vaccines, and built the concept for polymeric nano-particles.[20] Around one decade later, there were great advances in rapidly biodegradable drug loaded polymeric nanoparticles due to high efforts by Robert Langer.[21] In 1985, Donald A. Tomalia introduced poly(amidoamine) dendrimers as a new class of polymers named "starburst polymers".[22] Their use improves many relevant biological properties such as bioa-vailability, solubility, and selectivity, of which the latter is one of the main advances by poly(amidoamine) and enables diverse applications, i.e. in biomedicine.[23]

In the same year, Robert F. Curl and Harold W. Kroto published the first C_{60} buckminsterfull-erene,[24] for which they received the Nobel Prize eleven years later. C_{60} plays an interesting role for drug delivery, since it can be multifunctionalized, forms nanoparticles and acts as a drug absorbent. To overcome its initial insolubility in water, partial masking of the apolar full-erene surface or covalent modifications of the aromatic structure were used.[25] Five years after the first publication on these fullerenes, in 1990, Wolfgang Krätschmer concentrated them in a new solid form,[26] which was experimentally proven one year later by Sumio Iijima as a new material called carbon nanotubes.[27] They can be functionalised with bioactive pep-tides, proteins, nucleic acids and drugs, show low toxicity as functionalised excipients and are not immunogenic while delivering their loading to cells and organs.[28] In addition to the better solubility of functionalized carbon nanotubes, they also show a high propensity to cross cell membranes, can be charged with biologically active moieties and offer the possibil-ity to get more than one function introduced on the same tube. Thus, among others, drugs, targeting molecules and contrast agents can be transported at the concurrently.[28]

At the same time, in the early 1990s, the interest in shape-controlled nanoparticles became very high, starting with the publication of Hideki Masuda about a preparation techniques of

gold nanorods, where a microporous structure of anodic alumina film is replaced by metal.[29] Since then, gold nanoparticles are used in a variety of research fields, among others in techniques for treating cancer (photodynamic therapy),[30] as vesicle drug delivery carrier,[31] or, as recently published, to enhance the therapeutic efficacy of small interfering RNA drugs.[32] This last publication deals with the doping of conventional small-interfering RNA-liposomal formulations with gold nanoparticles to enhance gene silencing. They showed that a gold nanoparticle size of 20 nm leads to excellent biostability, less lysosomal degradation, superior gene silencing, and reduction of toxicity as well as inhibition of tumour growth in human xenograft. Although one liposomal small interfering RNA drug is FDA-approved, there is no therapeutic intervention for ovarian cancer with such kind of RNA yet. Continuing in the year 1995, liposomal doxorubicin (Doxil®) was approved as the first nano-drug by the FDA. It is based, among others, on the use of PEGylated nano-liposomes.[33] The first liposomes were already described 30 years earlier and soon proposed as drug delivery systems.[34] Liposomal drugs are known for their ability to reduce the side effects of the encapsulated drugs relative to free drugs. This ability increases the therapeutic index of the drugs weighing the efficacy against toxicity.

From the early 2000s, many research groups tried to functionalize mesoporous silica nanoparticles with biological components such es antibodies, nucleic acids, and cell membranes for a better and controlled biodistribution and a reduced toxicity. In 2012, Alessandro Parodi prepared nanoporous silicon particles, which evade the immune system, cross the biological barriers of the body as well as being localized at target tissues, when they are coated with cellular membranes.[35] One main idea and aim of this concept was to avoid being cleared by the immune system as it reduces the possibility to be detected as foreign matter. The use of poly(ethylene glycol) (PEG) attached to various different proteins has long been used to reduce the immunogenicity and thus to protect proteins from the host's immune system. However, in the meantime, anti-PEG antibody formation after a therapy with PEGylated proteins was documented.[36] A recent publication lists various types of cell membrane-cloaked nanoparticles for biomedical applications, but also points out the currently existing limitations of these systems such as complex preparation methods, low yields, low synthesis scales, and difficult preservation.[37]
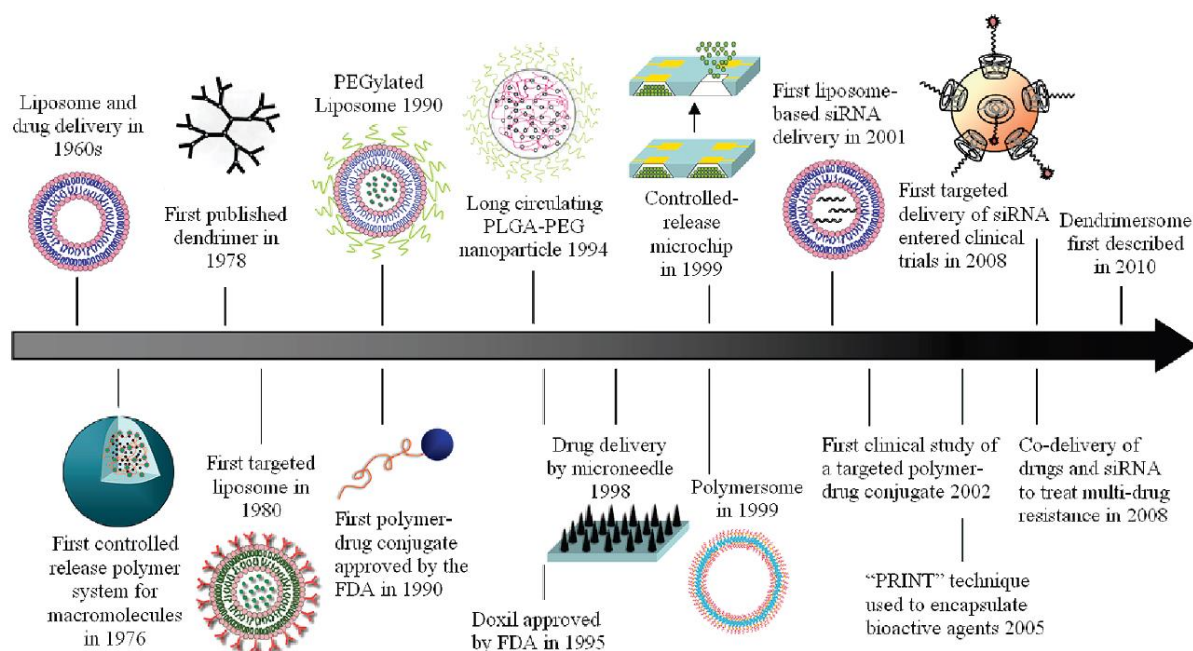
Figure 3: Historical timeline of nanotechnology-based drug delivery systems that serve as important milestones throughout the history of drug delivery, until the year 2010. Permission of ref [38]. Copyright 2010 American Chemical Society.

The timeline in **Figure 2** shows milestones of the developments in nanomedicine over a very long time period. **Figure 3** highlights another timeline that deals with important developments of nanotechnology-based drug delivery systems from 1960-2010.[38] This timeline, published by the group of Robert Langer, focusses on more specific drug delivery systems and their substantial improvement during this period.

Polymeric micelles as drug delivery systems

Since the NMR spectroscopic investigation of polymeric micelles as drug delivery systems (DDS) represent one main topic of this dissertation, this type of DDS will be discussed in more detail. As mentioned earlier, at the end of the 1970s, the research group around Robert Langer attracted a lot of attention for their effort and advances in rapidly biodegradable drug loaded polymeric nanoparticles. In the early 1980s, the first use of polymeric micelles for cancer treatment was reported.[39] They are supramolecular, nanoscaled core-shell structures formed by amphiphilic block copolymers (an exemplary scheme of the two investigated components of this work is shown in **Scheme 2**). In water, the hydrophobic part of the copolymers self-associates into a semi-solid core whereas at the same time a coronal layer is formed by the hydrophilic regions.[40] Micellization is mainly entropy-driven.[41] Water molecules close to the hydrophobic blocks of the non-aggregated polymer lead to reduced allowed mutual orientations resulting in a decrease of entropy. If the loss of entropy for this process is larger than for self-assembly, micellization takes place. For a more detailed de-

scription of the physical background, the reader is referred to ref [41] and ref [42]. Above the critical micelle concentration (CMC), additionally dissolved polymers directly form micelles. An accompanying aspect is the constant surface tension of the micelle. While for some research areas the CMC is an unwanted limit, in the case of DDS it is preferable to overcome this threshold. A further important parameter is the loading capacity (LC) of the polymeric micelles, which is defined as the total mass m_{Drug} of entrapped drug divided by the total mass of the resulting micelle:

$$LC = \frac{m_{Drug}}{m_{Drug} + m_{Polymer}}$$

The importance of a high possible LC value is illustrated by the nonionic surfactant Cremophor EL (CrEL), which is a formulation vehicle for PTX and thus of particular interest for this thesis. The best-known biological side-effects of these formulations are acute hypersensitivity, dyspnoea, flushing, rash chest pain, tachycardia, hypotension, angio-oedema, and generalised urticaria.[43] Minor side-effects on the patients occur in around 40% of the cases while strong and potentially life-threatening reactions still are observed for 1.5-3% of the patients. These values refer to a formulation of 30 mg PTX dissolved in 5 ml of a 1:1 mixture of 50% CrEL and 50% dehydrated ethanol. Several investigations of this specific formulation point out that all side-effects are caused by CrEL.[43] These findings were already published in 2001. Since then, several different ways were investigated to replace Cremophor EL whereas a further focus laid on a high LC which consequently leads to less excipient caused side-effects.

Therefore, a variety of different formulations for PTX was developed.[44] This includes the protein-based nanoparticle Abraxane®, the polymer-conjugate Opaxio™ as well as Genexol-PM® and NK105.[45] The latter two contain PTX in polymer micelles formed by polyethylene glycol–polylactic acid (Genexol-PM®) and polyethylene glycol-poly(amino acid) (NK105) copolymers. In general, the development of formulations and their clinical trials require very long times with highly uncertain outcomes. The above-mentioned formulations have undergone multiple phase II/III clinical trials over the past decades, e.g. a recently published phase III clinical trial of NK105,[46] but only Abraxane® is successfully marketed with FDA approval since 2007. Furthermore, they are all characterized by a relatively low PTX loading not exceeding 25 wt.%. In this context, Luxenhofer *et al.*[47] reported promising preclinical data for polymer micelles comprising poly(2-oxazoline) (POx) based triblock copolymers loaded with up to 50 wt.% of PTX. Compared to the clinically approved PTX formulations, their formulations show higher maximum tolerated doses, elevated drug exposure to tumour tissue, and prolonged survival for mice bearing A2780 human ovarian tumours. Schulz *et al.*[48], Jaksch

et al.[49], and Sochor *et al.*[50] studied their micellar morphology for different drug loadings (PTX and curcumin) using dynamic light scattering, atomic force microscopy, (cryogenic) transmission electron microscopy, and small-angle neutron scattering (SANS). They found that the pure polymer self-assembles into wormlike and spherical micelles in aqueous solution, while incorporation of PTX led to the exclusive formation of spherical micelles. Interestingly, SANS data revealed small, PTX rich domains partly submerged within the micellar core. Apart from such morphological aspects and to be able to design improved drug delivery systems, it is very important to also understand the complex structural arrangements and interactions in such amorphous drug-polymer formulations on a molecular level.

Continuing on the results described above, Lübtow *et al.*[51] found that even a small change in the polymer structure, namely a migration of a methylene group from the polymer side chain to the polymer main chain, led to a strongly altered specific drug load of PTX and the natural product curcumin. All the publications based on these systems have in common that they do not provide insights of the interaction between the polymer POL and the drug PTX on an atomic level. This knowledge about the interactions can give explanations about the structural composition and its underlying mechanism of these systems such as the coupling of POL and PTX via dipolar interaction in spatial proximity of certain molecular groups. One possible experimental method to enable those insights is NMR.

NMR probes the local environment of atoms and molecules and is thus an excellent tool to report on various possible interactions. The sometimes strongly reduced mobility of encapsulated drugs within drug formulations can hinder the characterization by NMR in solution due to strong broadening of the signals, which makes solid-state NMR the method of choice.[52] Crystalline or well-ordered structures are not required and the experiments also gives valuable results for disordered as well as amorphous samples. Solid-state NMR has been established as a powerful tool for structure elucidation in pharmaceutical contexts such as identification of polymorphs or investigation of amorphous solid dispersions.[53] The enormous progress made with respect to hardware development, e.g. MAS frequencies of up to 130 kHz being available now,[54] also enables high-resolution detection of protons in the solid state and longer coherence lifetimes.[55] Callari *et al.*[56] as well as Pöppler *et al.*[57] recently showcased how solid-state NMR at moderate to fast Magic Angle Spinning (MAS) helps to obtain loading dependent structural insights into micellar formulations with an assumed core-shell structure. Both groups found that increasing the loading of two different types of polymeric micelles did not just affect the micellar core but interestingly also the surrounding shell, which served as a basis to explain their physicochemical and biological properties such as reduced cellular uptake and inferior dissolution rates. For the mentioned studies, micelles are investigated in their solid state. In general, micelles are only proven to exist in a selective solvent.

However, there are several strong indications for micelles to exist in their solid-state form as well, including a similar system to the one investigated in this work which also contains PTX as drug: Luxenhofer *et al.*[58] showed that the micelles can be lyophilized and subsequently redispersed in water without a change in drug loading, particle size or *in vitro* drug activity.

This should bring us back to the initial question: "Is the field of drug delivery no longer of interest for research due to the downward trend of absolute number of publications containing the term "drug delivery"?" Again, reference should be made to the publications of Leroux *et al.*[59] as well as Mitragotri *et al.*[60] mentioned in this context. On the one hand, it is emphasized that new ways must be found to better explore the unique characteristics of nanotechnology and more development of transport technologies is needed for clinical application.[59] Furthermore, they addressed the reader with the direct question: *"What aspects of nanotechnology are key to future drug delivery systems, what are the key hurdles in the field, and how do we address them to fulfill its true potential?"*[60] This is intended to call and encourage greater focus on research on fundamental mechanisms and contributions, including the characterization of nanoparticles.[60] A multifaceted and multidisciplinary approach is needed for future drug delivery systems to fulfil their true potential. Only one publication or manuscript of the current doctoral study contains the term "drug delivery", as they focus on the system itself for deeper understanding of the interaction and the structure. This can be one puzzle piece towards future nanotechnological advances.

To answer the initial question: The research in the field of drug delivery itself isn't on a downward trend. This field deals with such a huge number of formulations for various diseases and is so large that research often can only focus on one aspect.[60] Therefore, very much remains to explore and understand. This further research will often go beyond the development of new DDS. Thus, this dissertation will focus on fundamental research, but the outcome won't be less valuable or of less urgent scientific need for our common goal: the fight against diseases.

The first part addresses the detailed characterization of the crystalline drug PTX, which due to its size and complexity has only been partially characterized by solid-state NMR. As the number of resonances in the solid-state NMR spectrum directly correlates with crystallographic symmetry, such an analysis is particularly attractive in the field of pharmaceutical solids and their polymorphs.[61] This study includes ^{13}C NMR investigations, ^{1}H MAS data up to 100 kHz and supporting geometric calculations of published crystal structures. Complementary PXRD techniques are also used with the aim to obtain a new crystal structure.

The second part of this dissertation deals with the detailed investigation of nitrogen-hydrogen proximities of the DDS consisting of POL-PTX formulations. The frequent involvement of nitrogen atoms in hydrogen bonding in pharmaceuticals makes this nucleus a promising starting point for a detailed investigation of PTX containing formulations (**Scheme 2**) through 2D nitrogen-proton correlation NMR experiments in the solid state. Therefore, ^{14}N-^{1}H HMQC MAS NMR experiments[62] will be investigated as a valuable tool to disperse overlapping ^{15}N signals by observing ^{14}N nuclei, which contain additional quadrupolar shifts. The aim is to test the applicability of this promising NMR method to the POL-PTX system with a complexity to which it has not yet been applied.
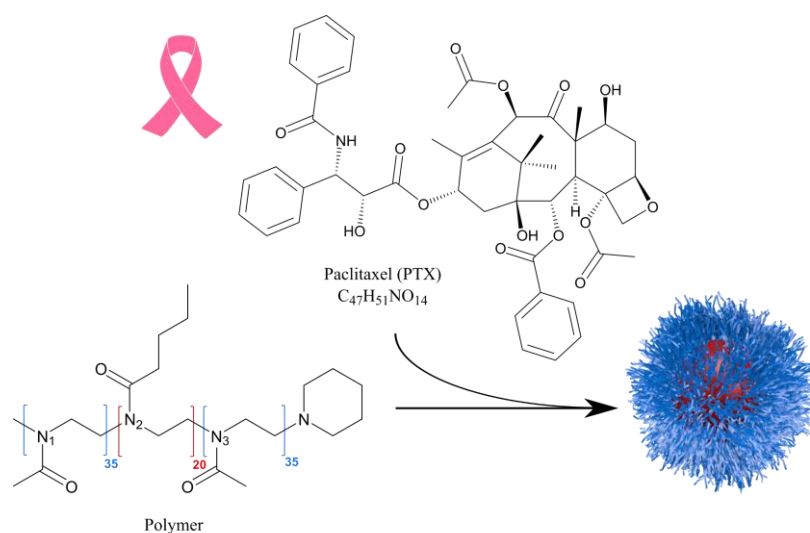
Scheme 2: Structural formulas of the components used in this study and schematic drawing of a micelle: The amphiphilic block copolymer poly(2-methyl-2-oxazoline)-block-poly(2-n-butyl-2-oxazoline)-block-poly(2-methyl-2-oxazoline) (POL) encapsulates paclitaxel (PTX) by self-assembly into polymeric micelles. Reprinted with the permission from ref.[63] Copyright 2020 Royal Society of Chemistry.

In the third part, the PTX loaded polymeric micelles (**Scheme 2**) are characterized by solid-state NMR to get insights and learn more about the structural details for a stepwise drug loading, aiming for a structural model of this process. This part investigates differently loaded formulations with various solid-state NMR experiments with the focus of the analysis regarding the interaction of PTX and POL. In addition, the possibilities and limits of solid-state NMR studies of such very complex drug polymer systems are intended to be specified.

References

[1] M. E. Wall, M. C. Wani, *153rd National Meeting, American Chemical Society* **1967**.

[2] Harshita, M. A. Barkat, SarwarBeg, F. H. Pottoo, F. J. Ahmad, *Nanomedicine* **2019**, *14*, 1323-1341.

[3] a) S. B. Horwitz, D. Cohen, S. Rao, I. Ringel, H. J. Shen, C. P. Yang, *J. Natl. Cancer Inst. Monogr.* **1993**, 55-61; b) D. M. Bollag, P. A. McQueney, J. Zhu, O. Hensens, L. Koupal, J. Liesch, M. Goetz, E. Lazarides, C. M. Woods, *Cancer Res.* **1995**, *55*, 2325-2333.

[4] R. T. Liggins, W. Hunter, H. M. Burt, *J. Pharm. Sci.* **1997**, *86*, 1458-1463.

[5] a) H. Dowden, J. Munro, *Nat. Rev. Drug Discovery* **2019**, *18*, 495-496; b) U. S. Food and Drug Administration (FDA). Novel drug approvals for 2018. Available at: https://www.fda.gov/drugs/new-drugs-fda-cders-new-molecular-entities-and-new-therapeutic-biological-products/novel-drug-approvals-2018. Accessed December 16, 2020.

[6] S. Hassan, G. Prakash, A. Bal Ozturk, S. Saghazadeh, M. F. Sohail, J. Seo, M. R. Dokmeci, Y. S. Zhang, A. Khademhosseini, *Nano Today* **2017**, *15*, 91-106.

[7] S. Kalepu, V. Nekkanti, *Acta Pharm. Sin. B* **2015**, *5*, 442-453.

[8] M. Rodriguez-Aller, D. Guillarme, J.-L. Veuthey, R. Gurny, *J. Drug Delivery Sci. Technol.* **2015**, *30*, 342-351.

[9] a) L. Di, E. H. Kerns, G. T. Carter, *Curr. Pharm. Des.* **2009**, *15*, 2184-2194; b) L. Di, P. V. Fish, T. Mano, *Drug discovery today* **2012**, *17*, 486-495.

[10] H. D. Williams, N. L. Trevaskis, S. A. Charman, R. M. Shanker, W. N. Charman, C. W. Pouton, C. J. Porter, *Pharmacol. Rev.* **2013**, *65*, 315-499.

[11] V. Wagner, A. Dullaart, A.-K. Bock, A. Zweck, *Nat. Biotechnol.* **2006**, *24*, 1211-1217.

[12] R. A. Freitas, *Nanomedicine, volume I: basic capabilities, Vol. 1*, Landes Bioscience Georgetown, TX, **1999**.

[13] I. Freestone, N. Meeks, M. Sax, C. Higgitt, *Gold Bull* **2007**, *40*, 270-277.

[14] S. McMahon, F. Currell, in *Front. Nanosci., Vol. 5*, Elsevier, **2013**, pp. 65-93.

[15] a) D. V. Hill, R. J. Speakman, M. D. Glascock, H. Neff, *Vol. 968*, ACS Symposium Series, **2007**, pp. 422-446; b) P. Sciau, *Nanoparticles in ancient materials: the metallic lustre decorations of medieval ceramics, Vol. 115*, INTECH Open Access Publisher, **2012**.

[16] O. Bobin, M. Schvoerer, C. Ney, M. Rammah, B. Pannequin, E. C. Platamone, A. Daoulatli, R. Gayraud, *Archaeometry* **2003**, *28*, 352-359.

[17] P. Sciau, C. Mirguet, C. Roucau, D. Chabanne, M. Schvoerer, *J. Nano Res.* **2009**, *8*, 133-139.

[18] R. P. Feynman, in *Engineering and science, Vol. 23*, **1959**.

[19] N. Taniguchi, in *Proceeding of the ICPE*, **1974**.

[20] J. Kreuter, *Int. J. Pharm.* **2007**, *331*, 1-10.

[21] a) Y. Cao, R. Langer, in *Proceedings of the National Academy of Sciences, Vol. 105*, **2008**, pp. 13203-13205; b) R. Langer, J. Folkman, *Nature* **1976**, *263*, 797-800.

[22] D. A. Tomalia, H. Baker, J. Dewald, M. Hall, G. Kallos, S. Martin, J. Roeck, J. Ryder, P. Smith, *Polymer J.* **1985**, *17*, 117-132.

[23] R. V. d. Araújo, S. d. S. Santos, E. Igne Ferreira, J. Giarolla, *Molecules* **2018**, *23*, 2849.

[24] H. W. Kroto, J. R. Heath, S. C. O'Brien, R. F. Curl, R. E. Smalley, *Nature* **1985**, *318*, 162-163.

[25]   A. Montellano, T. Da Ros, A. Bianco, M. Prato, *Nanoscale* **2011**, *3*, 4035-4041.

[26]   W. Krätschmer, L. D. Lamb, K. Fostiropoulos, D. R. Huffman, *Nature* **1990**, *347*, 354-358.

[27]   S. Iijima, *Nature* **1991**, *354*, 56-58.

[28]   A. Bianco, K. Kostarelos, M. Prato, *Curr. Opin. Chem. Biol.* **2005**, *9*, 674-679.

[29]   H. Masuda, H. Tanaka, N. Baba, *Chem. Lett.* **1990**, *19*, 621-622.

[30]   Y. Cheng, A. C. Samia, J. D. Meyers, I. Panagopoulos, B. Fei, C. Burda, *J. Am. Chem. Soc.* **2008**, *130*, 10643-10647.

[31]   K. Niikura, N. Iyo, Y. Matsuo, H. Mitomo, K. Ijiro, *ACS Appl. Mater. Interfaces* **2013**, *5*, 3900-3907.

[32]   M. N. Hossen, L. Wang, H. R. Chinthalapally, J. D. Robertson, K.-M. Fung, S. Wilhelm, M. Bieniasz, R. Bhattacharya, P. Mukherjee, *Sci. Adv.* **2020**, *6*, eaba5379.

[33]   Y. C. Barenholz, *J. Controlled Release* **2012**, *160*, 117-134.

[34]   T. M. Allen, P. R. Cullis, *Adv. Drug Delivery Rev.* **2013**, *65*, 36-48.

[35]   A. Parodi, N. Quattrocchi, A. L. Van De Ven, C. Chiappini, M. Evangelopoulos, J. O. Martinez, B. S. Brown, S. Z. Khaled, I. K. Yazdi, M. V. Enzo, *Nat. Nanotechnol.* **2013**, *8*, 61-68.

[36]   a) A. P. Chapman, *Adv. Drug Delivery Rev.* **2002**, *54*, 531-545; b) C. Lubich, P. Allacher, M. de la Rosa, A. Bauer, T. Prenninger, F. M. Horling, J. Siekmann, J. Oldenburg, F. Scheiflinger, B. M. Reipert, *Pharm. Res.* **2016**, *33*, 2239-2249.

[37]   B. Choi, W. Park, S.-B. Park, W.-K. Rhim, D. K. Han, *Methods* **2020**, *177*, 2-14.

[38]   J. Shi, A. R. Votruba, O. C. Farokhzad, R. Langer, *Nano Lett.* **2010**, *10*, 3223-3230.

[39]   L. Gros, H. Ringsdorf, H. Schupp, *Angew. Chem. Int. Ed.* **1981**, *20*, 305-325.

[40]   E. Blanco, C. W. Kessinger, B. D. Sumer, J. Gao, *Exp. Biol. Med.* **2009**, *234*, 123-131.

[41]   P. Shi, H. Zhang, L. Lin, C. Song, Q. Chen, Z. Li, *RSC Adv.* **2019**, *9*, 3224-3231.

[42]   T. Lodge, M. Muthukumar, *J. Phys. Chem.* **1996**, *100*, 13275-13292.

[43]   H. Gelderblom, J. Verweij, K. Nooter, A. Sparreboom, *Eur. J. Cancer* **2001**, *37*, 1590-1598.

[44]   A. M. Sofias, M. Dunne, G. Storm, C. Allen, *Adv. Drug Delivery Rev.* **2017**, *122*, 20-30.

[45]   a) Y. S. Youn, Y. H. Bae, *Adv. Drug Deliv Rev.* **2018**, *130*, 3-11; b) Z. He, A. Schulz, X. Wan, J. Seitz, H. Bludau, D. Y. Alakhova, D. B. Darr, C. M. Perou, R. Jordan, I. Ojima, *J. Controlled Release* **2015**, *208*, 67-75.

[46]   Y. Fujiwara, H. Mukai, T. Saeki, J. Ro, Y.-C. Lin, S. E. Nagai, K. S. Lee, J. Watanabe, S. Ohtani, S. B. Kim, *Br. J. Cancer* **2019**, *120*, 475.

[47]   a) Z. He, X. Wan, A. Schulz, H. Bludau, M. A. Dobrovolskaia, S. T. Stern, S. A. Montgomery, H. Yuan, Z. Li, D. Alakhova, M. Sokolsky, D. B. Darr, C. M. Perou, R. Jordan, R. Luxenhofer, A. V. Kabanov, *Biomaterials* **2016**, *101*, 296-309; b) R. Luxenhofer, A. Schulz, C. Roques, S. Li, T. K. Bronich, E. V. Batrakova, R. Jordan, A. V. Kabanov, *Biomaterials* **2010**, *31*, 4972-4979.

[48]   A. Schulz, S. Jaksch, R. Schubel, E. Wegener, Z. Di, Y. Han, A. Meister, J. Kressler, A. V. Kabanov, R. Luxenhofer, C. M. Papadakis, R. Jordan, *ACS Nano* **2014**, *8*, 2686-2696.

[49]   S. Jaksch, A. Schulz, Z. Di, R. Luxenhofer, R. Jordan, C. M. Papadakis, *Macromol. Chem. Phys.* **2016**, *217*, 1448-1456.

[50]   B. Sochor, Ö. Düdükcü, M. M. Lübtow, B. Schummer, S. Jaksch, R. Luxenhofer, *Langmuir* **2020**, *36*, 3494-3503.

[51]   M. M. Lübtow, L. Hahn, M. S. Haider, R. Luxenhofer, *J. Am. Chem. Soc.* **2017**, *139*, 10980-10983.

[52]   a) R. F. Moran, D. M. Dawson, S. E. Ashbrook, *Int. Rev. Phys. Chem.* **2017**, *36*, 39-115; b) S. E. Ashbrook, P. Hodgkinson, *J. Chem. Phys.* **2018**, *149*, 040901; c) P. Florian, F. Fayon, in *Modern Methods in Solid-state NMR: A Practitioner's Guide*, The Royal Society of Chemistry, **2018**, pp. 356-390.

[53]   a) R. K. Harris, *J. Pharm. Pharmacol.* **2007**, *59*, 225-239; b) H. G. Brittain, *Polymorphism in Pharmaceutical Solids, Second Edition*, CRC Press, **2009**; c) S. Baghel, H. Cathcart, N. J. O'Reilly, *J. Pharm. Sci.* **2016**, *105*, 2527-2544.

[54]   S. K. Vasa, P. Rovó, R. Linser, *Acc. Chem. Res.* **2018**, *51*, 1386-1395.

[55]   a) S. P. Brown, *Solid State Nucl. Magn. Reson.* **2012**, *41*, 1-27; b) R. Zhang, K. H. Mroue, A. Ramamoorthy, *Acc. Chem. Res.* **2017**, *50*, 1105-1113; c) Y. Nishiyama, *Solid State Nucl. Magn. Reson.* **2016**, *78*, 24-36.

[56]   M. Callari, P. L. De Souza, A. Rawal, M. H. Stenzel, *Angew. Chem. Int. Ed.* **2017**, *56*, 8441-8445.

[57]   A. C. Pöppler, M. M. Lübtow, J. Schlauersbach, J. Wiest, L. Meinel, R. Luxenhofer, *Angew. Chem. Int. Ed.* **2019**, *58*, 18540-18546.

[58]   R. Luxenhofer, A. Schulz, C. Roques, S. Li, T. K. Bronich, E. V. Batrakova, R. Jordan, A. V. Kabanov, *Biomaterials* **2010**, *31*, 4972-4979.

[59]   J. C. Leroux, *Angew. Chem. Int. Ed.* **2017**, 56, 2-4.

[60]   S. Mitragotri, T. Lammers, Y. H. Bae, S. Schwendeman, S. C. De Smedt, J. C. Leroux, D. Peer, I. C. Kwon, H. Harashima, A. Kikuchi, *J. Controlled Release* **2017**, *246*, 183-184.

[61]   a) D. Singh, P. V. Marshall, L. Shields, P. York, *J. Pharm. Sci.* **1998**, *87*, 655-662; b) J. C. Burley, M. J. Duer, R. S. Stein, R. M. Vrcelj, *Eur. J. Pharm. Sci.* **2007**, *31*, 271-276; c) F. G. Vogt, G. R. Williams, M. N. Johnson, R. C. Copley, *Cryst. Growth Des.* **2013**, *13*, 5353-5367; d) N. Zencirci, U. J. Griesser, T. Gelbrich, D. C. Apperley, R. K. Harris, *Mol. Pharmaceutics* **2014**, *11*, 338-350; e) C. M. Widdifield, S. O. N. Lill, A. Broo, M. Lindkvist, A. Pettersen, A. S. Ankarberg, P. Aldred, S. Schantz, L. Emsley, *Phys. Chem. Chem. Phys.* **2017**, *19*, 16650-16661.

[62]   A. S. Tatton, J. P. Bradley, D. Iuga, S. P. Brown, *Z. Phys. Chem.* **2012**, *226*, 1187-1204.

[63]   M. Grüne, R. Luxenhofer, D. Iuga, S. P. Brown, A.-C. Pöppler, *J. Mater. Chem. B* **2020**, *8*, 6827-6836.

Manuscript 1:

New anhydrous crystalline phase of paclitaxel revealed by solid-state NMR spectroscopy, powder X-ray diffraction and complementary quantum chemical calculations

Marvin Grüne[a], Dominik Heuler[b], Klaus Müller-Buschbaum[b] and Ann-Christin Pöppler[a]*

[a] *Institute of Organic Chemistry, University of Würzburg, Am Hubland, 97074 Würzburg, Germany*
[b] *Institute of Inorganic and Analytical Chemistry, University of Gießen, 35392 Gießen, Germany*

Introduction

Currently, one of the most important and relevant drugs to combat breast and ovarian cancers is paclitaxel (PTX, $C_{47}H_{51}NO_{14}$), which is known since the 1960s.[1] A detailed overview from the discovery until the first total synthesis in 1994 is given by Wall and Wani, the scientists responsible for the initial discovery.[2] While its efficiency to combat breast and ovarian cancers is already established, it is currently also undergoing clinical trials for use against other types of cancer.[3] The mechanism of action of PTX includes blocking of
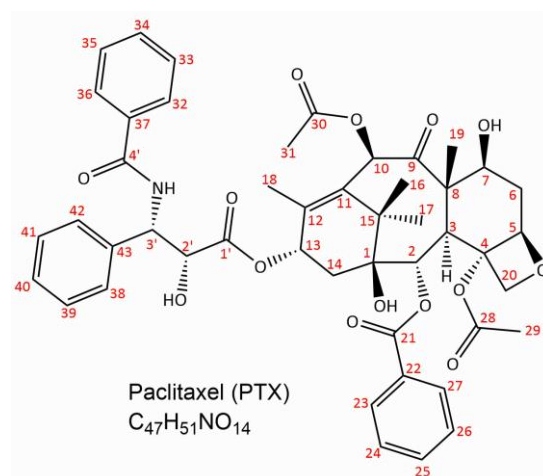
Scheme 1: Structural formula of paclitaxel (PTX).

the attacked cell in the mitotic phase in the cell cycle by stabilizing the microtubule cytoskeleton.[4] PTX has a variety of solid-state forms, differing in their physical and chemical properties. However, obtaining a crystal structure of paclitaxel or a closely related derivative turned out to be very difficult for more than two decades after the determination of the molecular structure was completed in 1971.[5] In 1995/1996, two scientists independently published different crystal structure of paclitaxel and its derivatives. Mastropaolo *et al.* grew dioxane solvent hydrate paclitaxel crystals and analyzed them by X-ray diffraction, although they suffered from decomposition due to solvent loss and X-ray damage.[6] Analogously, Gao and coworkers investigated three different chemically modified derivatives of paclitaxel.[7] In 2005, there was still no crystal structure available for pure PTX. Therefore, Harper *et al.* used solid-state NMR to investigate a stable polymorph of paclitaxel with only a low water content, identifying two molecules per asymmetric unit.[8] Apart from their second publication in 2007,[9] in which a large number of carbon resonances could be assigned with the help of complementary calculations, no further findings using solid-state NMR to elucidate the structure of paclitaxel were published. It was not until 2013 that Vella-Zarb *et al.* published the first solvent-free crystal structure of PTX

alongside two hydrous forms, a hemihydrate- and a dihydrate (**Table 1**).[10] The water mole-cules of the hydrated form are loosely bound and lost upon moderate heating. The dihydrate structure was solved based on single-crystal synchrotron diffraction data, while the other two structures were obtained by X-ray powder diffraction (PXRD) at elevated temperatures. All three structures contain two molecules in the asymmetric unit and eight molecules in the unit cell (at least 904 atoms) in an arrangement corresponding to the space group $P2_12_12_1$.

Table 1: Crystallographic data of the three forms of paclitaxel as published by Vella-Zarb *et al.*[10]

Structure	Dihydrate	Hemihydrate	Anhydrate
# Water Molecules (AU)	6	1	0
CCDC Number	912149	912148	912147
a [Å]	9.512	9.68905	9.653
b [Å]	28.064	28.0760	28.120
c [Å]	33.08	33.6166	33.538
α/β/γ [°]	90/90/90	90/90/90	90/90/90
Temperature [K]	120.15	293	313
Experiment Type	Single Crystal (Syn-chrotron)	Powder	Powder
Comments	2 H missing (H_2O)	used as published	3 H missing

Like many anti-cancer drugs, the overall activity of PTX is hampered by its poor aqueous sol-ubility.[11] Therefore, a variety of different pharmaceutical formulations was and still are devel-oped.[3, 12] To value the large body of work, which has gone into the development of these formulations and to improve their performance in the future, it is important to understand the miscibility of PTX and the excipient, underlying structural arrangements and key intermolecular interactions between PTX and the excipients. From such data, structure-property relations and ultimately formulations with targeted modifications and new properties can arise. Recent work has shown that solid-state NMR is a promising tool and can form the basis for the desired improvements.[13] However, an essential requirement for this approach is the detailed knowledge of the drug molecule itself and most importantly a complete assignment of all ^{1}H, ^{13}C, and ^{15}N resonances. Due to the complexity of the drug molecule itself and the fact that there are two individual molecules in the asymmetric unit (giving rise to two sets of very similar yet not identical chemical shifts), a complete assignment is challenging. Recent improvements in the hardware for solid-state NMR, in particular the availability of high magnetic fields and fast magic angle spinning (MAS) above 100 kHz,[14] combined with reliable tools for the calcu-lation of solid-state NMR parameters and the crystal structures published by Vella-Zarb *et al.*[10] hold the promise for improving the existing partial assignment of the heteronuclei and attempt-ing the assignment of ^{1}H NMR data by thoroughly investigating this important yet complex molecule.

Due to NMR spectroscopy being very sensitive to subtle changes in the local environment of the respective nuclei, it is a particularly powerful technique to analyze ordered materials with more than one individual molecule in the asymmetric crystallographic unit. As the number of

resonances in the ^{13}C solid-state NMR spectrum directly correlates with crystallographic symmetry, such an analysis is particularly attractive in the field of pharmaceutical solids and their polymorphs, which is documented by a variety of published reports.[15] This is of course not a phenomenon limited to pharmaceutical compounds, but concerns a subset of about 9% of crystal structures and the advancements in the detailed analysis of such structures are also of interest for a broad range of scientific communities.[16] The combination of solid-state NMR with periodic structure calculations for general signal assignment is well established and has been summarized in several reviews.[17] Especially for structures with Z' > 1, this combination of complementary insights is at its most impressive. The sensitivity of NMR spectroscopy to the local environment is impressively demonstrated by the work of Brown *et al.*, who reported NMR spectroscopic data in the solid state in combination with GIPAW[18] (gauge-including projector augmented wave) / CASTEP calculations of campho[2,3-*c*]pyrazole, which contains a remarkable number of six individual molecules in the asymmetric unit (Z' = 6).[19] Due to the identical chemical entities but individual environments, a series of similar yet not identical chemical shifts is obtained in the ^{13}C CP MAS NMR spectrum. Due to the strong signal overlap and small differences in chemical shifts, the assignment of such spectra is far from being trivial. However, through the combination with complementary GIPAW (CASTEP) calculation, Brown *et al.* succeeded in providing a complete assignment of all molecules and chemical sites in this system. A similar demonstration of the suitability of this set of analytical tools for the complete assignment of materials with Z' > 1 by the same group concerns guanosine derivatives, which are in the focus due to their rich supramolecular chemistry.[20]

The above-mentioned advancements and findings show that a thorough solid-state NMR investigation of PTX including assignment of ^{1}H NMR data should be feasible despite the complexity of the molecule. This structural understanding can serve as important puzzle piece in the future investigation of various PTX formulation types. Based on the recent report of the first ^{1}H solid-state NMR data for PTX,[21] we present a detailed structural investigation of crystalline PTX using 1D and 2D solid-state NMR complemented by X-ray powder diffraction (PXRD), extensive GIPAW (CASTEP) calculations and differential scanning calorimetry (DSC). This investigation led to the identification of a new, anhydrous phase of PTX. Based on our experiments, we propose this new form to be a structurally relaxed version of the anhydrous phase initially obtained in-situ by Vella-Zarb *et al.*[10]

Experimental section

Material

Both batches of paclitaxel (PTX) in its crystalline form were purchased from *LC Laboratories* (Woburn, MA, USA) and used without further purification. *PTX Dry* was prepared by drying

material from *PTX Batch 2* for three days at 70°C and subsequently seven days at room temperature. Heating at lower temperature or for a reduced time resulted in an amorphous phase. Lyophilization was used to prepare fully amorphous PTX. More details on the experimental procedures and analytical data of the different batches and phases can be found in the SI.

NMR

All ^{13}C NMR data, except the data for *PTX Batch 2*, were obtained with a Bruker Avance III HD 600 MHz (14.1 T) spectrometer and a 3.2 mm double-channel MAS probe. The ^{13}C CP MAS data of *PTX Batch 2* were acquired using a Bruker Avance Neo 400 MHz (9.4 T) spectrometer and a 4 mm double-channel MAS probe. ^{1}H NMR data at 60 and 65 kHz were measured on a Bruker Avance III HD 600 MHz spectrometer with a Bruker 1.3 mm double-channel MAS probe. The [1]H(DQ)-[1]H(SQ) BABA spectrum at 100 kHz MAS was recorded with a Bruker Avance NEO 700 MHz (16.4 T) spectrometer and a 0.7 mm double-channel MAS probe.

The duration of the ^{1}H pulses was 2.50 µs in the ^{13}C CP MAS with ramped cross-polarization conditions optimized with α-glycine using a ramp from 90 to 100 with 100 increments and a contact time of 2.5 ms. SPINAL-64[22] heteronuclear decoupling was applied during an acquisition period of 23 ms at a [1]H *rf* nutation frequency of 100 kHz, with an optimized 180° pulse length of 4.6-5.1 µs. [1]H-^{13}C FSLG HETCOR MAS spectra were obtained using the optimized ^{13}C CP MAS parameters and a contact time of 50 µs. For the [1]H(DQ)-[1]H(SQ) BABA experiment, one rotor period of the BABA recoupling was used for the excitation and reconversion of DQ coherence.[23] A nested 16-step phase cycle was used to select $\Delta p = \pm 2$ on the DQ excitation pulses (4 steps) and $\Delta p = -1$ (4 steps) on the z-filter 90° pulse, where p is the coherence order. The t_1 increment was set equal to the rotor period (the reciprocal of the MAS frequency) and the States-TPPI method was used to achieve sign discrimination in F1.

KBr was used for magic angle calibration. [13]C chemical shifts were referenced to the methylene carbon signal of adamantane at 38.48 ppm.[24] For all experiments with the 3.2 mm probe, the calibrated probe temperature was set to 296.4 K. The additional warming is the result of the frictional heating due to MAS. Based on temperature calibration this temperature corresponds to calibrated 324 K (20 kHz) and 340 K (24 kHz) (see chapter **SI 3**).

CASTEP

GIPAW (CASTEP) calculations were run on the local cluster of the institute except for the calculation of the chemical shieldings of the hydrate 912149, which were done on the cluster of the University of Bayreuth, Germany. They were performed using the CASTEP code,[25] academic release version 17.2. All structures were first geometry optimized with the unit cell parameters fixed before chemical shieldings were calculated using the GIPAW method.[18] In all calculations, the PBE exchange-correlation function was used.[26] For the plane-wave basis

set with ultra-soft pseudopotentials,[27] a maximum cut-off energy of 600 eV was used along-side a Monkhorst–Pack grid for sampling over the Brillouin zone with minimum sample spacing $0.1 \times 2\pi$ Å^{-1}. The enthalpy value continuously decreased and the forces, energies, and displacements of all calculated structures were converged to better than 0.05 eV/Å, 2×10^{-5} eV and 0.001 Å, respectively.

PXRD

Phase analysis was performed using X-ray powder diffraction (PXRD) with a Bruker Discover D8 powder diffractometer (Karlsruhe, Germany) using Cu K$_\alpha$ radiation (unsplit K$_{\alpha1}$ + K$_{\alpha2}$ doublet, mean wavelength λ = 1.5419 Å), a focusing Goebel mirror and a 2.5° axial Soller slit. Detection was done with a LynxEye-1D-Detector (Bruker AXS). Measurements were performed in reflection geometry in coupled two theta/theta mode with a step size of 0.025° in 2θ in the range of 5–50°. The samples were filled in a glass capillary (Hilgenberg ⌀ = 0.5 mm) and sealed. Data collection was done with the software package DIFFRAC.Suite (V2 2.2.690, BrukerAXS 2009–2011, Karlsruhe, Germany).

An additional X-ray diffraction experiment with *PTX Dry* for pawley refinement was carried out on a STOE STADI P diffractometer (Darmstadt, Germany) using Cu Kα_1 radiation (λ = 1.5406 Å) in Debye−Scherrer geometry. The diffractometer is equipped with a DECTRIS MYTHEN 1K detector and a Ge(111) monochromator. The sample was filled in a glass capillary (Hilgenberg ⌀ = 0.5 mm) under inert gas atmosphere, sealed and measured with a step size of 0.015° in 2θ in a range from 2 to 90°, 2.005 to 90.005° and 2.01 to 90.01°. The three measurements were subsequently merged, repeated once and summed up, resulting in a final step size of 0.005°. Data collection was done with the WinXPOW Program Package (V3.05, STOE & Cie GmbH 2011, Darmstadt, Germany).

Pawley Refinement

Pawley refinement was carried out using the TOPAS-Academic V6 software.[28] The fit indicators r$_{wp}$, r$_{exp}$ and *gof* (goodness of fit) were used to assess the quality of the refined lattice parameters. The initial profile in a reduced 2θ range from 3 to 70°, due to limited data intensity, was refined by five free background coefficients of a Chebyshev polynomial function, a zero point off-set, peak shape parameters of a modified Thomson-Cox-Hastings pseudo-Vogt function, a simple axial model to fit peak asymmetry, a linear absorption coefficient, and the lattice parameters *a*, *b* and *c*.[29]

Material Studio

The unit cell was modeled with the program Accelrys *Materials Studio 4.4.* using P2$_1$2$_1$2$_1$ symmetry restriction and given cell parameters from the Pawley refinement.

DSC

2.89 mg paclitaxel were placed in a flat-bottom aluminum pan with crimped-on lids and inserted into a calibrated DSC 204 F1 Phoenix equipped with a CC200 F1 Controller (NETZSCH, Selb, Germany). The heating rate was 10 °C/min (25-225 °C). All scans were recorded under nitrogen atmosphere.
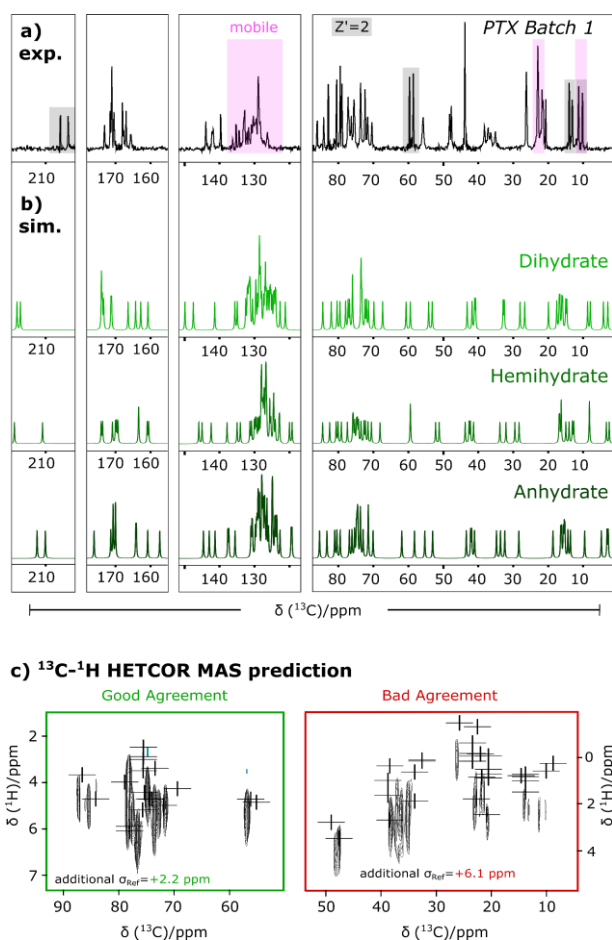
Results and discussion

PTX Batch 1

Figure 1a: ^{13}C CP MAS NMR spectrum of *PTX Batch 1*, recorded at 14.1 T and 24 kHz MAS spinning rate with a contact time of 2.5 ms, 1756 co-added transients and a recycle delay of 2.5 s.
Figure 1b: simulated NMR spectra based on the different PTX structures shown in Table 1.
Figure 1c: Extracts from a [1]H-^{13}C FSLG HETCOR MAS spectrum of *PTX Batch 1* with overlayed calculated NMR shifts of the published anhydrate structure (Table 1). For full spectrum see Figure S7.

To facilitate a complete assignment of both individual molecules in crystalline paclitaxel, a two-step procedure was intended: The first step aimed at the assignment of the ^{13}C NMR data through combination with GIPAW (CASTEP)[18, 25] calculations followed by a second step, the analysis of the ^{1}H chemical shifts employing 1D and 2D ^{1}H NMR data at high field and fast MAS, [1]H-^{13}C FSLG-HETCOR correlations and the results from the quantum chemical calculations. Consequently, ^{13}C CP MAS data for PTX used as received was recorded at 24 kHz MAS and 14.1 T (**Figure 1a**). In agreement with the previous solid-state NMR work on PTX,[8-9] the well resolved ^{13}C NMR spectrum shows two sets of carbon resonances due to the two individual molecules in the asymmetric unit of the crystal structure. This becomes easily apparent for the ketone resonance above 200 ppm as well as for the methyl signals around 10 ppm and other separated signals (e.g. at ~ 60 ppm) stemming from the rigid baccatin core of the PTX molecule (highlighted in grey). Additionally, ^{13}C direct exci-

tation experiments (**Figure S6**) with short interscan delay served to identify mobile functional groups in the molecule (highlighted in blue), namely two methyl groups and phenyl moieties, again matching previous findings in the literature.[8-9]

For the complete assignment of the ^{13}C NMR signals to the individual molecules PTX-A and PTX-B, calculation of the chemical shieldings based on existing structures from X-ray diffraction data is essential. Therefore, in a first step, the dihydrate crystal structure of PTX (CCDC number: 912149, Table 1) was used as input for calculations of solid-state NMR parameters with the program package CASTEP due to it being based on high quality synchrotron X-ray diffraction data. After successful completion, subsequent calculations were also performed for the two other less hydrated and anhydrous structures (CCDC numbers: 912148 and 912147) obtained from X-ray powder diffraction at elevated temperatures. In general, all structures were geometry optimized carefully (parameter evolution see **SI 1**) before subjecting them to the calculation of NMR parameters. The geometry optimization was particularly challenging and time consuming as the crystallographic unit cell, the starting point for these calculations, contains 900 to almost 1000 atoms depending on the individual water content. This is starting to fall into the range of what is referred to as large scale quantum mechanical calculations in the literature and for which generally other dedicated and specific large-scale treatments are in the research focus.[30] As the computational time for large simulations in CASTEP scales approximately cubically with the number of atoms, the calculations in this project are amongst the largest NMR calculations run so far with this software package. Despite using the low memory version of the Broyden-Fletcher–Goldfarb-Shanno (L-BFGS) algorithm[31] for the geometry optimization, overall durations for the optimization were in the range of 45-60 days per structure using 300 GB of memory on our local cluster. The consecutive calculations of the NMR parameters were completed after 15 days (hemihydrate) and 31 days (anhydrate) using analogous settings and the corresponding referenced chemical shifts plotted in **Figure 1b** with a line broadening of 0.1 ppm ((σ_{Ref}(^{13}C) = 166.99 ppm, σ_{Ref}(^{1}H) = 29.43 ppm)). The general features and signal areas in the experimental spectrum are also found in the calculated spectra, which is particularly noticeable for the signal region from 70 to 90 ppm as well as between 120 and 150 ppm. However, upon analyzing the individual chemical shift predictions more carefully, it becomes apparent that there are multiple carbon atoms, of which the chemical shift deviates more strongly from the experimental value than expected based on the average error margin of ±2 ppm[17f, 32] established for this type of calculations on purely organic molecules. Focusing on the ppm range below 40 ppm and considering the banana effect (high chemical shifts are predicted too high, low ones too low) often observed for ^{13}C chemical shift calculations,[33] the dihydrate structure calculation seems to agree best with the experimental data. On the other hand, the agreement between experimental and calculated chemical shifts for this structure is rather poor for the spectral region from 160 to 180 ppm. Interestingly, analogous considerations can be made for the two other comparisons. This apparent disagreement between experimental data and any of the calculated structures becomes also particularly apparent in 2D NMR data, e.g. the extracts from the ^{1}H-^{13}C FSLG HETCOR spectrum recorded to facilitate
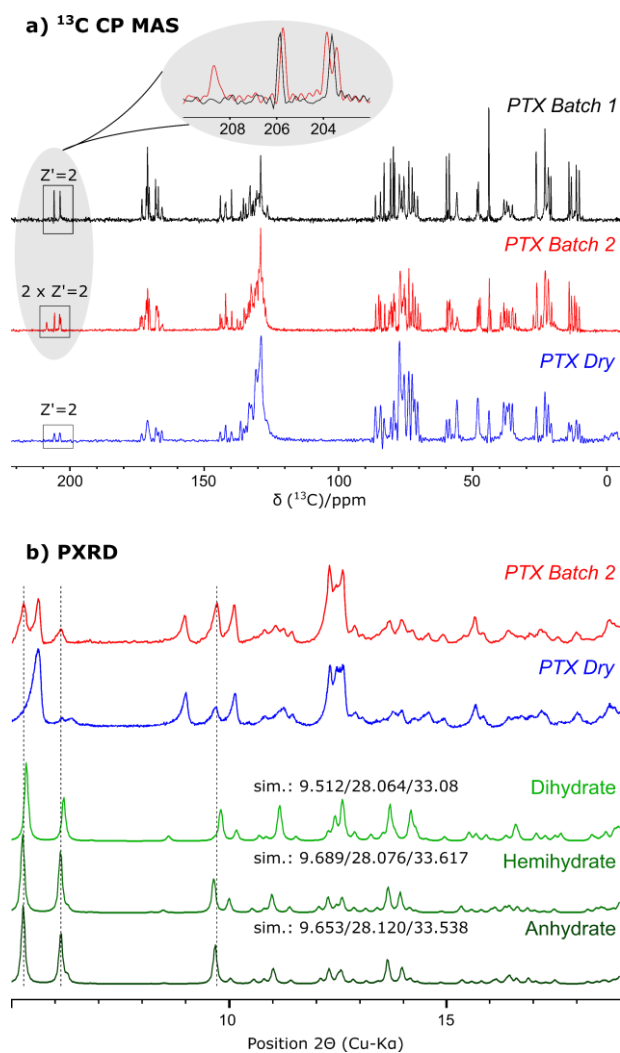
Figure 2a: ^{13}C CP MAS NMR spectra of *PTX Batch 1* (black), *PTX Batch 2* (red) and *PTX Dry* (blue). They were recorded with the following parameter (co-added transients/spinning frequency/contact time/recycle delay, the latter individually optimized to the measured spin-lattice relaxation times): 1756/24 kHz/2.5 ms/2.5 s (*PTX Batch 1*), 932/11 kHz/2.0 ms/5.0 s (*PTX Batch 2*), 10240/20 kHz/2.0 ms/4.0 s (*PTX Dry*).

Figure 2b: experimental PXRD data of *PTX Batch 2* and *PTX Dry* (top) as well as simulated PXRD spectra of the published PTX structures from Table 1.

complete signal assignment and shown in **Figure 1c** (full spectrum **Figure S7**). Together with the 2D NMR data and despite the discrepancies in the calculations, the majority of the ^{13}C chemical shifts could be successfully assigned to the individual molecules and we could identify some of the more strongly deviating carbon atoms to be in proximity to water molecules in the dihydrate structure. As the water molecules in the structure are loosely bound and therefore not likely to be in a fixed position during the room temperature measurements, we hypothesized this to be the source for the observed deviations between experiment and calculation, which we planned to confirm with further experiments, e.g. variable temperature measurements, before proceeding to the analysis of the more crowded ^1H NMR data.

PTX Batch 2

At this stage of the project, we purchased a second batch of PTX, which will be referred to as *PTX Batch 2*. We immediately saw that this new batch yielded NMR spectra with more signals than observed for *PTX Batch 1*. Comparison of the ^{13}C NMR spectra (**Figure 2a**), particularly in the ketone area above 200 ppm, showed that there is one set of signals at 204 and 206 ppm found in both datasets while a new additional set of two more signals appears at 203 and 209 ppm (highlighted and enlarged in grey). The presence of a second set of signals is also confirmed by ^{15}N NMR data published as part of a previous investigation on PTX formulations.[21] To confirm the presence of this second phase, X-ray powder diffraction data was recorded and compared to the simulated diffraction patterns for the three published PTX crystal structures (**Figure 2b**). For clarity, only the data at low 2Θ values is shown and the reader is referred to **Figure S9** for the complete PXRD datasets. Through this comparison, the reflections belonging to the previously published

PTX phases can be identified in the experimental PXRD diffractogram of *PTX Batch 2* (indicated by vertical lines). However, additional reflections are observed at 5.6° and 9.0° 2Θ indicating – in agreement with the NMR spectroscopic data – the presence of a second, unknown phase. Furthermore, the calorimetric profile resulting from DSC measurements generally matched the data found for hydrated PTX in the literature,[34] albeit with small, but noticeable differences (**Figure S8**). Elemental analysis of *PTX Batch 2* further substantiates the hypothesis of two distinct phases as it yielded a composition, which is between the values expected for the anhydrate and the dihydrate (**Table S2**). To clarify whether *PTX Batch 2* contains a hydrous and an anhydrous phase or two differently hydrated phases, the as-received *batch 2* was carefully dried under vacuum while moderately heating the sample to 70°C. Repeated PXRD measurements now yielded only the peaks of the previously unknown phase. Therefore, the experimental diffraction data confirms the presence of one hydrous phase and a new, anhydrous phase. Analogously, the ^{13}C CP MAS spectrum of the dried sample also contains only one phase. Interestingly, this spectrum is also identical to the ^{13}C NMR spectrum of *PTX Batch 1*. This closes the first cycle as the complete *PTX Batch 1* and one of the two phases of *PTX Batch 2* are composed of a to date unpublished, anhydrous crystalline arrangement with different cell parameters compared to the published data. This explains very convincingly, why none of the calculated parameters agrees sufficiently with the experimental solid-state NMR data.
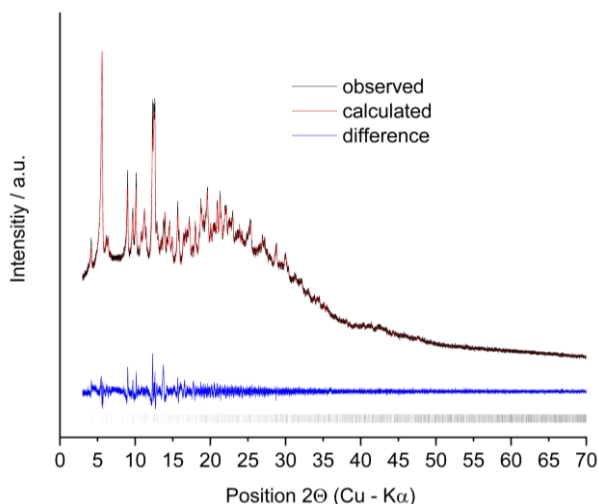
Structure Modelling of the New Anhydrous Phase

Figure 3: Diffraction pattern for *PTX Dry* (black line), calculated structure using Pawley refinement (red line) with R_{wp}=2.36%, R_{exp}=1.41% and Goodness of fit: 1.67, difference curve (blue) and hkl positions (black ticks).

For further investigations of the observed new phase, a sample of *PTX Dry* was packed and sealed in a glass capillary under inert gas atmosphere to protect the sample from moisture. This sample was used to collect powder diffraction data in a long-term measurement for good data quality. With this PXRD dataset, cell indexing (space group $P2_12_12_1$) and a Pawley refinement (**Figure 3**) was carried out to obtain refined lattice parameters (a 28.643(5), b 31.256(8), c 9.533(2)). This new unit cell has a 6.2%
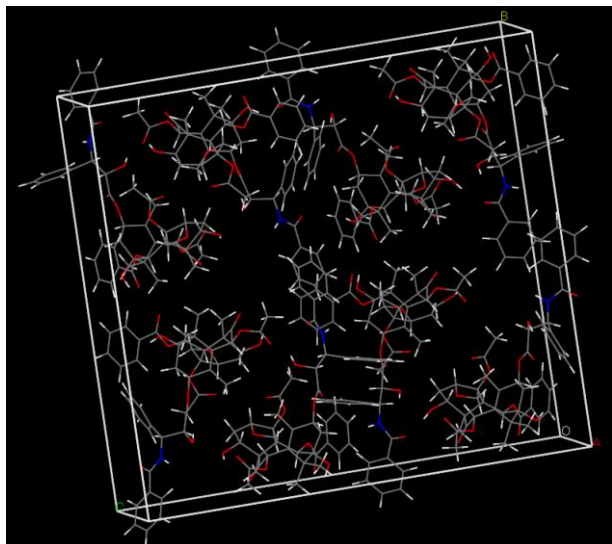
Figure 4: Unit cell of the investigated structure of PTX Dry created by Materials Studio and without further geometry optimization so far, as this is still an ongoing process at the time of submission of this thesis.

smaller volume than the unit cell of the published anhydrate (Table 1). Considering that during the drying process of the sample the water molecules must first escape the crystal structure, which then undergoes a restructuring resulting in this reduced volume, these cell parameters could build the unit cell of a fully relaxed crystal structure. The sample was prepared by drying over a long period of time and simultaneously heating. It has been shown that a shorter drying time without heating the sample leads to a more amorphous structure, which we attribute to the slow rearrangement to a stable structure (see **SI 11**).

Since the anhydrous structure by Vella-Zarb et. al.[10] was obtained in-situ and the time-frame therefore even faster than this shorter time period, the new unit cell and structure can be described as a relaxed version of their data. The observed high background intensities in the PXRD pattern can be attributed to the used glass capillary, which is confirmed by the measurement of an empty capillary (**Figure S12**). The software Materials Studio was used to create a unit cell of our investigated structure using these refined lattice parameters, space group, and the structural information of Z'=2 (**Figure 4**). Currently (12/2020), the resulting structure is still under geometry optimization.

Structural Elucidation

Since the geometry optimization of the structures of **Table 1** took up to 60 days, it is expected that this new structure will require at least 60-120 days for optimization because there is no pre-optimization of this structure in Materials Studio. Therefore, the geometry optimization and the subsequent calculation of chemical shifts of this newly obtained structure will be finished after submission of this thesis and thus, the following assignments are based on the geometry-optimized structure of the anhydrate (**Table 1**). The calculated chemical shifts of the published anhydrate serve only as a basis for the assignments and are supplemented by experimental [1]H-^{13}C HETCOR as well as fast MAS (100 kHz) 1D and 2D ^{1}H data. *PTX Dry* is used for this ^{13}C as well as ^{1}H signal assignment, as it contains the new anhydrous structure and is free from the second phase of *PTX Batch 2*. **Figure 5a** shows ^{1}H MAS NMR spectra of crystalline *PTX Batch 1* recorded at different magnetic field strength and different spinning rates as well as a very fast ^{1}H MAS NMR spectrum at 100 kHz spinning speed of *PTX Dry*. The increase of
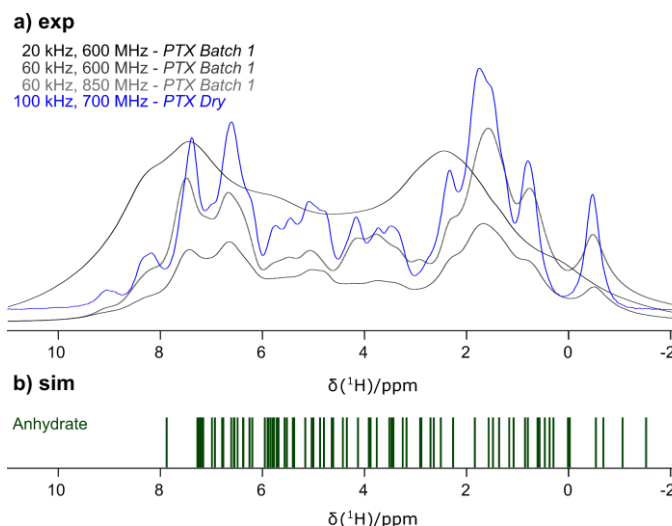
a) exp
20 kHz, 600 MHz - *PTX Batch 1*
60 kHz, 600 MHz - *PTX Batch 1*
60 kHz, 850 MHz - *PTX Batch 1*
100 kHz, 700 MHz - *PTX Dry*

b) sim

Anhydrate

Figure 5a: ^{1}H MAS NMR spectra of *PTX Batch 1* (blue, red, and green) and *PTX Dry* (purple) recorded at different spinning rates and different magnetic field strengths.
Figure 5b: GIPAW (CASTEP) calculated chemical shifts of the anhydrate PTX structure of Table 1, represented in bars. This structure was geometry-optimized before the calculation of the chemical shifts.

the magnetic field and the spinning frequency result in an augmented number of up to 17 detected ^{1}H MAS peaks for more than 100 different protons in the asymmetric unit of PTX. The result of the calculation of the proton chemical shifts from the anhydrate structure in **Table 1** is shown in **Figure 5b**. The experimental ^{1}H MAS data show a good separation of the NH protons (for more detailed information on this topic see Grüne *et al.*[21]) and a separation of the methyl groups. Nevertheless, even the spectrum at 100 kHz MAS frequency still shows strong overlap of the proton signals. Therefore, 2D correlation NMR spectra are needed to achieve a tentative assignment of the proton data.

The [1]H-^{13}C FSLG HETCOR MAS spectrum of *PTX Dry* (**Figure S14**) at a MAS frequency of 20 kHz with a short contact time of 50 µs shows closest [1]H-^{13}C proximities via through-space dipolar interactions, i. e. for this contact time the protons directly bound to the corresponding carbon atoms. The indirect measurement of the proton chemical shifts enables a significantly improved resolution in the ^{1}H dimension. An assignment of the [13]C-^{1}H proximities of the aromatic region (^{13}C chemical shifts above 120 ppm) is not possible due to the low resolution and the overlap of the signals. For the evaluation, the signals that were well separated from other signals were first examined. Afterwards, the focus was set on each signal which can be clearly assigned. Subsequently, these unambiguous results are then used for the evaluation of the more complex [1]H(DQ)-[1]H(SQ) BABA MAS spectrum (**Figure 6**). In such a spectrum, double-quantum correlation peaks indicate close through-space proximity between protons. The peaks appear at a value corresponding to the sum of the single-quantum chemical shifts of the individual protons. For further details, the reader is referred to Schnell *et al.*[23b] who published the first ^{1}H DQ MAS spectra using this rotor-synchronized BABA recoupling sequence, or to the review about ^{1}H DQ MAS measurements of S. P. Brown[35]. In principle, the evaluation of

this spectrum follows the same way as for the [1]H-^{13}C HETCOR MAS spectrum. Nevertheless, while the latter is limited to interactions between directly bonded ^{1}H and ^{13}C atoms due to the short contact time, through [1]H(DQ)-[1]H(SQ) BABA MAS spectra, interactions between protons with a distance of 3.5-4.0 Å are typically observed, which significantly increases the total number of possible interactions partners.
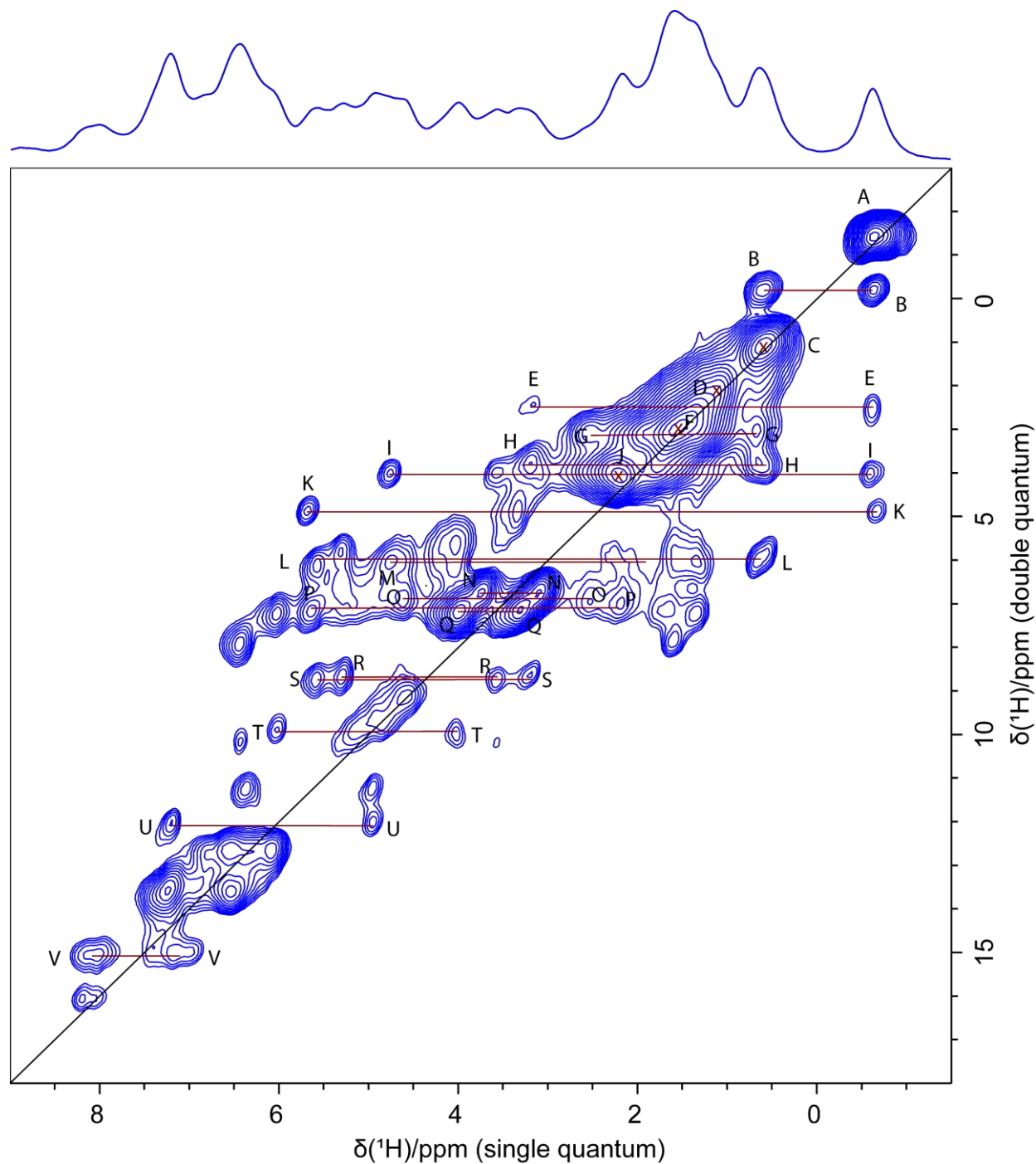
Figure 6: [1]H(DQ)-[1]H(SQ) MAS NMR correlation spectrum of *PTX Dry* (with external ^{1}H one-pulse NMR spectrum) recorded using one rotor period of BABA recoupling at 16.4 T and 100 kHz spinning rate. 432 t_1 FIDs were measured each with 16 co-added transients for a recycle delay of 1.5 s (experimental time: 2h 53 min).

Therefore, the peaks were assigned in a repetitive iterative process based on the anhydrate structure from **Table 1** and supported by the ^{1}H-^{13}C HETCOR MAS data. **Table 2** shows the result of the ^{1}H(DQ)-^{1}H(SQ) BABA MAS spectrum containing the single-quantum as well as the corresponding double-quantum chemical shifts of the labeled peaks together with their shortest distance in the crystal structure. For peaks originating from methyl group protons interacting with themselves, a distance specification was omitted. **Table 3** summarizes all extracted ^{1}H chemical shift values which can be assigned to a certain proton of a certain molecule of the asymmetric unit cell, sorted by chemical shift values. If an assignment of the ^{13}C chemical shift in the ^{1}H-^{13}C HETCOR MAS spectrum is possible, it is listed as well.

Table 2: ^{1}H DQ correlations observed in *PTX Dry* in Figure 6, together with the corresponding shortest distances obtained from the geometry optimized anhydrate structure (Table 1). This table lists the carbon atoms to which the protons are attached. Label A and B mark the corresponding PTX molecule in its asymmetric unit. Superscript numbers distinguish between two protons for CH$_2$ groups.

	Carbon	δ_{SQ_1} / ppm	Carbon	δ_{SQ_2} / ppm	δ_{DQ} / ppm	Separation / Å
A	A16	-0.6	A16	-0.6	-1.2	-
B	B17	0.6	A16	-0.6	0.0	2.5
	A17	0.6	B16	-0.6		2.7
C	A17	0.6	B17	0.6	1.2	5.8
	B17	0.6	A17	0.6		
D	A19	1.1	A19	1.1	2.2	-
E	A20^2	3.1	A16	-0.6		2.6
F	B19	1.5	B19	1.5	3.0	-
	A29	1.5	A29	1.5		-
	A31	1.5	A31	1.5		-
	B31	1.5	B31	1.5		-
	B31	1.5	A31	1.5		-
G	B6^1	2.5	B6^2	0.7	3.2	2.4
H	A20^2	3.2	B17	0.6	3.8	3.0
	B20	3.2	A17	0.6		3.0
	B1OH	3.2	B17	0.6		2.2
I	B13	4.8	B16	-0.6	4.2	1.9
	A13	4.8	A16	-0.6		1.8
J	B29	2.2	B29	2.2	4.4	-
K	PhA22	5.7	A16	-0.7	5.0	2.9
L	A2	5.6	A17	0.6	6.2	2.0
	B2	5.6	A17	0.6		3.5
M	A3'	4.8	A2'OH	1.7	6.5	2.8
N	A20^1	3.7	A20^2	3.1	6.8	1.8
O	B13	4.6	B14	2.5	7.1	2.4
	B5	4.6	B6^1	2.5		2.3
	A5	4.6	A6^1	2.5		2.3
	A5	4.6	A6^2	2.5		2.8
P	A7OH	5.6	B14	2.2	7.8	2.3
Q	B20^1	4.0	B20^2	3.2	7.3	1.8
R	A7	5.3	A3	3.6	8.9	2.2
	B7	5.3	B3	3.6		2.4
S	A2	5.6	A20	3.2	8.8	2.9
T	B27	6.0	B20^1	4.0	10.0	2.6
U	A42	7.2	A3'	5.0	12.2	2.4
	B42	7.2	B3'	5.0		2.3
V	BNH	8.1	B38	7.1	15.2	2.7

Table 3: Partial assignment of the ^{1}H chemical shifts and its corresponding ^{13}C chemical shifts based on the [1]H(DQ)-[1]H(SQ) BABA MAS spectrum and the [1]H-^{13}C HETCOR MAS spectrum. Label A and B mark the corresponding PTX molecule in its asymmetric unit.

δ(^{1}H) / ppm	δ(^{13}C) / ppm	Carbon	δ(^{1}H) / ppm	δ(^{13}C) / ppm	Carbon
-0.6	26.2	A16	3.6	47.9	A3
	26.2	B16		47.9	B3
0.6	21.7	A17 / B17	3.7	73.7	A20^1
	21.7	A17 / B17	4.0	73.7	B20^1
0.7	37.2	B6^2	4.6	70.4	B13
1.1	10.2	A19		84.3	B5
1.3	13.2	A18		86.1	A5
1.5	11.3	B19	4.8	70.4	B13
	23.0	A29		71.6	A13
	23.0	A31		55.8	A3'
		B31	5.0	55.8	A3'
1.7		A2'OH		55.8	B3'
1.8	14.0	B18	5.3		A7
1.9	35.2	A14			B7
2.2	20.6	B29	5.6		A2
	36.5	B14			B2
2.5	37.2	B6^1			A7OH
	38.3	A6^1	5.7		PhA22
	38.3	A6^2	6.0		A10, B10
	36.5	B14	6.0		B27
3.1	73.7	A20^2	7.1		A38
3.2	73.7	B20^2	7.2		A42
		B1OH			B42

As demonstrated by the results summarized in **Table 3**, the combination of the applied experimental and computational techniques enables a variety of ^{1}H NMR chemical shifts of PTX to be assigned for the first time. With the help of the newly obtained structure of PTX Dry, for which geometry optimization is currently performed, remaining ambiguities of the assignments should be significantly reduced.

Summary and conclusion
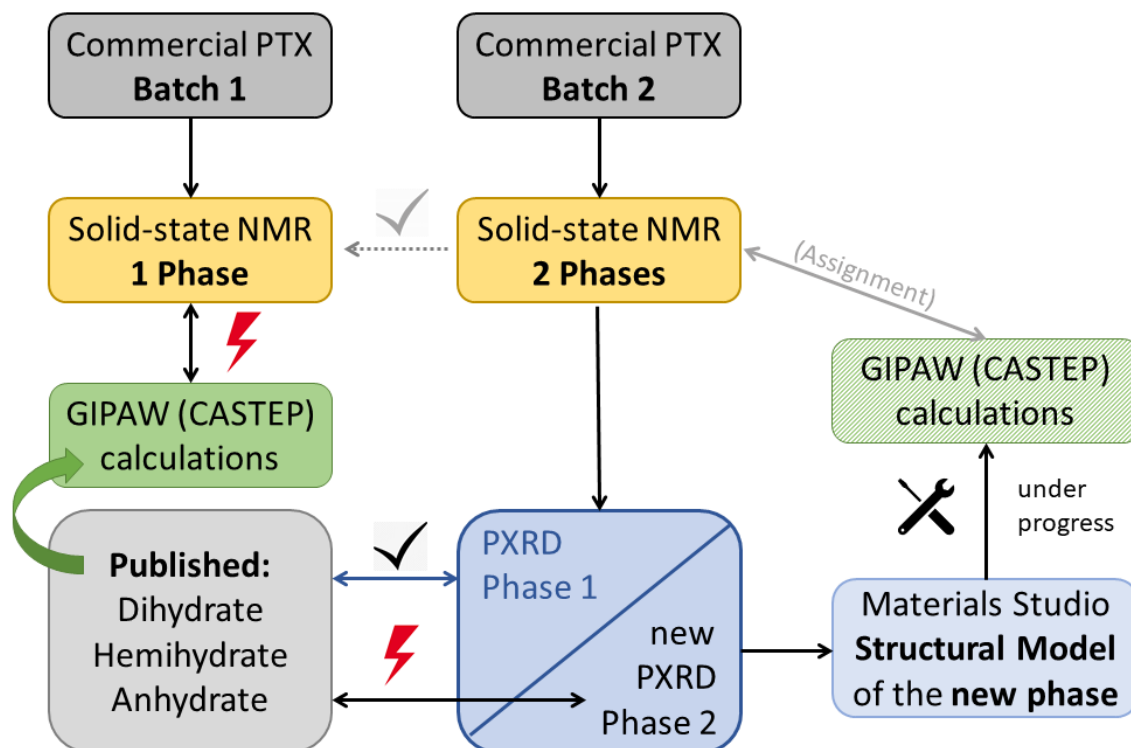
Scheme 2: Schematic representation of the results of this chapter.

In this work, two different commercially available batches of PTX were investigated, named *PTX Batch 1* and *PTX Batch 2,* which is schematically represented in **Scheme 2.** Solid-state NMR as well as PXRD data together with geometry optimization and calculation of NMR chemical shifts revealed the existence of an identical and so far unknown PTX phase in both baches. In contrast to *PTX Batch 1*, *PTX Batch 2* consists of an additional phase that was similar to a known hydrous form characterized by Vella-Zarb *et. al.*[10]. By drying *PTX Batch 2* under vacuum for ten days (three days at 70°C and seven days at room temperature), it is completely transformed to the new phase, which we therefore named *PTX Dry*. We could show that a shorter drying time leads to a more amorphous state, which we attribute to the slow rearrangement to a stable structure. Since the drying conditions to obtain the anhydrous PTX structure described by Vella-Zarb et. al.[10] were even faster than this shorter time period, we identify our phase as a relaxed version of the anhydrate structure published by Vella-Zarb *et al.*

^{13}C solid-state NMR data of *PTX Dry* showed that it contains two molecules in the asymmetric unit. Pawley refinement was used to determine refined lattice parameters from PXRD data of *PTX Dry*. With the help of Material Studios, a new cell structure was created, which is currently undergoing geometry optimization.

The anhydrate structure of Vella-Zarb *et. al.*[10], 1D ^{13}C CP MAS data as well as ^{1}H-^{13}C HETCOR MAS and ^{1}H(DQ)-^{1}H(SQ) BABA MAS spectra at up to 100 kHz spinning frequency allowed ^{13}C and first partial ^{1}H assignments for PTX Dry. At this stage of the project, these investigations had to be done without the chemical shielding calculations of the newly obtained crystal phase. In the future, the chemical shielding calculations of this new structure will allow the assignment of more cross-peaks in experiments such as ^{1}H(DQ)-^{1}H(SQ) BABA MAS as well as a more precise and more detailed assignment of the ^{13}C chemical shifts. While the PXRD results in this work nicely show how to make use of long-range information for the investigations of both phase and unit cell of this large structure, the solid-state NMR investigation with its sensitivity to short-range information enables the structural elucidation at an atomic level even for complex solid materials as PTX, an important milestoone for further investigation of PTX together with pharmaceutical excipients.

References

[1] M. E. Wall, M. C. Wani, *153rd National Meeting, American Chemical Society* **1967**.

[2] M. E. Wall, M. C. Wani, *J. Ethnopharmacol.* **1996**, *51*, 239-254.

[3] Harshita, M. A. Barkat, SarwarBeg, F. H. Pottoo, F. J. Ahmad, *Nanomedicine* **2019**, *14*, 1323-1341.

[4] a) S. B. Horwitz, D. Cohen, S. Rao, I. Ringel, H. J. Shen, C. P. Yang, *J. Natl. Cancer Inst. Monogr.* **1993**, 55-61; b) D. M. Bollag, P. A. McQueney, J. Zhu, O. Hensens, L. Koupal, J. Liesch, M. Goetz, E. Lazarides, C. M. Woods, *Cancer Res.* **1995**, *55*, 2325-2333.

[5] M. C. Wani, H. L. Taylor, M. E. Wall, P. Coggon, A. T. McPhail, *J. Am. Chem. Soc.* **1971**, *93*, 2325-2327.

[6] D. Mastropaolo, A. Camerman, Y. Luo, G. D. Brayer, N. Camerman, *Proc. Natl. Acad. Sci. USA* **1995**, *92*, 6920-6924.

[7] a) Q. Gao, S.-H. Chen, *Tetrahedron Lett.* **1996**, *37*, 3425-3428; b) Q. Gao, J. Golik, *Acta Crystallogr C* **1995**, *51*, 295-298; c) Q. Gao, W. L. Parker, *Tetrahedron* **1996**, *52*, 2291-2300.

[8] J. K. Harper, D. H. Barich, E. M. Heider, D. M. Grant, *Cryst. Growth Des.* **2005**, *5*, 1737-1742.

[9] E. M. Heider, J. K. Harper, D. M. Grant, *Phys. Chem. Chem. Phys.* **2007**, *9*, 6083-6097.

[10] L. Vella-Zarb, U. Baisch, R. E. Dinnebier, *J. Pharm. Sci.* **2013**, *102*, 674-683.

[11] N. Qiao, M. Li, W. Schlindwein, N. Malek, A. Davies, G. Trappitt, *Int. J. Pharm.* **2011**, *419*, 1-11.

[12] A. M. Sofias, M. Dunne, G. Storm, C. Allen, *Adv. Drug Delivery Rev.* **2017**, *122*, 20-30.

[13] a) M. Callari, P. L. De Souza, A. Rawal, M. H. Stenzel, *Angew. Chem. Int. Ed.* **2017**, *56*, 8441-8445; b) C. Cao, J. Zhao, F. Chen, M. Lu, Y. Y. Khine, A. Macmillan, C. J. Garvey, M. H. Stenzel, *Chem. Mater.* **2018**, *30*, 5227-5236; c) E. Procházková, C. Cao, A. Rawal, M. Dračínský, S. Bhattacharyya, I. Císařová, J. M. Hook, M. H. Stenzel, *ACS Applied Mater. Interfaces* **2019**, *11*, 28278-28288; d) M. Urbanova, M. Gajdosova, M. Steinhart, D. Vetchy, J. Brus, *Mol. Pharm.* **2016**, *13*, 1551-1563; e) A.-C. Pöppler, M. M. Lübtow, J. Schlauersbach, J. Wiest, L. Meinel, R. Luxenhofer, *Angew. Chem. Int. Ed.* **2019**, *58*, 18540-18546.

[14] a) Y. Nishiyama, S. P. Brown, Z. Gan, L. Delevoye, L. O'Dell, D. Reichert, M. Vogel, D. Arcon, J. Stebbins, H. Heise, *Modern Methods in Solid-state NMR: A Practitioner's Guide*, Royal Society of Chemistry, **2018**; b) P.-H. Chien, K. J. Griffith, H. Liu, Z. Gan, Y.-Y. Hu, *Annual Review of Materials Research* **2020**, *50*.

[15] a) D. Singh, P. V. Marshall, L. Shields, P. York, *J. Pharm. Sci.* **1998**, *87*, 655-662; b) J. C. Burley, M. J. Duer, R. S. Stein, R. M. Vrcelj, *Eur. J. Pharm. Sci.* **2007**, *31*, 271-276; c) F. G. Vogt, G. R. Williams, M. N. Johnson, R. C. B. Copley, *Cryst. Growth Des.* **2013**, *13*, 5353-5367; d) N. Zencirci, U. J. Griesser, T. Gelbrich, D. C. Apperley, R. K. Harris, *Mol. Pharm.* **2014**, *11*, 338-350; e) C. M. Widdifield, S. O. Nilsson Lill, A. Broo, M. Lindkvist, A. Pettersen, A. Svensk Ankarberg, P. Aldred, S. Schantz, L. Emsley, *Phys. Chem. Chem. Phys.* **2017**, *19*, 16650-16661.

[16] K. M. Steed, J. W. Steed, *Chem. Rev.* **2015**, *115*, 2895-2933.

[17] a) R. K. Harris, R. E. Wasylishen, M. J. Duer, *NMR Crystallography*, John Wiley & Sons, **2010**; b) C. Bonhomme, C. Gervais, F. Babonneau, C. Coelho, F. Pourpoint, T. Azaïs, S. E. Ashbrook, J. M. Griffin, J. R. Yates, F. Mauri, C. J. Pickard, *Chem. Rev.*

2012, *112*, 5733-5779; c) C. Martineau, J. Senker, F. Taulelle, in *Annual Reports on NMR Spectroscopy, Vol. 82* (Ed.: G. A. Webb), Academic Press, **2014**, pp. 1-57; d) S. E. Ashbrook, D. McKay, *Chem. Commun.* **2016**, *52*, 7186-7204; e) G. J. O. Beran, *Chem. Rev.* **2016**, *116*, 5567-5613; f) P. Hodgkinson, *Prog. Nucl. Magn. Reson. Spectrosc.* **2020**, *118-119*, 10-53.

[18] a) C. J. Pickard, F. Mauri, *Phys. Rev. B* **2001**, *63*; b) J. R. Yates, C. J. Pickard, F. Mauri, *Phys. Rev. B* **2007**, *76*.

[19] A. L. Webber, L. Emsley, R. M. Claramunt, S. P. Brown, *J. Phys. Chem. A* **2010**, *114*, 10435-10442.

[20] G. N. M. Reddy, D. S. Cook, D. Iuga, R. I. Walton, A. Marsh, S. P. Brown, *Solid State Nucl. Magn. Reson.* **2015**, *65*, 41-48.

[21] M. Grüne, R. Luxenhofer, D. Iuga, S. P. Brown, A.-C. Pöppler, *J. Mater. Chem. B* **2020**, *8*, 6827-6836.

[22] B. Fung, A. Khitrin, K. Ermolaev, *J. Magn. Reson.* **2000**, *142*, 97-101.

[23] a) W. Sommer, J. Gottwald, D. Demco, H. W. Spiess, *J. Magn. Res., Ser. A* **1995**, *113*, 131-134; b) I. Schnell, A. Lupulescu, S. Hafner, D. E. Demco, H. W. Spiess, *J. Magn. Reson.* **1998**, *133*, 61-69.

[24] C. R. Morcombe, K. W. Zilm, *J. Magn. Reson.* **2003**, *162*, 479-486.

[25] S. J. Clark, M. D. Segall, C. J. Pickard, P. J. Hasnip, M. I. Probert, K. Refson, M. C. Payne, *Z. Kristallogr.* **2005**, *220*, 567-570.

[26] J. P. Perdew, K. Burke, M. Ernzerhof, *Phys. Rev. Lett.* **1996**, *77*, 3865-3868.

[27] D. Vanderbilt, *Phys. Rev. B* **1990**, *41*, 7892.

[28] A. A. Coelho, *Coelho Software, Brisbane, Australia* **2007**.

[29] P. Thompson, D. Cox, J. Hastings, *J. Appl. Crystallogr.* **1987**, *20*, 79-83.

[30] L. E. Ratcliff, S. Mohr, G. Huhs, T. Deutsch, M. Masella, L. Genovese, *WIREs Comput Mol Sci* **2017**, *7*, e1290.

[31] a) C. G. Broyden, *J. Inst. Math. Its Appl.* **1970**, *6*, 222-231; b) R. Fletcher, *Comp. J.* **1970**, *13*, 317-322; c) D. Goldfarb, *Math. Comp.* **1970**, *24*, 23-26; d) D. F. Shanno, P. C. Kettler, *Math. Comp.* **1970**, *24*, 657-664.

[32] E. Salager, G. M. Day, R. S. Stein, C. J. Pickard, B. Elena, L. Emsley, *J. Am. Chem. Soc.* **2010**, *132*, 2564-2566.

[33] R. K. Harris, P. Hodgkinson, C. J. Pickard, J. R. Yates, V. Zorin, *Magn. Reson. Chem.* **2007**, *45*, S174-S186.

[34] R. T. Liggins, W. Hunter, H. M. Burt, *J. Pharm. Sci.* **1997**, *86*, 1458-1463.

[35] S. P. Brown, *Prog. Nucl. Magn. Reson. Spectrosc.* **2007**, *4*, 199-251.

Supporting Information

New anhydrous crystalline phase of paclitaxel revealed by solid-state NMR spectroscopy, powder X-ray diffraction and complementary quantum chemical calculations

Marvin Grüne[a], Dominik Heuler[b], Klaus Müller-Buschbaum[b], and Ann-Christin Pöppler[a]*

[a] *Institute of Organic Chemistry, University of Würzburg, Am Hubland, 97074 Würzburg, Germany*
[b] *Lehrstuhl für Chemische Technologie der Materialsynthese, University of Würzburg, Röntgenring 11, 97070 Würzburg, Germany*

Supporting Information

Content:

SI 1: Evolution of CASTEP geometry optimization parameters

SI 2: Chemical shifts of the anhydrate (CCDC 912147)

SI 3: Temperature calibration of the 3.2 mm CP MAS probe for 600 MHz

SI 4: ^{13}C direct excitation MAS spectrum

SI 5: ^{1}H-^{13}C FSLG HETCOR MAS spectrum of PTX Batch 1

SI 6: DSC measurements of PTX Batch 1

SI 7: Elemental analyses of PTX Batch 2

SI 8: Complete PXRD data

SI 9: Preparation, NMR data, and PXRD data of amorphous PTX

SI 10: Diffraction pattern of PTX Dry and an empty capillary

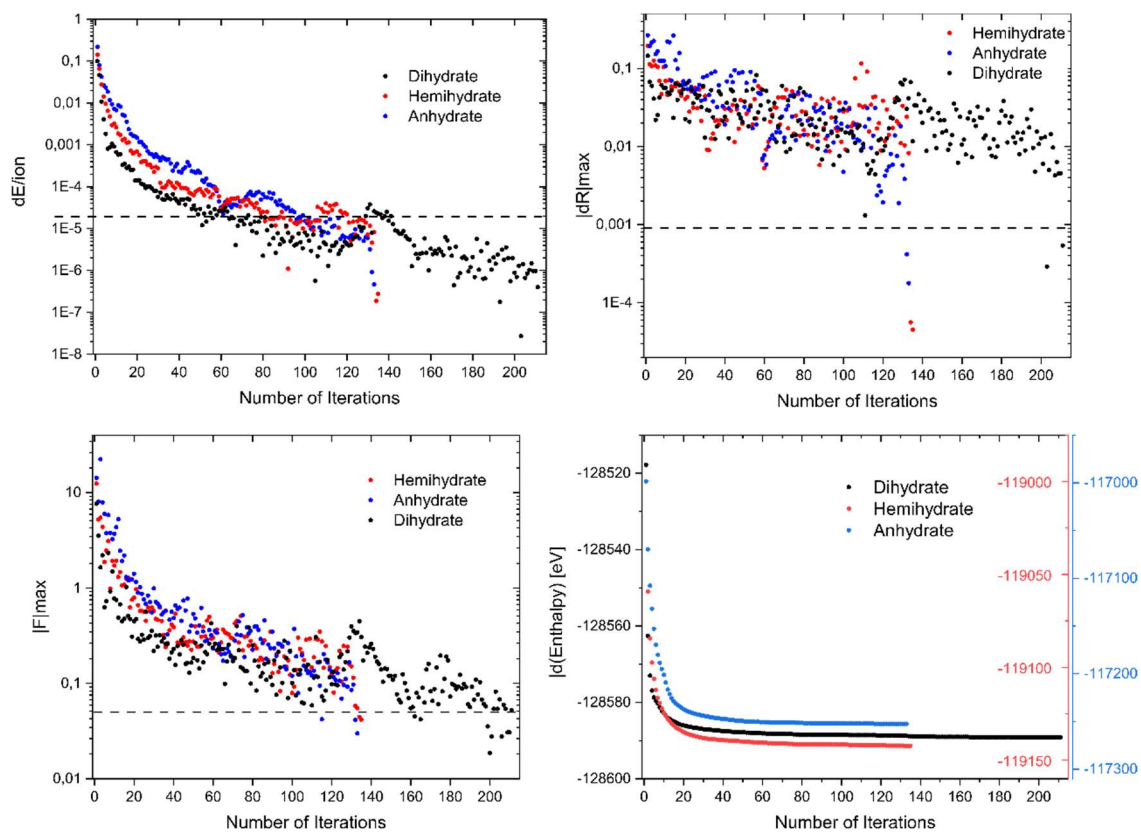**SI 11:** Preparation and NMR data of PTX Dry

SI 12: References

SI 1: Evolution of CASTEP geometry optimization parameters

Figure S1: Evolution of different CASTEP parameters during the geometry optimization of the different hydrous structures (Table 1, main text).

SI 2: Chemical shifts of the anhydrate (CCDC 912147)

Figure S2 and **S3** show the predicted ^{13}C and ^{1}H chemical shifts of the anhydrate (Table 1, main text) after geometry optimization and following calculation of the chemical shifts in comparison to experimental data.
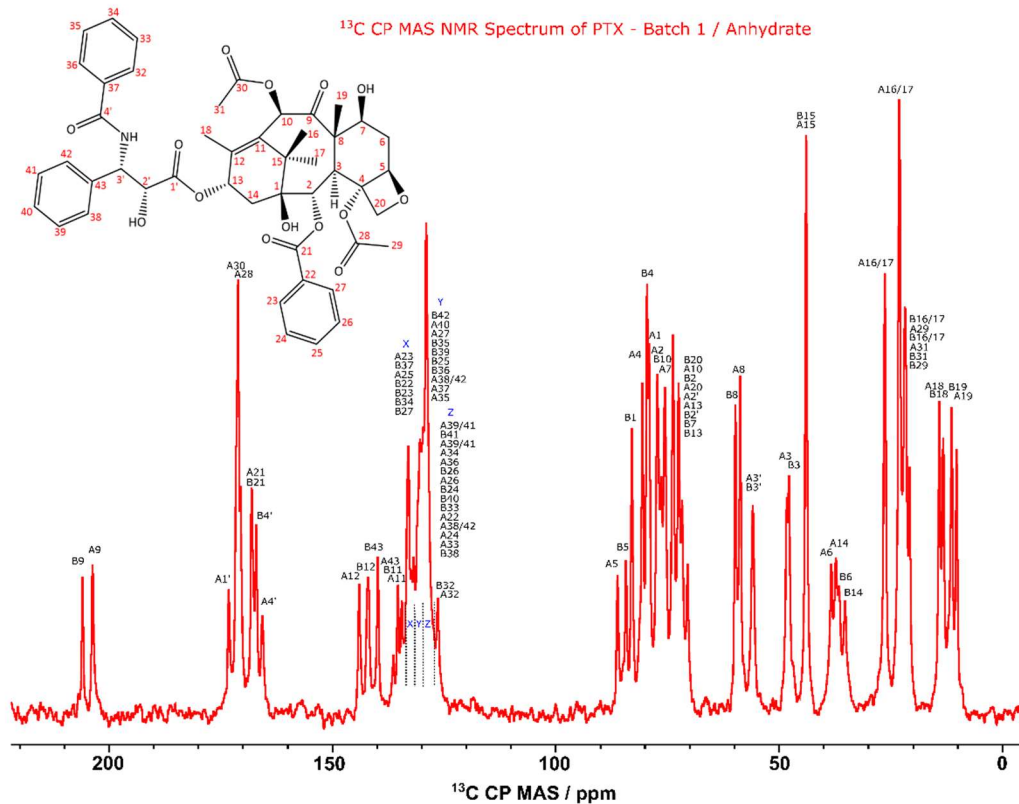

Figure S2: Tentative structural assignment of the experimental ^{13}C CP MAS spectrum of *PTX Batch 1* using the calculated chemical shifts of the anhydrate (Table 1). The calculated shifts were assigned based on the order of their chemical shift values.
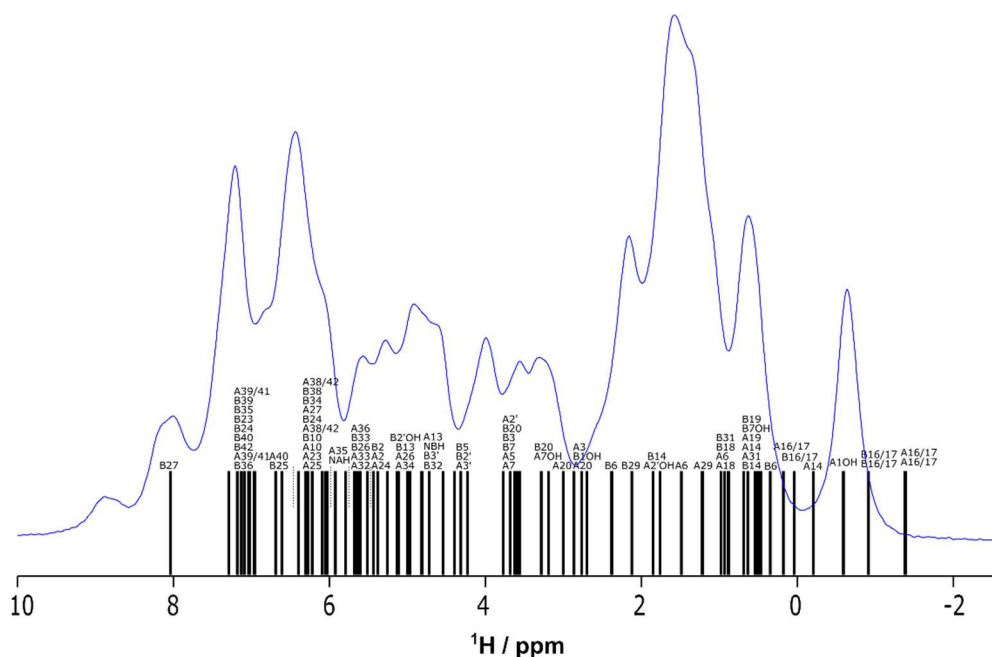
Figure S3: Comparison of the experimental ¹H one-pulse MAS spectrum of *PTX Dry* (recorded at 16.5 T and 100 kHz spinning frequency) with the calculated chemical shifts of the anhydrate (Table 1). The calculated shifts were assigned based on the order of their chemical shift values.

Figure S3 shows the ¹H one-pulse MAS spectrum of *PTX Dry*, recorded at 16.5 T and 100 kHz spinning frequency. Every black bar underneath the trace represents a calculated ¹H chemical shift of the asymmetric unit of the anhydrous structure (Table 1). Broader black bars are caused by the overlay of different bars which are close together in chemical shift. The letter above the bars describes the corresponding carbon or oxygen atom to which the distinct proton is bound. As soon as different letters are aligned above each other, they describe the region of different bars underneath them. The allocation is as follows: from top to bottom describes the distribution of the respective bars from high to low chemical shift values. This representation uses averaged CH$_3$ groups as a single value.

SI 3: Temperature calibration of the 3.2 mm MAS probe for 600 MHz

Temperature calibration was performed using a $Pb(NO_3)_2$ sample.[1] **Figure S4** shows the calibration for a spinning frequency of 24 kHz and varying temperatures. Different coloured dots correspond to different Bruker Cooling Unit (BCU2) power levels: strong (blue), medium (black) and low (grey). The vertical dashed lines show the set temperatures 0°C (purple) and 20°C (orange) whereas the horizontal dashed lines represent the calibrated 20°C (blue) and 37°C (body temperature, green). **Figure S5** shows the dependence of the recorded temperature on the spinning frequency for a controlled probe temperature of 296.4 K of the spectrometer. **Table S1** lists the Bruker Cooling Unit parameters for each set temperature. The VT gas channel of the 3.2 mm MAS probe is separate from the bearing and drive channels.
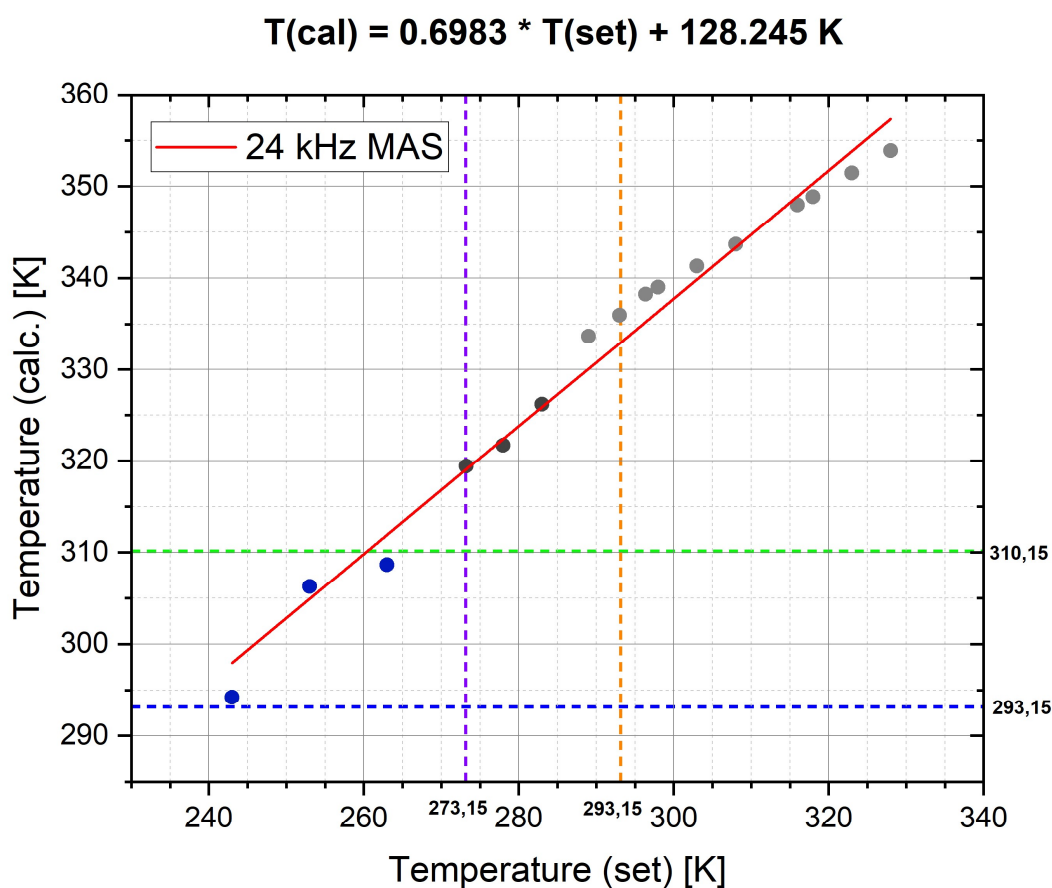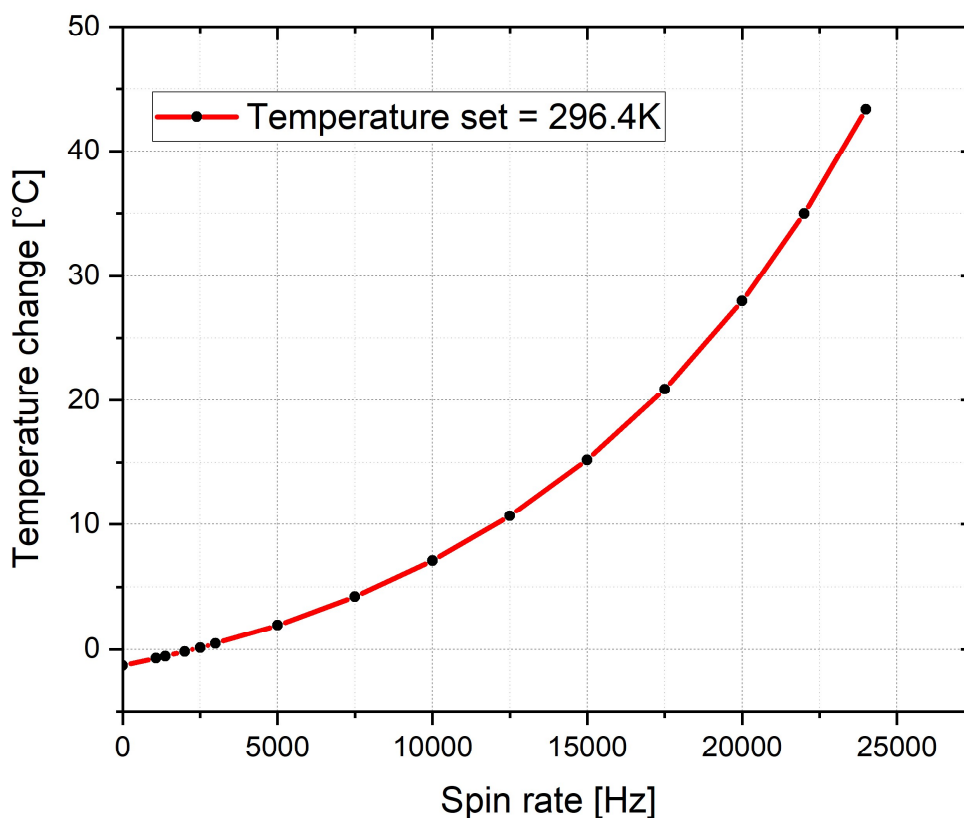
$$T(cal) = 0.6983 * T(set) + 128.245 \text{ K}$$

Figure S4: Resulting sample temperature calibration curve of the 3.2 mm double-channel (^{15}N-^{31}P/^{1}H-^{19}F) MAS probe (600 MHz) at a spinning frequency of 24 kHz, using a $Pb(NO_3)_2$ sample.

Figure S5: Resulting sample temperature calibration curve of the 3.2 mm double-channel ([15]N-^{31}P/[1]H-^{19}F) MAS probe (600 MHz) depending on the spinning frequency at a regulated probe temperature of 296.4 K, using a $Pb(NO_3)_2$ sample.

Table S1: Bruker cooling unit parameters for each set temperature.

Set temperature / Kelvin	Power level	Gas flow / litre per hour
243.0	strong	1000
253.0	strong	750
263.0	medium	1000
273.2	medium	1000
278.0	medium	750
289.0	low	500
293.0	low	500
303.0	low	500
308.0	low	500
313.0	low	500
316.0	low	500
318.0	low	500
328.0	low	500

SI 4: ^{13}C direct excitation MAS spectrum

An additional ^{13}C direct excitation MAS spectrum with a short interscan delay of 0.8 s was recorded (**Figure S6**). This measurement can give information about the relative mobilities of different parts of the structure. Regarding the structural assignment in **Figure S2** and **Table 3**, the most dominant signals of the ^{13}C direct excitation MAS spectrum belong to the methyl groups, followed by a smaller, but broader peak in the aromatic region. This indicates, on the one hand, a high mobility of those groups and, on the other hand, demonstrates the rigidity of the baccatin core, which was already shown by Harper *et al.*[2] and Heider *et al.*[3]. Heider *et al.* also suggested that the C3' phenyl ring is rigid whereas those at C4' and C2 are proposed to have dynamic disorder. The latter two phenyls ring are supposed to belong to the detected mobile aromatic part in the ^{13}C direct excitation MAS spectrum.
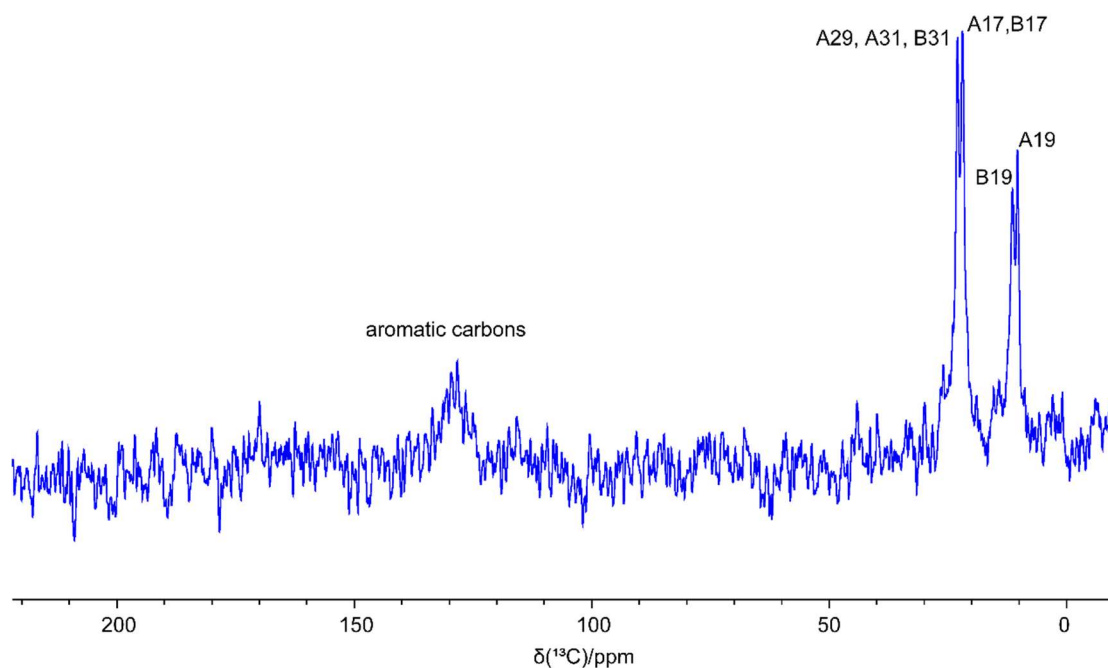

Figure S6: ^{13}C direct excitation MAS NMR spectrum of *PTX Batch 1* recorded at 14.1 T and 24 kHz MAS spinning rate, with a recycle delay of 0.8 s, and 512 co-added transients.
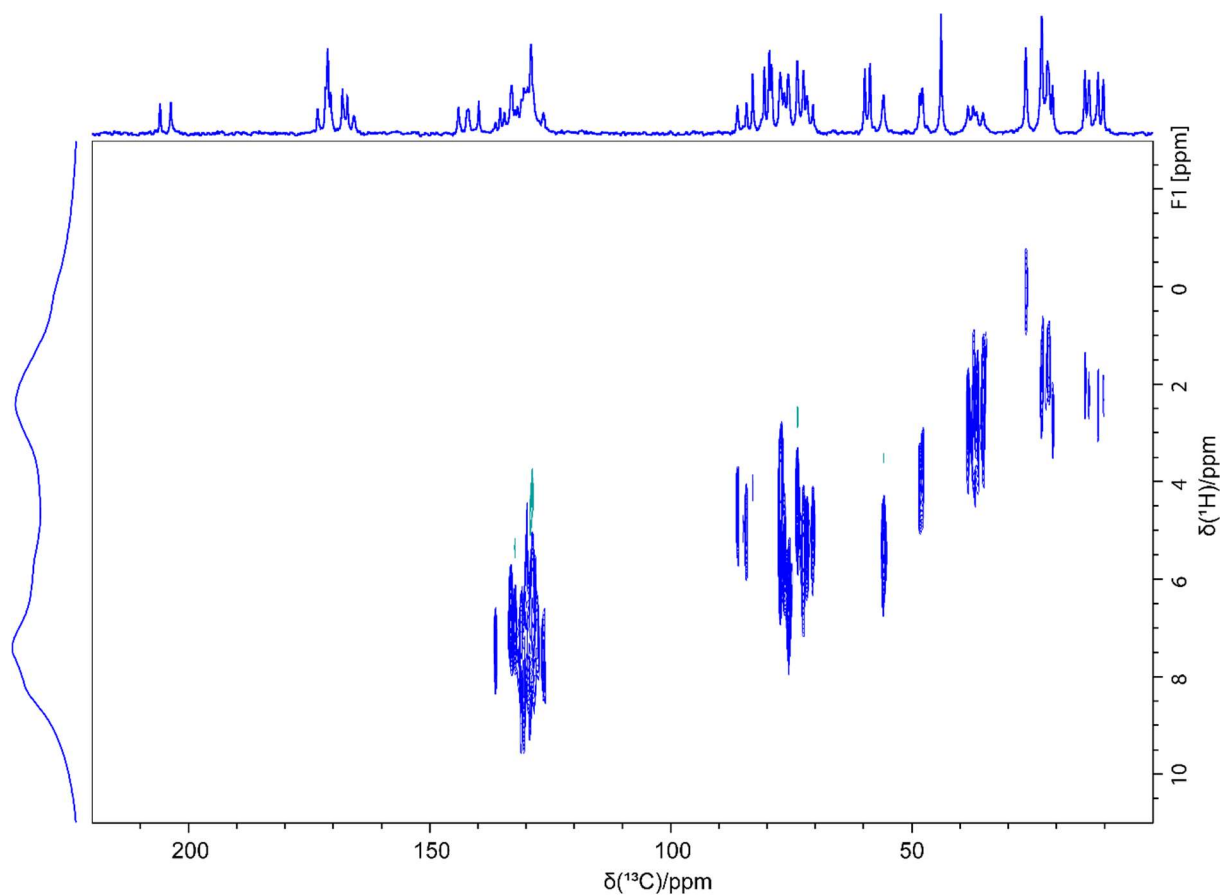
SI 5: ^{1}H-^{13}C FSLG HETCOR MAS spectrum of PTX Batch 1

Figure S7: ^{1}H-^{13}C HETCOR MAS spectrum of *PTX Batch 1*, recorded at 14.1 T and a MAS spinning rate of 20 kHz, using a mixing time of $\tau_{mix} = 50 \, \mu s$. 60 t_1 FID increments were acquired using a recycle delay of 2 s, each with 256 co-added transients. The corresponding ^{1}H one-pulse MAS and ^{13}C CP MAS NMR spectra are shown as external projections.
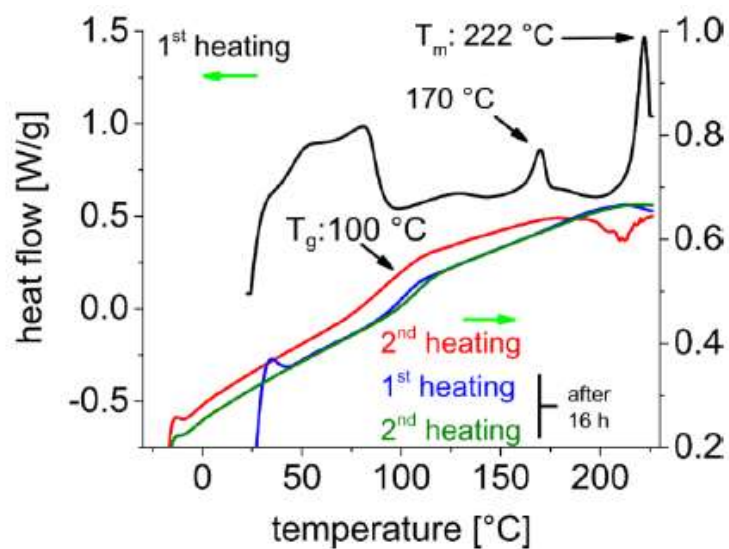
SI 6: DSC measurements of PTX Batch 1

Figure S8: DSC of 1st heating and cooling cycle of *PTX Batch 1*. Loss of crystal water results in the endotherm between 60 and 80°C. The endotherm at 170°C denotes a change in solid state structure. The sample melts at 222°C. The cooling curve does not show a change back to the original solid-state form*.*

SI 7: Elemental analysis of PTX Batch 2

Elemental Analysis measurement was involved for further investigation of the two phases in *PTX Batch 2*. The upper part of Table 2 contains the results of the elemental analysis, the bottom part shows the calculated percentages per element for the different hydrate forms of Table 1. As expected from the ^{13}C CP MAS evaluation, the experimental data doesn't fit a certain prediction of the hydrated structures. From the ^{13}C CP MAS spectrum, it can be estimated that 56% of *PTX Batch 2* exist in the anhydrous form and the remaining 44% in a hydrous form. Using this together with the experimental results of the elemental analysis, it turns out that the hydrous phase of *PTX Batch 2* contains 1.5 water molecules per molecule of PTX, resulting in an overall number of three water molecules per asymmetric unit of *PTX Batch 2*.

Table S2: Elemental Analysis of *PTX Batch 2* (top) and the analogous values for the structures in Table 1.

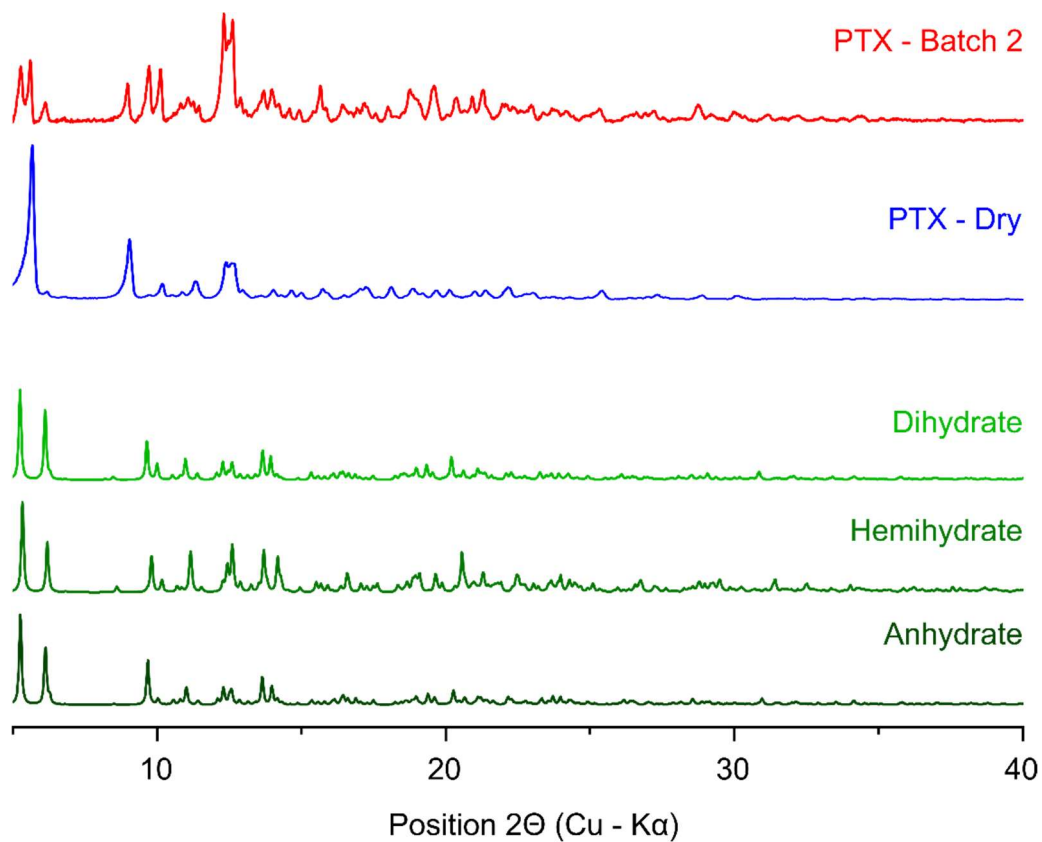|	Elemental Analysis		
PTX Batch 2	C [%]	H [%]	N [%]
	64.2	6.23	1.55
	Calculations		
	C [%]	H [%]	N [%]
Dihydrate	63.43	6.23	1.57
Hemihydrate	65.42	6.07	1.62
Anhydrate	66.11	6.02	1.64

SI 8: Complete PXRD data

Figure S9: Experimental PXRD data of *PTX Batch 2* and *PTX Dry* as well as simulated PXRD diffractograms of the published PTX structures summarized in Table 1 of the main manuscript.

SI 9: Preparation, NMR data, and PXRD data of amorphous PTX

Lyophilization was used to prepare amorphous PTX. PXRD measurements shown in **Figure S10** and solid-state NMR data in **Figure S11** confirmed the amorphicity.

PXRD spectrum of amorphous PTX

Position 2Θ (Cu - Kα)
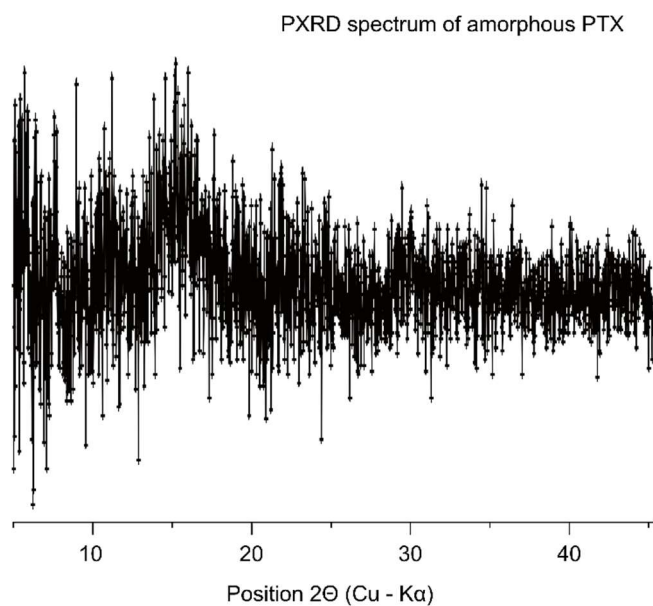
Figure S10: Diffraction pattern of amorphous PTX.

¹³C-CP MAS NMR spectrum of amorphous PTX
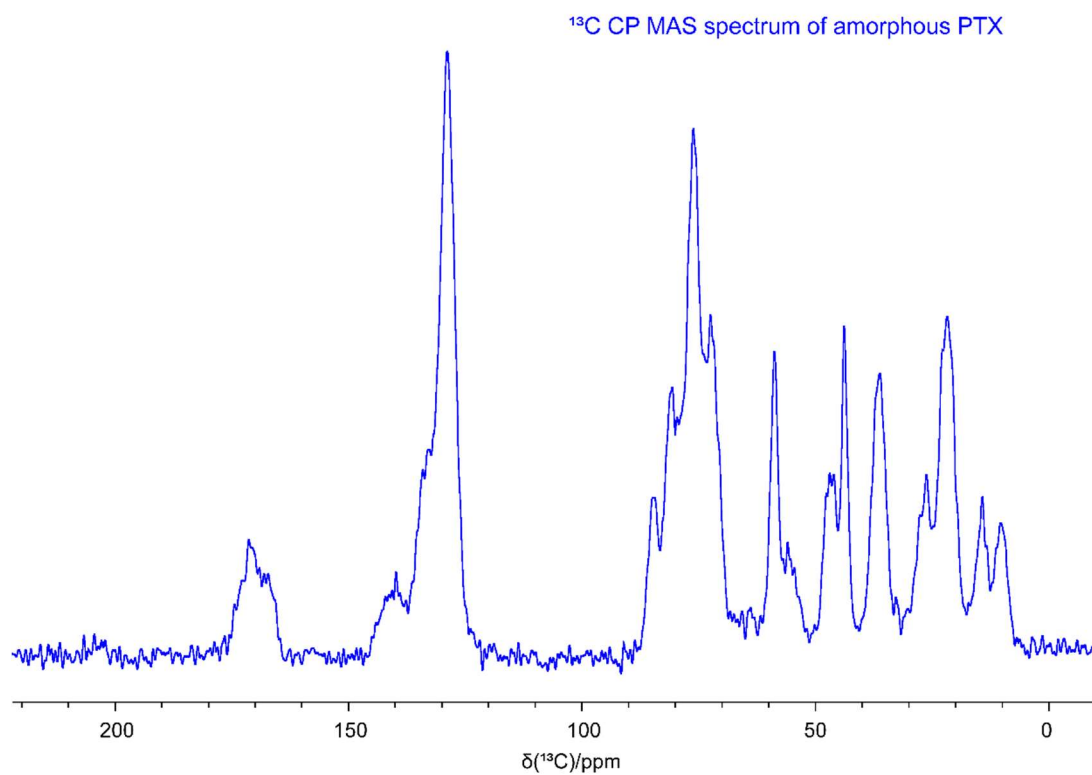
Figure S11: ¹³C CP MAS NMR spectrum of amorphous PTX, recorded at 14.1 T, 24 kHz MAS spinning rate, 2.5 ms contact time, 2.5 s recycle delay, and 23532 co-added transients. The line broadening is set to 30 Hz.

SI 10: Diffraction pattern of PTX Dry and an empty capillary
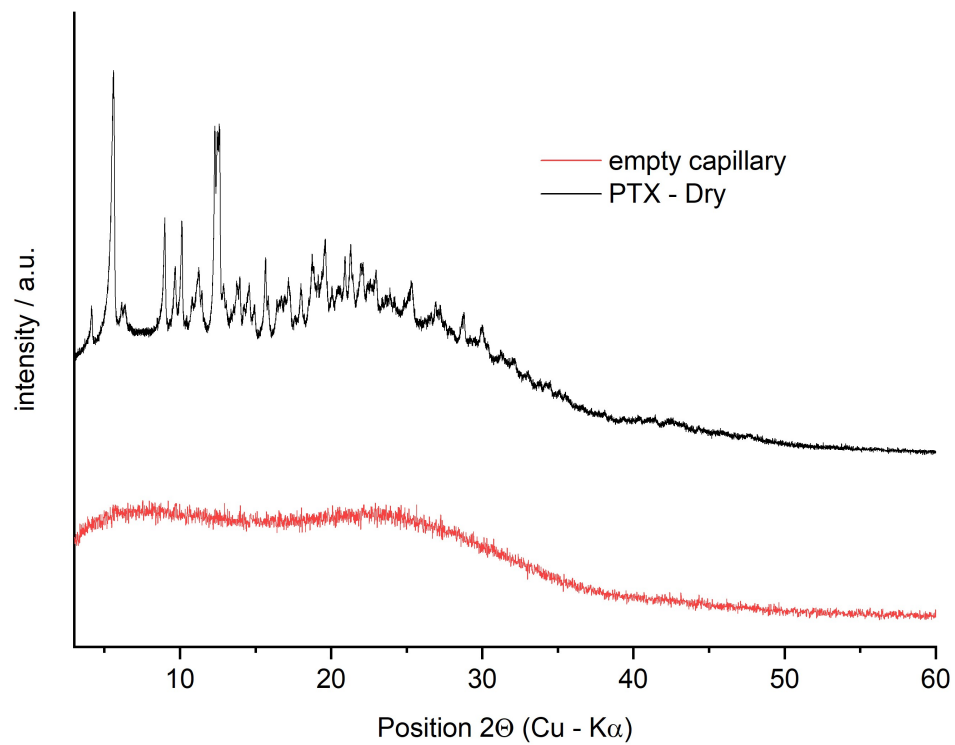
Figure S12: Diffraction pattern for *PTX Dry* (black) and an empty, crushed capillary.

SI 11: Preparation and NMR data of PTX Dry

In a first attempt, 32.9 mg PTX were placed in a welted glass with snap-on lid. Holes were made in the lid, the glass was placed in a Schlenk tube and evacuated overnight. The corresponding PXRD spectrum of this drying process is shown in **Figure S13**. The spectrum is shown without a subtracted background to emphasize the amorphous character, comparable to **Figure S10**.

PXRD pattern of PTX after drying overnight

Position 2Θ (Cu - Kα)
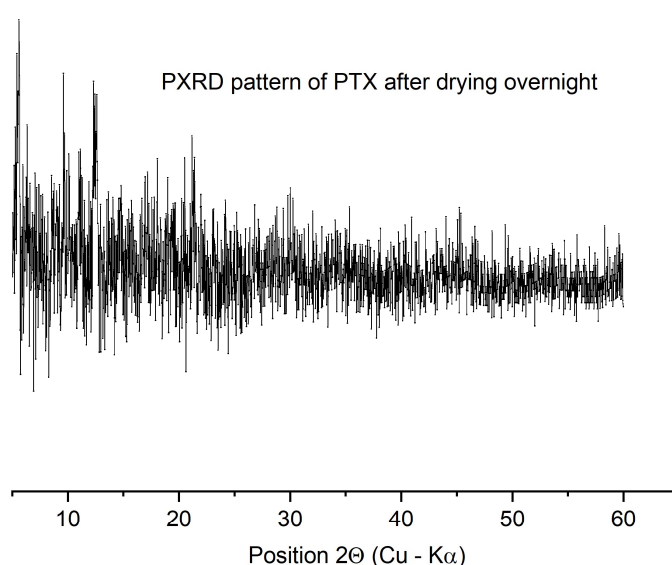
Figure S13: Diffraction pattern for dry PTX after drying overnight (black) with resulting amorphous character.

One reason for the amorphous character could be the rearrangement process from a hydrate phase to a dry phase. Therefore, in a second attempt to verify this assumption, 50 mg PTX were placed in a welted glass with snap-on lid with holes. This time, the sample was evacuated in a Schlenk tube for 10 days. Additionally, during the first three days, the Schlenk tube was placed in a 70°C oil bath. This sample was used for further investigation in the main text (**Figure 2b**).

^{1}H-^{13}C FSLG HETCOR MAS spectrum of PTX Dry
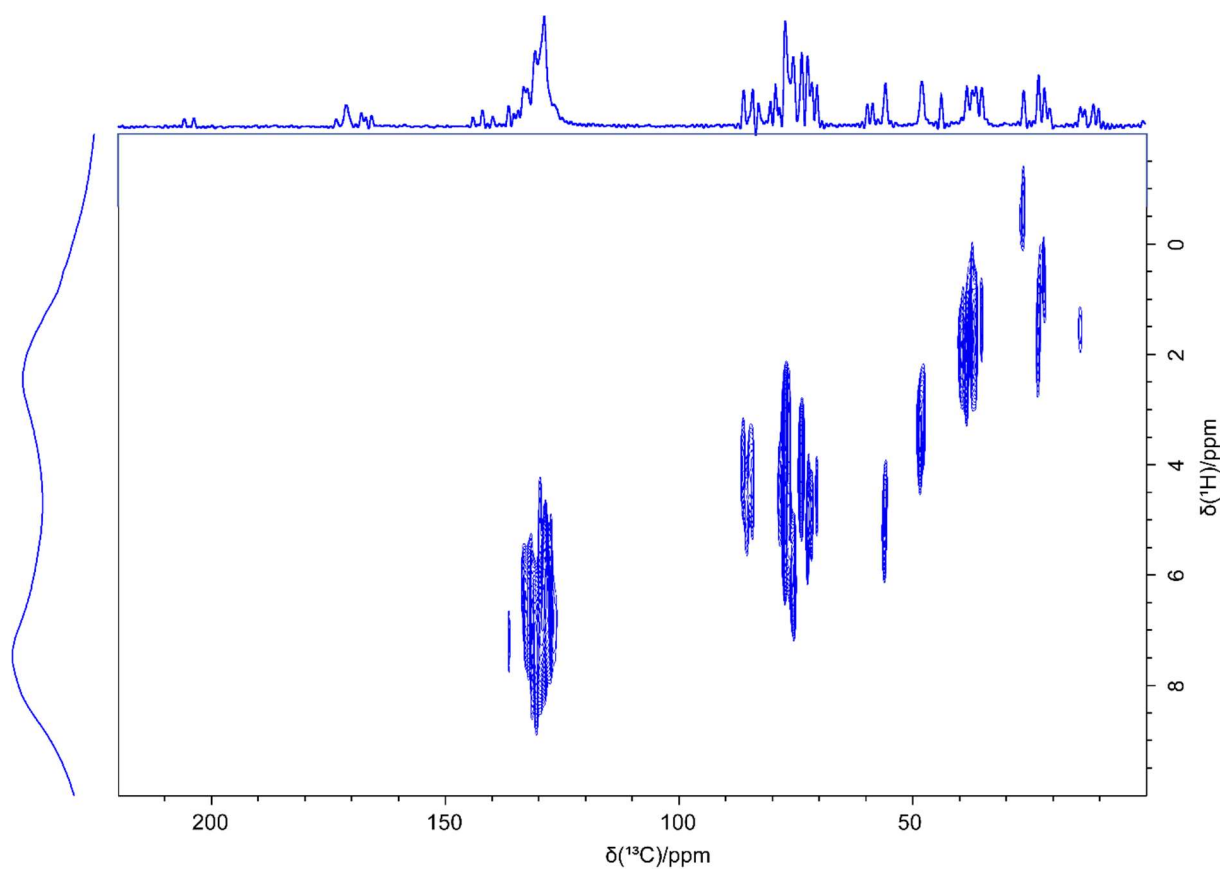
Figure S14: ^{1}H-^{13}C HETCOR MAS spectrum of *PTX Dry*, recorded at 14.1 T and a MAS spinning rate of 20 kHz, using a mixing time of $\tau_{mix} = 50\ \mu s$. 120 t_1 FID increments were acquired using a recycle delay of 4 s, each with 256 co-added transients. The corresponding ^{1}H one-pulse MAS and ^{13}C CP MAS NMR spectra are shown as external projections.

SI 12: References

[1]   a) A. Bielecki, D. P. Burum, *J. Magn. Reson., Ser. A* **1995**, *116*, 215-220; b) V. Hronský, *Acta Electrotechnica et Informatica* **2013**, *13*.

[2]   J. K. Harper, D. H. Barich, E. M. Heider, D. M. Grant, *Cryst. Growth Des.* **2005**, *5*, 1737-1742.

[3]   E. M. Heider, J. K. Harper, D. M. Grant, *Phys. Chem. Chem. Phys.* **2007**, *9*, 6083-6097.

Journal of Materials Chemistry B

Materials for biology and medicine

rsc.li/materials-b

POL-4-PTX

Polymer

Taxol

1D - MAS MNR

14N   15N

Themed issue: Emerging Investigators 2020

ROYAL SOCIETY OF CHEMISTRY

PAPER
Ann-Christin Pöppler *et al.*
14N–1H HMQC solid-state NMR as a powerful tool to study amorphous formulations – an exemplary study of paclitaxel loaded polymer micelles

Indexed in Medline!

Journal of Materials Chemistry B

PAPER

Check for updates

14N–1H HMQC solid-state NMR as a powerful tool to study amorphous formulations – an exemplary study of paclitaxel loaded polymer micelles†

Marvin Grüne,[a] Robert Luxenhofer, [ID][b] Dinu Iuga,[c] Steven P. Brown [ID][c] and Ann-Christin Pöppler [ID] *[a]

Amorphous drug–polymer formulations are complex materials and often challenging to characterize, even more so if the small molecule component itself is increasingly complex. In this work, we present 14N–1H HMQC magic-angle spinning (MAS) NMR experiments in the solid state as a promising tool to study amorphous formulations. Poly(2-oxazoline) based polymer micelles loaded with different amounts of the cancer drug paclitaxel serve to highlight the possibilities offered by these experiments: while the dense core of these polymeric micelles prevents NMR spectroscopic analysis in solution and the very similar 15N chemical shifts hamper a solid-state NMR characterization based on this nucleus, 14N is a very versatile alternative. 14N–1H HMQC experiments yield well-separated signals, which are spread over a large ppm range, and provide information on the symmetry of the nitrogen environment and probe 14N–1H through-space proximities. In this way, the overall complexity can be narrowed down to specific N-containing environments. The results from the experiments presented here represent a valuable puzzle piece, which helps to improve the structural understanding of drug–polymer formulations. It can be straightforwardly combined with complementary NMR spectroscopic experiments and other analytical techniques.

Introduction

Paclitaxel (PTX, Scheme 1) is an effective anti-cancer drug for a wide range of tumours, but it exhibits a very low aqueous solubility of 0.4 μg mL^{-1}.[1,2] Therefore, a variety of different formulations for PTX has been developed.[3] This includes the protein-based nanoparticle Abraxane®, the polymer-conjugate Opaxio™, Genexol-PM® and NK105.[4,5] The latter two contain PTX in polymer micelles formed of polyethylene glycol–polylactic acid (Genexol-PM®) and polyethylene glycol–poly(amino acid) (NK105) copolymers. In general, the development of formulations and their clinical trials require very long times with highly uncertain outcomes. The above mentioned formulations have undergone multiple phase II/III clinical trials over the past decades, *e.g.* a recently published phase III clinical trial of NK105,[6] and only Abraxane® has been successfully marketed with FDA approval since 2007. Furthermore, they are all

characterized by a relatively low PTX loading not exceeding 25 wt%. In this context, Luxenhofer *et al.* reported promising preclinical data for polymer micelles comprising a poly(2-oxazoline) (POx) based triblock copolymer loaded with up to 50 wt% of PTX.[7,8] Compared to the clinically approved PTX
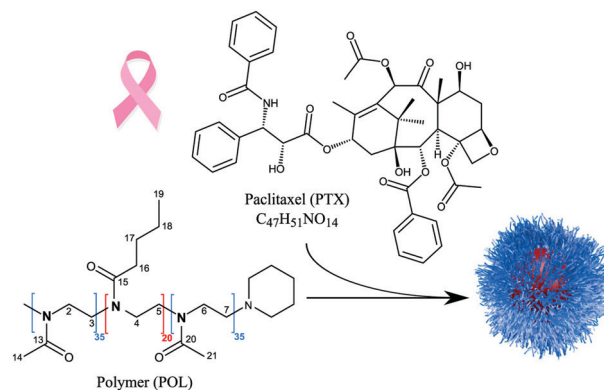
Scheme 1 Structural formula of the components used in this study: the amphiphilic block copolymer poly(2-methyl-2-oxazoline)-*block*-poly(2-*n*-butyl-2-oxazoline)-*block*-poly(2-methyl-2-oxazoline) (POL) encapsulates paclitaxel (PTX) by self-assembly into polymeric micelles (schematic drawing on the right).

[a] *Institute of Organic Chemistry, University of Würzburg, Am Hubland, 97074 Würzburg, Germany. E-mail: ann-christin.poeppler@uni-wuerzburg.de*
[b] *Lehrstuhl für Chemische Technologie der Materialsynthese, University of Würzburg, Röntgenring 11, 97070 Würzburg, Germany*
[c] *Department of Physics, University of Warwick, Coventry, CV4 7AL, UK*
† Electronic supplementary information (ESI) available. See DOI: 10.1039/d0tb00614a

This journal is © The Royal Society of Chemistry 2020

J. Mater. Chem. B, 2020, **8**, 6827–6836 | **6827**

formulations, their formulations showed higher maximum tolerated doses, elevated drug exposure to tumour tissues and prolonged survival of mice bearing A2780 human ovarian tumours. Schulz et al.,[9] Jaksch et al.[10] and Sochor et al.[11] studied their micellar morphology for different drug loadings (PTX and curcumin) using dynamic light scattering, atomic force microscopy, (cryogenic) transmission electron microscopy, and small-angle neutron scattering (SANS). They found that the pure polymer self-assembles into wormlike and spherical micelles in aqueous solution, while the incorporation of PTX led to the exclusive formation of spherical particles. Interestingly, SANS data revealed small, PTX rich domains partly submerged within the micellar core. Apart from such morphological aspects and capability to design improved drug delivery systems, it is very important to also understand the complex structural arrangements in such amorphous drug–polymer formulations on the molecular level. NMR probes the local environment of molecules and is thus an excellent tool to report on various possible interactions. This doesn't necessarily require crystalline or well-ordered structures, and also gives excellent results for disordered as well as amorphous samples.[12–14]

In particular, solid-state NMR has been established as a powerful tool for structure elucidation in pharmaceutical contexts such as identification of polymorphs or investigation of amorphous solid dispersions.[15–17] The sometimes strongly reduced mobility of encapsulated drugs within drug formulations can hinder the characterization by NMR in solution due to strong broadening of the signals, which makes solid-state NMR the corresponding method of choice. Callari et al. as well as Pöppler et al. recently showcased how solid-state NMR at moderate to fast Magic Angle Spinning (MAS) helps to obtain loading dependent structural insights into micellar formulations with an assumed core–shell structure.[18,19] Both groups found that increasing the loading of two different types of polymeric micelles did not just affect the micellar core but interestingly also affected the surrounding shell, which served as a basis to explain their physicochemical and biological properties such as reduced cellular uptake and inferior dissolution rates. Hirsh et al. have recently also shown how ^{1}H MAS measurements enable the rapid characterization of general pharmaceutical dosage forms.[20] The enormous progress made with respect to hardware development, e.g. MAS frequencies of up to 130 kHz being available now,[21] also enables high-resolution detection of protons in the solid state with longer coherence lifetimes.[22–24] The latter are essential prerequisites for sophisticated homonuclear as well as heteronuclear 2D experiments, which are exciting tools to learn more about the intermolecular proximities in a large range of materials.

However, for the solid-state NMR spectroscopic characterization of PTX and its formulations as discussed above, a series of complexities arises: PTX alone with its 51 protons and thus a variety of strongly overlapping chemical environments already poses a challenge. In addition, crystalline PTX contains two individual molecules in the asymmetric unit ($Z' = 2$),[25] which leads to the doubling of the expected resonances. Consequentially, to date, only ^{13}C solid-state NMR data with assignment based on

comparison with structurally related fragments and calculations has been published,[26,27] while ^{1}H solid-state NMR data of PTX is still missing. Taking the polymer component and potential drug–polymer interactions into account further complicates the spectral evaluation and thus requires narrowing down the search space, e.g. by focusing on specific functionalities. For example, spectral simplification can be achieved by making use of NMR active heteronuclei.

The frequent involvement of nitrogen atoms in hydrogen bonding in pharmaceuticals makes this nucleus a promising starting point for a detailed investigation of PTX containing formulations through 2D nitrogen-proton correlation experiments, especially since PTX has only one nitrogen environment per molecule. There are two NMR-active nitrogen isotopes with low magnetogyric ratios: [15]N ($I = 1/2$) possesses a low natural abundance of only 0.37%, whereas ^{14}N has a natural abundance of 99.6% but exhibits quadrupole broadening due to its nuclear spin quantum number $I = 1$. The substantial disadvantage of the first-order quadrupole interaction, causing a broadening in the range of several MHz, can be avoided by setting the indirect ^{14}N spectral width of the 2D correlation equal to the spinning frequency. Tatton et al. successfully applied this in the form of a [14]N–[1]H heteronuclear multiple-quantum correlation (HMQC) experiment to study crystalline model compounds,[28] hydrogen bonding in co-crystals and attempting the first transfer to amorphous solid dispersions.[29] So far, the majority of [14]N–[1]H HMQC experiments have been performed for highly ordered, crystalline compounds.[28,30–39] In contrast, disordered systems with significant differential dynamics are more challenging systems and there are thus very seldom reports on employing the [14]N–[1]H HMQC experiment for their characterization. However, the characterization of disordered and amorphous materials could substantially benefit from the additional ^{14}N second-order isotropic quadrupolar shifts (see the ESI† for detailed equations) as opposed to the ^{15}N isotropic chemical shifts alone. The additional ^{14}N second-order isotropic quadrupolar shifts will result in the spreading of the nitrogen signals over a larger ppm range (hundreds of ppm) and can thus disperse very similar or even overlapping ^{15}N NMR signals. This could prove to be crucial for the analysis of amorphous drug formulations, either when the nitrogen in both, the drug and polymer, is a part of the same functional moiety (e.g. amides in the previously mentioned POx/PTX formulations) or when the distribution of similar local environments as observed in amorphous forms makes the differentiation between peaks challenging. This is underlined by the fact that around 84% of unique small-molecule drugs contain a nitrogen atom.[40] As a result, there is a large, yet largely unexplored potential of this experiment for the analysis and increased understanding of such materials. In solid-state NMR, there are two different ways to create [14]N–[1]H HMQCs, either heteronuclear through-bond [14]N–[1]H J-couplings and residual second-order quadrupole–dipolar couplings or by [14]N–[1]H through-space dipolar couplings.[33,34,41] By varying the recoupling time in the latter case, it is then possible to obtain different through-space proximities with longer recoupling times probing longer range intra- and intermolecular

6828 | J. Mater. Chem. B, 2020, **8**, 6827–6836

This journal is © The Royal Society of Chemistry 2020

N···H distances.[28] A practical guideline with a focus on experimental procedures and parameters can be found in the recent literature.[42] Combining all aspects, $^{14}N-^1H$ HMQC experiments represent a very promising tool for the investigation of the complex drug–polymer assemblies.

In the present work, we investigate the suitability and potential of $^{14}N-^1H$ solid-state NMR experiments for the analysis of amorphous polymer–PTX formulations, for which structural information is challenging to obtain due to the lack of long-range order. Therefore, differently loaded paclitaxel formulations based on the amphiphilic triblock copolymer poly(2-methyl-2-oxazoline)-*block*-poly(2-*n*-butyl-2-oxazoline)-*block*-poly(2-methyl-2-oxazoline) (pMeOx-*b*-pBuOx-*b*-pMeOx = A-pBuOx-A = POL) (Scheme 1) serve as the set of samples.[8] Complemented by samples of the individual components, the following points will be addressed: (i) general feasibility of the experimental setup for the individual components, (ii) exploring the potential of $^{14}N-^1H$ HMQC experiments for the analysis of their amorphous micellar formulations, (iii) extracting information about $^{14}N-^1H$ proximities for intermolecular through-space contacts and (iv) their interpretation with respect to (loading dependent) structural features as a complementary source of information to existing data obtained by techniques such as SANS.

Experimental section

Materials

Paclitaxel in its crystalline form was purchased from LC Laboratories and used without further purification. The ABA triblock polymer poly(2-methyl-2-oxazoline)-*block*-poly(2-*n*-butyl-2-oxazoline)-*block*-poly(2-methyl-2-oxazoline) (POL) was synthesized according to previously published protocols.[43] Subsequent preparation of the differently loaded PTX–POL formulations also followed the literature known procedures.[8,9] A short description can be found in the ESI.† Resulting drug loadings were determined using HPLC analysis. The corresponding micellar formulation denoted as POL-2-PTX, POL-4-PTX and POL-9-PTX contain 17 wt% (10:2), 29 wt% (10:4) and 47 wt% (10:9) PTX.

NMR

$^{14}N-^1H$ HMQC experiments were performed using a Bruker Avance III spectrometer at a ^1H Larmor frequency of 850 MHz. A Bruker 1.3 mm triple resonance probe operating in the double resonance mode at a MAS frequency of 60 kHz was used. A pulse sequence diagram is shown in Fig. S1 (ESI†). Heteronuclear dipolar couplings were reintroduced by applying rotary resonance recoupling (R^3)[44] under the $n = 2$ condition, as proposed by Gan *et al.*,[33] using $x, -x$ phase inversion.[45] Each recoupling block had a length of 16.67 μs. The durations of the ^1H pulses/^{14}N pulses were 1.6 μs/3.2 μs for PTX and POL-9-PTX, 1.55 μs/3.1 μs for POL-2-PTX, POL-4-PTX, and 1.55 μs/3.2 μs for POL. A four-step nested phase cycle was used to select changes in the coherence order $\Delta p = \pm 1$ (on the first ^1H pulse, two steps) and $\Delta p = \pm 1$ (on the final ^{14}N pulse, two steps). Correct calibration of the magic angle is crucial for this experiment.

All NMR data including the compiled pulse sequences for the results presented in this paper can be found in the Warwick Research Archive Portal (WRAP). Magic angle and pulse calibrations were performed with the dipeptide β-AspAla. ^{14}N chemical shifts were referenced to saturated NH_4Cl at -352.9 ppm, corresponding to a primary reference of CH_3NO_2 at 0 ppm. ^{15}N experiments recorded at 9.4 T were referenced to unlabelled α-glycine at -342.0 ppm and those at 20 T were referenced to labelled L-histidine, which has an NH_3^+ resonance at -333.1 ppm. Both ways of ^{15}N referencing correspond to a CH_3NO_2 reference at 0 ppm. The ^{13}C NMR data were measured with a Bruker Avance III HD 600 MHz spectrometer and a 3.2 mm double-channel probe. The duration of the ^1H pulses was 2.5 μs in the ^{13}C CP MAS under ramped cross-polarization conditions optimized using a ramp from 90 to 100 with 100 increments and the α-glycine sample. SPINAL-64[46] heteronuclear decoupling was applied during an acquisition period of 23 ms at a ^1H rf nutation frequency of 100 kHz, with an optimized pulse length of 4.9–5.1 μs. The ^{15}N data of POL-9-PTX were recorded with a Bruker Avance III spectrometer at a ^1H Larmor frequency of 850 MHz and a duration of the ^1H pulses of 2.5 μs under the optimized cross-polarization conditions using histidine. The ^{15}N data of crystalline PTX and POL were recorded using a Bruker Avance Neo 400 MHz spectrometer. In both cases, 4 mm rotors with a sample volume of 80 μL were used. The duration of the ^1H pulses was 2.5 μs under the optimized cross-polarization conditions using α-glycine. KBr was used for magic angle calibration. ^{13}C chemical shifts were referenced to the methylene carbon of adamantane at 38.48 ppm.[47]

Results

As the starting point for the spectral assignment and further investigation of the three differently loaded formulations of the poorly water-soluble cancer-drug paclitaxel containing 17 wt% (POL-2-PTX), 29 wt% (POL-4-PTX) and 47 wt% (POL-9-PTX) PTX, NMR experiments in solution were performed (Sections SI 4–SI 6, ESI†). For the assignment of PTX, data from NMR measurements in $CDCl_3$ were used. However, in aqueous polymer micellar formulations, only extremely broad, unresolved PTX signals can be observed in the ^1H NMR spectra (Section SI 6 with Fig. S4, ESI†), underlining the necessity to focus on solid-state NMR for the analysis of such formulations. Consequently, a set of different solid-state NMR spectra at moderate to fast MAS spinning frequencies were recorded for the formulations and as-received PTX, amorphous PTX and the neat polymer.

Both the ^{13}C CP MAS NMR spectra recorded at 24 kHz (Fig. 1a) as well as powder X-ray diffraction data (Fig. S5, ESI†) confirm that the formulations are amorphous materials in agreement with a single glass transition temperature published in a previous work by one of the authors.[9] While crystalline paclitaxel (black spectrum) shows two sets of carbon resonances due to its two independent molecules in the asymmetric unit, amorphous PTX and an exemplary formulation (POL-9-PTX, highest PTX content) (grey and blue spectrum) show broad
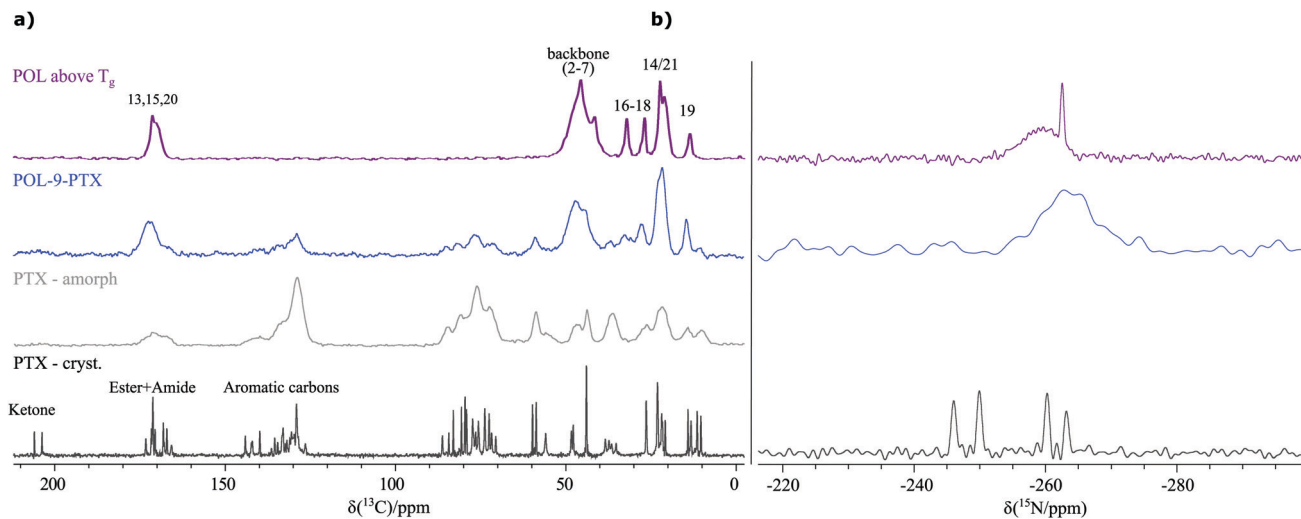
Fig. 1 (a) ^{13}C CP MAS NMR spectra of the pure polymer (purple), an exemplary PTX formulation (blue), amorphous (grey) and crystalline PTX (black). Partial peak assignment is indicated. All spectra were recorded at 14.1 T and 24 kHz MAS with a contact time of 2.5 ms and the following parameters (co-added transients/recycle delay): 1756/2.5 s (purple), 2048/2.0 s (blue), 23 532/2.5 s (grey) and 1756/2.5s (black). (b) Corresponding ^{15}N CP MAS NMR spectra recorded at 9.4 T (PTX, POL) and 20 T (POL-9-PTX) using a contact time of 1 ms for POL and 2 ms for PTX. 82 796 (PTX), 16 991 (POL) and 25 600 (POL-9-PTX) co-added transients were measured with a recycle delay of 5.0 s (PTX, POL) and 3.0 s (POL-9-PTX) resulting in an overall experimental time of 4 d 19 h, 24 h and 21 h, respectively. Please note that the ^{15}N NMR spectrum of crystalline PTX is the only dataset, which was recorded on a new batch of PTX containing two differently hydrated PTX phases and thus showing an additional set of signals. As PTX exists in its amorphous state in the formulations and is dissolved for preparation, the initial degree of incorporated water in the respective phase is not relevant for the analysis of the formulations.

signals as expected for materials lacking long-range order and containing a distribution of environments and thus chemical shifts. Consequently, several moieties of PTX appear as joint signals complicating a straightforward extraction of spectral changes upon incorporation into the micelles in a similar way as recently shown for related polymer micelles loaded with curcumin as the model compound.[19] Moreover, additional complications arise from the overlap between PTX and POL resonances as can be seen from a comparison with the ^{13}C CP MAS spectrum of the neat polymer (purple spectrum). Note, that for better comparability, the neat polymer was heated above its glass transition temperature T_g (T_g(POL) = 56 °C)[48] prior to the measurement to account for similar conditions during the preparation of the formulations. Consequently, the analysis of the carbon spectra and extraction of reliable structural information is difficult and requires complementary tools such as quantum chemical calculations, which will be explored in detail in a separate work.

Ideally, for a thorough characterization of the formulations we would like to use the direct information from ^{1}H NMR data at fast MAS due to the high sensitivity of the ^{1}H nucleus to intermolecular interactions, through space proximities and subtle changes in the packing arrangement. The ^{1}H MAS NMR spectra recorded at 60 kHz are shown as external projection in the corresponding ^{14}N–^{1}H HMQC spectra in Fig. 2 and 3. As can be seen, the spectra are dominated by severe signal overlaps despite being recorded in a high magnetic field (20 T). Consequently, spectral simplification is required and the presence of only one secondary amide moiety per PTX enables this through N–H correlation experiments. Additionally, the tertiary amide functional groups in the polymer

could also serve as another source of structural information. Therefore, ^{15}N CP MAS spectra were recorded and it is very interesting to note that the secondary amides from PTX (Z' = 2, crystal structure in SI 10, ESI†) and the tertiary amide of the polymer show resonance in the same spectral region (Fig. 1b). For the POL-9-PTX formulation, only a very broad resonance can be observed, again in a similar spectral region and thus showing the need for a dispersion of the signals as expected for the quadrupolar ^{14}N nucleus.

^{14}N–^{1}H HMQC MAS NMR experiments are particularly powerful in this context, require only a small amount of sample and have been applied to study a variety of crystalline compounds.[33,35] Therefore, in the first step, ^{14}N–^{1}H HMQC spectra of the pure compound were recorded to identify their nitrogen shifts and ensure sufficient separation of the PTX and polymer nitrogen environments.

Pure compounds

Fig. 2 shows ^{14}N–^{1}H HMQC spectra of crystalline PTX as well as of the pure polymer. For PTX, correlations with two different dipolar recoupling times were measured and are illustrated in black (133.3 μs) and green (400.0 μs). Similar recoupling times in the ^{14}N–^{1}H HMQC experiments were first tested for the dipeptide β-AspAla showing the expected appearance of longer range through space proximities upon increase of the recoupling time (see Fig. S6 (ESI†) and Tatton *et al.*[28]). For PTX, using short recoupling times and in agreement with the X-ray diffraction data, two cross peaks at 8.8/−30 ppm (N^A) and 8.0/−18 ppm (N^B) were observed for the NH groups of the two individual molecules of PTX in the asymmetric unit. Consequently, one can deduce
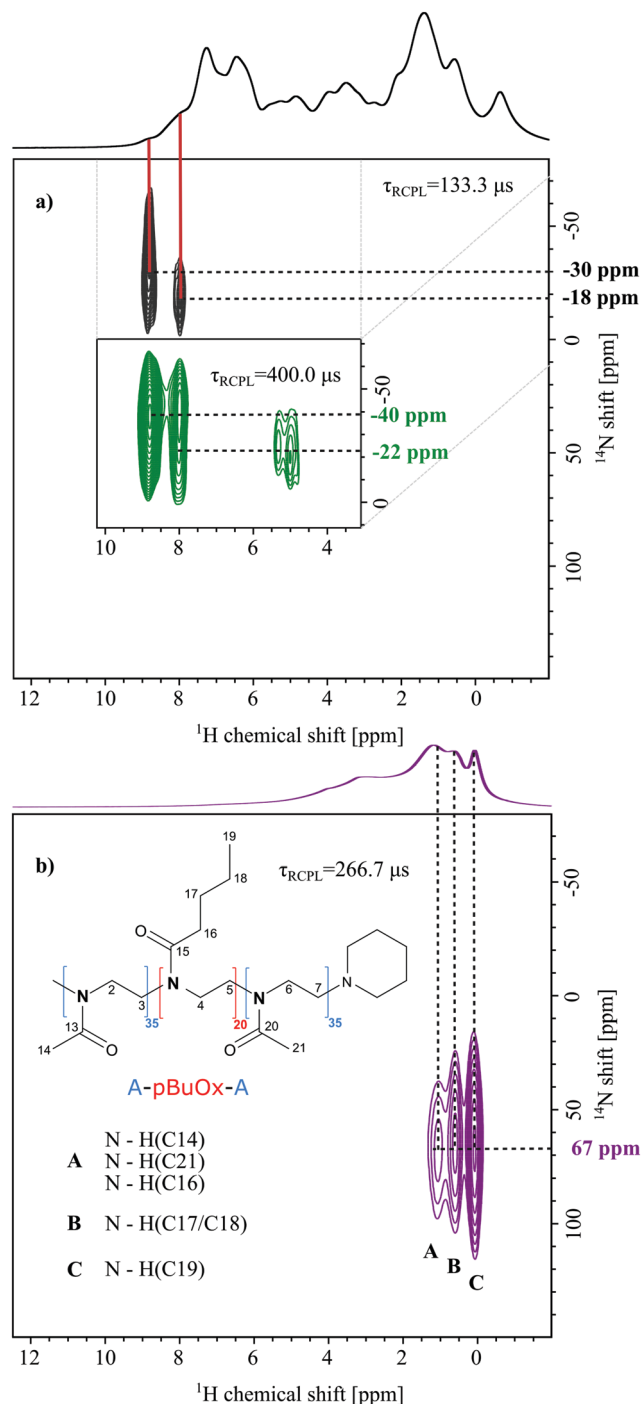
6830 | *J. Mater. Chem. B*, 2020, **8**, 6827–6836

This journal is © The Royal Society of Chemistry 2020

Fig. 2 (a) $^{14}N–^1H$ HMQC spectra (20 T, 60 kHz) of crystalline PTX recorded with recoupling times of $\tau_{RCPL} = 133.3$ μs, acquired with 34 t_1 FIDs (black) and $\tau_{RCPL} = 400.0$ μs, acquired with 98 t_1 FIDs (green, as an inset), each with 128 co-added transients for a recycle delay of 1.5 s (experimental time: 1 h 50 min (black) and 5 h 18 min (green)). The base contour level is at 30% (black), 34% (green) and 22% of the maximum peak height. The red bars point out the corresponding peaks in the ^1D ^1H one-pulse MAS NMR spectrum. (b) The $^{14}N–^1H$ HMQC spectrum of POL recorded with a recoupling time $\tau_{RCPL} = 266.7$ μs, 16 t_1 FIDs, each with 2048 co-added transients for a recycle delay of 1.3 s (experimental time 1 h 30 min), and corresponding assignment of the N···H cross-peaks. The skyline projections correspond to ^1H one-pulse MAS NMR spectra of each sample.

that N^A is involved in stronger hydrogen bonding than N^B. This agrees with a longer direct N^A···H distance, *e.g.* stronger involvement in hydrogen bonding, as observed in the crystal structure reported by Vella-Zarb *et al* for PTX anhydrate (Table 1, CSD code: RIGLEA).[25]

With a three times higher recoupling time, two changes of the previous peaks for shorter recoupling time are noticeable: the intensity of the peak corresponding to nitrogen N^B increases compared to N^A, the peak seems elongated in the ^{14}N dimension and two additional signals at around 5 ppm of proton chemical shift are observed. Small changes in the ^{14}N shift (N^A: -30 to -40 ppm and N^B: -18 to -22 ppm) could be caused by a temperature increase in the sample caused by the longer irradiation through the recoupling blocks. As the recoupling time for the dipolar couplings increases, it is possible to sample longer N···H distances through space. Consequently, the relative signal increase of N^B can be explained by proximities of N^A and N^B to aromatic protons, whose chemical shifts are overlapping with those of the proton attached to N^B in agreement with an increased ^1H intensity at 8.0 ppm. To confirm this, intra- and intermolecular close ^{14}N···^1H distances of up to 3 Å were extracted from PTX crystallographic data (Table 1, CSD code: RIGLEA). The threshold was chosen based on the maximum distances previously observed for comparable recoupling times.[28] Indeed, the shortest contact for N1 is found for the *ortho*-CH of the adjacent aromatic ring denoted as carbon 32 in the ESI.† In turn, the shortest NH distances for the second molecule were observed for the adjacent aliphatic CH and OH units (C3′H and C2′OH), which could explain the cross peaks observed at 5.0 and 5.3 ppm in the ^1H dimension. However, the distances in Table 1 can only serve as indication and should be viewed carefully as these distances originate from PXRD data at high temperature (360 K). Furthermore, it is still not fully understood why, for some small molecule compounds, fewer contacts than expected are observed.[42] In the $^{14}N–^1H$ HMQC MAS NMR spectrum of the neat polymer (Fig. 2b) recorded at an intermediate recoupling time of 266.7 μs (no direct NH), three cross peaks at a ^{14}N shift of 67 ppm and distinct ^1H chemical shifts are observed. Peak A results from the through space proximity of the nitrogen with the methyl groups C14 and C21 as well as the methylene group C16. Peak B indicates proximity to the CH2 unit of the hydrophobic butyl sidechain (C17/18) and peak C is related to N···H proximities including the methyl protons of the butyl sidechain (C19). Please note, that due to micelle formation, these cross-peaks are most likely of intermolecular nature. Interestingly, no cross peaks between N and polymer backbone CH2 groups could be observed. For a more detailed discussion on the signal assignment and appearance of specific cross-peaks, the reader is referred to the SI 4 (ESI†). Overall, the comparison of the two individual components shows that their nitrogen environments can be clearly distinguished in the $^{14}N–^1H$ HMQC experiment, which is not the case if ^{15}N chemical shifts are observed (see Fig. 2b and Table 1). Additionally, distinct correlation peaks are obtained in the 2D NMR spectra significantly reducing the spectral complexity in the ^1H dimension. This is an essential prerequisite for the following analysis of the formulations. While revealing valuable intra- and
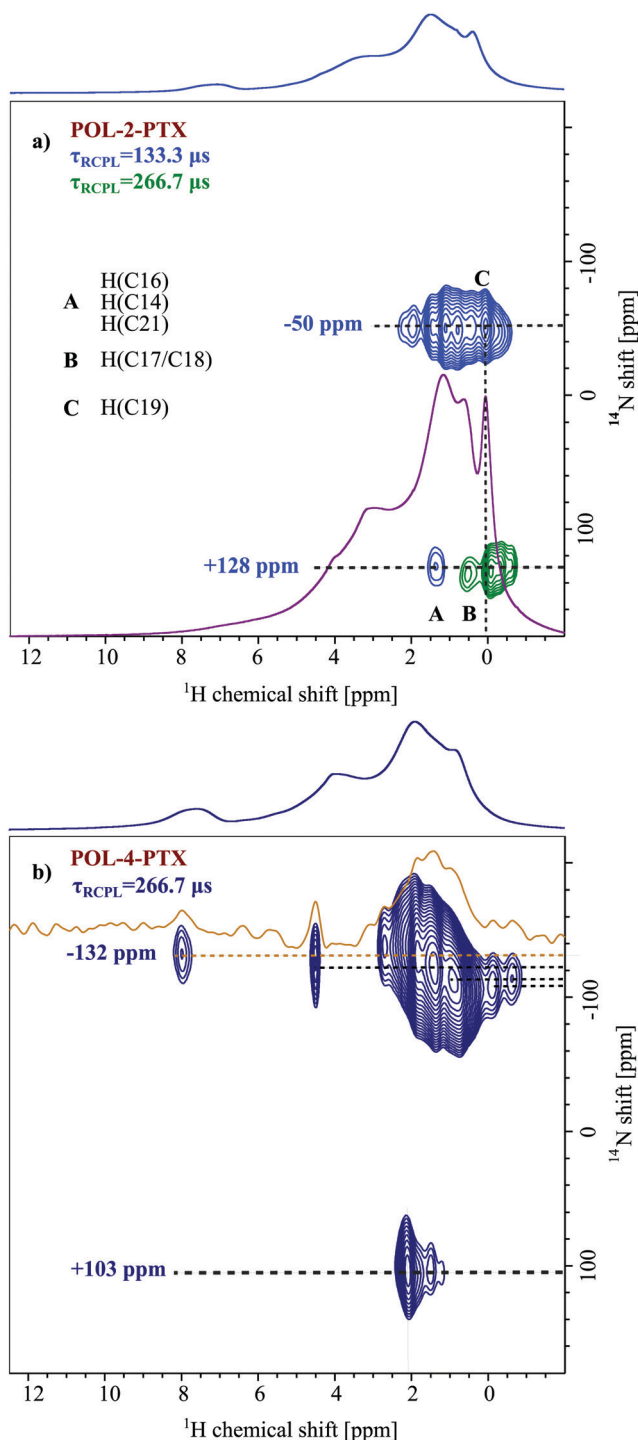
This journal is © The Royal Society of Chemistry 2020

J. Mater. Chem. B, 2020, **8**, 6827–6836 | **6831**

Table 1 Closest N$\cdots$H proximities[a] as extracted from PTX crystallographic data (CSD code: RIGLEA, PXRD data at 363.0 K)[24]

N$\cdots$H proximity	Distance/Å
$\underline{N}^A\underline{H}$	0.979
$\underline{N}^A H$–$C^{A32}\underline{H}$	1.642
$\underline{N}^A H$–$C^{A3'}\underline{H}$	2.031
$\underline{N}^A H$–$(C^{A2'}\underline{H}$–O$\underline{H})$	2.601
$\mathbf{\underline{N}^A H}$–$\mathbf{C^{A38}\underline{H}}$	**2.887**
$\underline{N}^B\underline{H}$	0.846
$\underline{N}^B H$–$C^{B3'}\underline{H}$	1.915
$\underline{N}^B H$–$(C^{B2'}\underline{H}$–O$\underline{H})$	2.486
$\underline{N}^B H$–$C^{A31}\underline{H}_3$	*2.787*
$\mathbf{\underline{N}^B H}$–$\mathbf{C^{B32}\underline{H}}$	**2.965**

[a] Intermolecular proximities in italics. Mobile aromatic units are shown in bold. N and H atoms of interest are underlined.

intermolecular N$\cdots$H proximities, the HMQC experiments also feature considerably shorter experimental times (1 h 30 min up to 7 h) than the 1D ^{15}N experiments (min 1 d), while also using significantly lower samples volumes (80 µL in 4 mm rotors *vs.* 1.5 µL in 1.3 mm rotors).

Formulations

Fig. 3 depicts ^{14}N–^{1}H HMQC MAS NMR spectra of two differently loaded formulations (a) POL-2-PTX and (b) POL-4-PTX, both with their ^{1}H MAS NMR spectra as external projections. In both spectra, two different ^{14}N shifts, one at positive and one at negative ppm values, can be observed with the cross-peaks at negative values being more intense than the corresponding signals at positive ^{14}N shifts. For the formulation with the lowest PTX loading (POL-2-PTX), all cross-peaks appear in the aliphatic ^{1}H chemical shift region below 2 ppm, the extracted ^{14}N shifts are −50 and +128 ppm. With increasing PTX loading of the formulations, both nitrogen shifts decrease to −132 and +103 ppm. Taking a closer look at the characteristic peaks for the medium loaded formulation, POL-4-PTX, cross-peaks are again observed in the aliphatic ^{1}H region and additional cross peaks at a proton chemical shift of 4.5 and 8.0 ppm can be clearly distinguished alongside weaker signals at 5.6 and 6.4 ppm (orange slice). The high ^{1}H chemical shift values are indicative of aromatic or hydrogen bonding environments. Interestingly, for this sample and in contrast to POL-2-PTX, multiple, defined ^{14}N shifts between −135 and −110 ppm are observed.

To complete the set of differently loaded formulations and subsequently extract trends, which might reveal information on changes of the local environment in the formulations, ^{14}N–^{1}H HMQC data were also recorded for POL-9-PTX, a formulation with almost 50 wt% PTX loading (Fig. 4). Due to hardware problems (untraceable spikes appearing in the FIDs) and despite multiple measurement attempts at different times (August 2019 and November 2019), unfortunately no artefact free dataset could be recorded. Therefore, the ^{14}N–^{1}H HMQC spectrum for POL-9-PTX was generated by addition of the individual FIDs of several datasets with different recoupling times ranging from 133.3 to 533.3 µs. The averaging of different datasets comes at the cost of resolution, particularly in the ^{1}H dimension. Consequently, only the ^{14}N shifts and relative signal intensities

Fig. 3 ^{14}N–^{1}H HMQC spectra (20 T, 60 kHz) of (a) the POL-2-PTX formulation recorded with recoupling times τ_{RCPL} = 133.3 µs (light blue) and τ_{RCPL} = 266.7 µs (green), both acquired with 18 t$_1$ FIDs, each with 1024 co-added transients for a recycle delay of 1.3 s (experimental time: 6 h 46 min), including tentative assignment of N$\cdots$H proximities. The base contour level is at 34% of the maximum peak height. The internal overlaid ^{1}H spectrum (purple) is that for POL. (b) The POL-4-PTX formulation recorded with a recoupling time τ_{RCPL} = 266.7 µs (dark blue), and 12 t$_1$ FIDs each acquired with 1200 co-added transients for a recycle delay of 1.3 s (experimental time: 5 h 17 min). The internal overlaid spectrum (orange) is the extracted slice at a ^{14}N shift of −132 ppm. The base contour level is at 22% of the maximum peak height. The skyline projections represent the ^{1}H one-pulse MAS NMR spectra of each sample.

6832 | *J. Mater. Chem. B*, 2020, **8**, 6827–6836

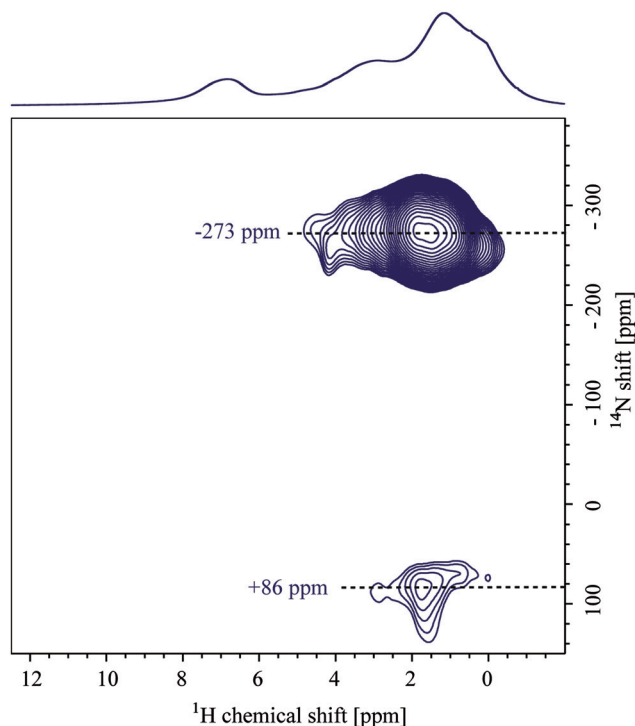This journal is © The Royal Society of Chemistry 2020

Fig. 4 ^{14}N–^{1}H HMQC (20 T, 60 kHz) spectrum of the POL-9-PTX formulation. The base contour level is at 34% of the maximum peak height. The skyline projection shows the corresponding ^{1}H one-pulse MAS NMR spectrum. Due to problems with the probe, the recorded datasets for this sample contained artefacts. Therefore, multiple datasets with different recoupling times varying from τ_{RCPL} = 133.3 μs to τ_{RCPL} = 533.3 μs (recycle delay of 1.0 s) were added to obtain the spectrum. Consequently, only the ^{14}N shift values were used for comparison.

are discussed in the course of this work. The values −273 and +86 ppm are consistent with the observed decrease in shift upon increasing the PTX loading.

All extracted values for both the individual components and the formulations are summarized in Table 1, which also includes selected ^{15}N chemical shifts extracted from the spectra shown in Fig. 1b. This first examination of the ^{14}N–^{1}H HMQC spectra of the three formulations is very promising as two different nitrogen environments can be distinguished for each sample, which follow a clear trend of decreasing ^{14}N shift with increasing loading. An analogous trend could not have been observed based on ^{15}N solid-state NMR data as indicated by the similarity of the extracted chemical shifts for the polymer and the formulation with highest PTX loading.

Discussion

In the next step, the observed trends and key N···H proximities have to be analyzed and transformed into chemical knowledge to improve our understanding of the studied formulations on the molecular level. To do so, ^{14}N quadrupolar shifts δQ_{iso} (for detailed explanation see SI 1, ESI†) can be estimated based on the hypothesis that the ^{14}N isotropic chemical shift are approximately identical to the ^{15}N isotropic chemical shifts.

Table 2 Overview of the experimentally determined ^{14}N shift values, selected ^{15}N chemical shifts and the resulting, calculated ^{14}N quadrupolar shifts

	$\delta ^{14}$N neg. ppm	$\delta ^{14}$N pos. ppm	$\delta ^{15}$N/ ppm	δQ_{iso}/ ppm
Crystalline PTX	−18/−30	—	−246/−260	228/230
Amorphous PTX	−55/−70	—		200[a]/185[a]
Pure POL	—	+67	−258/−263	325/330
POL-2-PTX	−50	+128		205/383
POL-4-PTX	−132	+103		123/358
POL-9-PTX	−273	+86	−263	−10/349

[a] Calculated as $\delta(^{14}$N)$-\delta(^{15}$N) using an average ^{15}N chemical shift of −255 ppm.

Consequently, the quadrupolar shift values can be determined by subtraction giving the values indicated in Table 2. If available, the corresponding experimental ^{15}N chemical shifts were used. For all formulations, a ^{15}N value of −263 ppm was used. For as-received and amorphous PTX, relatively large ^{14}N quadrupolar shifts of around 200 ppm are observed, which is indicative of the more asymmetric environment of the ^{14}N within a secondary amide. The data for the pure polymer, which only contains tertiary amides, reveals even larger quadrupolar shifts of above 300 ppm. Interestingly, the resulting quadrupolar shifts of all three formulations remain similarly sized for the ^{14}N signal observed at positive ppm values, which is further comparable in size to the neat polymer, while the quadrupolar shift of the ^{14}N signal at negative ppm values is decreasing with increasing PTX loading. This indicates a more symmetric N-environment at higher PTX loadings with the very low experimentally determined quadrupolar shift for POL-9-PTX verging on that of an almost tetrahedral arrangement. How can this major change in symmetry be explained?

To approach this question, it is first necessary to discuss the assignment of the two ^{14}N shifts observed for the formulations. At a first glance, the 2D NMR data of individual components, PTX and POL, showing positive as well as negative ^{14}N shifts in a similar region to the two shifts found for the formulations, suggest an analogous assignment for these two environments. However, for the lowest PTX loading (POL-2-PTX), only 2.2% of all nitrogen atoms in the sample belong to PTX, while the majority of nitrogen atoms originate from the polymer. Furthermore, no intramolecular NH contact like the one found in pure PTX is observed in the formulation with the lowest loading. For POL-4-PTX and POL-9-PTX, 4.5% and 10.1% of the nitrogen atoms in the sample are found in PTX molecules. With this in mind, we hypothesize that both ^{14}N signals arise from polymeric environments, the more intense signal at negative ppm values being assigned to amides in close proximity to PTX molecules acting as hydrogen bond donors and the signal at positive ppm resulting from the remaining amide fragments of the triblock copolymer. This agrees with the signal at negative ppm gaining intensity with respect to the other ^{14}N environment upon increasing the PTX loading. The tertiary amides can act as hydrogen bond acceptors and in doing so the nitrogen environment gets more symmetric, which results in a smaller quadrupolar shift. For example, this has been observed for

This journal is © The Royal Society of Chemistry 2020

J. Mater. Chem. B, 2020, **8**, 6827–6836 | **6833**

small di- and oligopeptides, where nitrogen atoms with three bonds and thus a less tetrahedral environment due to the lone pair showed high second order quadrupolar shifts, while in the case of zwitterionic RNH_3^+ environments (proton transfer being the extreme case of hydrogen bonding interaction) only a very small shift was observed.[28,36] Finally, the formulation with medium loading gives further insights into the drug–polymer assembly. While the amount of PTX in POL-2-PTX is very low and the ^{14}N–^{1}H HMQC is dominated by polymer–polymer contacts, distinct NH contacts with protons resonating above 4 ppm can be observed for the ^{14}N at negative ppm values in the ^{14}N–^{1}H HMQC spectrum of POL-4-PTX. All these cross-peaks can only arise from intermolecular drug–polymer contacts as the polymer itself does not show any proton chemical shifts above 3.9 ppm. Specifically, cross-peaks at 8.0, 6.4, 5.6 and 4.5 ppm were observed. In comparison with the NMR spectroscopy data of pure PTX, the cross-peak above 8 ppm can be assigned to a tertiary amide···HN proximity, while the remaining cross-peaks could result from interactions between the amide and different OH environments within PTX. Additionally, the spectrum of POL-4-PTX contains diverse ^{14}N shifts. As this feature is neither observed for the neat polymer nor for POL-2-PTX, where only one distinct ^{14}N shift is observed, it must be attributed to the increasing amounts of PTX present in the nanoparticles. Taking a closer look at the known structures of PTX with increasing number of water molecules could help to shed light on this: in the three structures published by Vella-Zarb et al.,[25] the NH group and all three OH-groups act as hydrogen bond donors to adjacent PTX and water molecules suggesting that this would also be the case for PTX–polymer interactions. The polymer amide nitrogen atoms serve as the hydrogen bond acceptor. From the previous work on similar polymers with PTX and curcumin,[11,19,49] we know that, with increasing loading, the poorly water-soluble guest not only interacts with the more hydrophobic pBuOx polymer block, but also with the hydrophilic pMeOx units. The critical drug loading, where the corona become significantly involved appears to be between 20–30 wt%. This would explain, why we don't observe this for the lowest loading. Furthermore, steric hindrance between the different PTX interaction sites and pBuOx vs. pMeOx would result in a differing deviation from ideal hydrogen bond geometries with respect to bond distances and bond angles,

while, overall, the hydrogen bonded amide nitrogen atom would be found in a more symmetric, closer to tetrahedral environment as compared to the planar, sp^2 hybridized initial environment (Fig. 5).

This underlines that ^{14}N–^{1}H HMQC NMR experiments are not only spreading out the nitrogen NMR signals but are also a promising tool to study the local symmetry and detect structure determining intermolecular interactions in complex and amorphous drug–polymer formulations. To further improve the structural understanding, these finding now need to be complemented by additional experimental and detailed theoretical data.

Summary and conclusion

In this work, we investigated amorphous polymer formulations of the anti-cancer drug paclitaxel. For both the polymer and the drug, ^{15}N chemical shifts in a very similar spectral area were observed, which results in significant signal overlap, especially if amorphous samples are involved. Consequently, for this set of samples, it is very challenging to distinguish small changes in the spectra, extract trends and information on the interactions of specific moieties, e.g. upon increasing the drug loading of the formulations. Therefore, ^{14}N–^{1}H HMQC NMR experiments were investigated as a valuable tool to disperse signals due to the additional quadrupolar shift when observing ^{14}N instead of ^{15}N. We could show that such experiments can be a rich source of information for the characterization of molecular interactions in amorphous polymer–drug nanoformulations, which is otherwise difficult to obtain. On the one hand, the ^{14}N signals were dispersed so that two distinct ^{14}N environments could be extracted for each formulation and the complexity in the ^{1}H dimension could be reduced through this correlation experiment. Thus, it was possible to extract trends for different drug loadings, distinguish cross peaks and extract quadrupolar parameters, which altogether enabled us to learn about the local amide environment, its symmetry and potential interacting motifs between the drug and polymer in such complex amorphous mixtures. Overall, the ^{14}N–^{1}H HMQC NMR experiments have great potential for the analysis of disordered and amorphous drug-delivery systems, which can be transferred and should be explored for other systems. Here, the ^{14}N–^{1}H experiments could also be insightful for nanocrystalline materials such as those found in Pluronic F127 stabilized PTX nanocrystals.[50]

It is of importance to stress for the broader applicability of the ^{14}N–^{1}H HMQC experiment that while fast MAS (≥ 60 kHz) is essential for these experiments due to the narrowing of the ^{1}H signal and most importantly increased ^{1}H coherence lifetimes,[28] the experiments are not limited to high magnetic fields. With the second order quadrupolar interaction being inversely proportional to the strength of the magnetic field, narrower lines are obtained at higher fields. However, a larger dispersion of the signals is counterbalancing this at lower magnetic field strengths. In fact, many examples for the application of this and other ^{14}N based experiments in the literature show their feasibility at 400–600 MHz.[30,34,36,51]
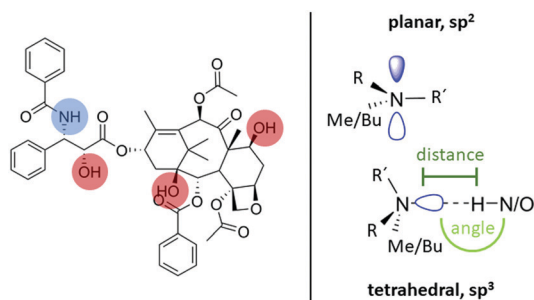

Fig. 5 Summary of the hydrogen bond donating moieties in PTX alongside nitrogen atom geometries and environments for initial tertiary amides and hydrogen bonded functionalities.

6834 | J. Mater. Chem. B, 2020, **8**, 6827–6836

This journal is © The Royal Society of Chemistry 2020

Furthermore, in a next step we intend to combine these experiments with additional data and complementary calculations to learn more about these PTX formulations and ultimately derive realistic structural models on a molecular level. In this context, molecular dynamics simulations could provide important insights due to the possibility to reproduce distributions of environments encountered for amorphous drug–polymer formulations.

Conflicts of interest

There are no conflicts to declare.

Acknowledgements

Notes and references

1 P. Ma and R. J. Mumper, *J. Nanomed. Nanotechnol.*, 2013, **4**, 1000164.
2 T.-H. Wang, H.-S. Wang and Y.-K. Soong, *Cancer*, 2000, **88**, 2619–2628.
3 A. M. Sofias, M. Dunne, G. Storm and C. Allen, *Adv. Drug Delivery Rev.*, 2017, **122**, 20–30.
4 Y. S. Youn and Y. H. Bae, *Adv. Drug Delivery Rev.*, 2018, **130**, 3–11.
5 Z. He, A. Schulz, X. Wan, J. Seitz, H. Bludau and D. Y. Alakhova, *et al.*, *J. Controlled Release*, 2015, **208**, 67–75.
6 Y. Fujiwara, H. Mukai, T. Saeki, J. Ro, Y.-C. Lin and S. E. Nagai, *et al.*, *Br. J. Cancer*, 2019, **120**, 475.
7 Z. He, X. Wan, A. Schulz, H. Bludau, M. A. Dobrovolskaia and S. T. Stern, *et al.*, *Biomaterials*, 2016, **101**, 296–309.
8 R. Luxenhofer, A. Schulz, C. Roques, S. Li, T. K. Bronich and E. V. Batrakova, *et al.*, *Biomaterials*, 2010, **31**, 4972–4979.
9 A. Schulz, S. Jaksch, R. Schubel, E. Wegener, Z. Di and Y. Han, *et al.*, *ACS Nano*, 2014, **8**, 2686–2696.
10 S. Jaksch, A. Schulz, Z. Di, R. Luxenhofer, R. Jordan and C. M. Papadakis, *Macromol. Chem. Phys.*, 2016, **217**, 1448–1456.
11 B. Sochor, Ö. Düdükcü, M. M. Lübtow, B. Schummer, S. Jaksch and R. Luxenhofer, *Langmuir*, 2020, **36**, 3494–3503.
12 R. F. Moran, D. M. Dawson and S. E. Ashbrook, *Int. Rev. Phys. Chem.*, 2017, **36**, 39–115.
13 S. E. Ashbrook and P. Hodgkinson, *J. Chem. Phys.*, 2018, **149**, 040901.
14 P. Florian and F. Fayon, *Disordered Solids. Modern Methods in Solid-state NMR: A Practitioner's Guide*, The Royal Society of Chemistry, 2018, ch. 12, pp. 356–90.
15 R. K. Harris, *J. Pharm. Pharmacol.*, 2007, **59**, 225–239.
16 H. G. Brittain. *Polymorphism in Pharmaceutical Solids*, CRC Press, 2nd edn, 2009.
17 S. Baghel, H. Cathcart and N. J. O'Reilly, *J. Pharm. Sci.*, 2016, **105**, 2527–2544.
18 M. Callari, P. L. De Souza, A. Rawal and M. H. Stenzel, *Angew. Chem., Int. Ed.*, 2017, **56**, 8441–8445.
19 A. C. Pöppler, M. M. Lübtow, J. Schlauersbach, J. Wiest, L. Meinel and R. Luxenhofer, *Angew. Chem., Int. Ed.*, 2019, **58**, 18540–18546.
20 D. A. Hirsh, A. V. Wijesekara, S. L. Carnahan, I. Hung, J. W. Lubach and K. Nagapudi, *et al.*, *Mol. Pharmaceutics*, 2019, **16**, 3121–3132.
21 S. K. Vasa, P. Rovó and R. Linser, *Acc. Chem. Res.*, 2018, **51**, 1386–1395.
22 S. P. Brown, *Solid State Nucl. Magn. Reson.*, 2012, **41**, 1–27.
23 R. Zhang, K. H. Mroue and A. Ramamoorthy, *Acc. Chem. Res.*, 2017, **50**, 1105–1113.
24 Y. Nishiyama, *Solid State Nucl. Magn. Reson.*, 2016, **78**, 24–36.
25 L. Vella-Zarb, U. Baisch and R. E. Dinnebier, *J. Pharm. Sci.*, 2013, **102**, 674–683.
26 J. K. Harper, D. H. Barich, E. M. Heider, D. M. Grant, R. R. Franke and J. H. Johnson, *et al.*, *Cryst. Growth Des.*, 2005, **5**, 1737–1742.
27 E. M. Heider, J. K. Harper and D. M. Grant, *Phys. Chem. Chem. Phys.*, 2007, **9**, 6083–6097.
28 A. S. Tatton, J. P. Bradley, D. Iuga and S. P. Brown, *Z. Phys. Chem.*, 2012, **226**, 1187–1204.
29 A. S. Tatton, T. N. Pham, F. G. Vogt, D. Iuga, A. J. Edwards and S. P. Brown, *Mol. Pharmaceutics*, 2013, **10**, 999–1007.
30 E. K. Corlett, H. Blade, L. P. Hughes, P. J. Sidebottom, D. Walker and R. I. Walton, *et al.*, *Solid State Nucl. Magn. Reson.*, 2020, DOI: 10.1016/j.ssnmr.2020.101662.
31 A. G. M. Rankin, J. Trébosc, P. Paluch, O. Lafon and J.-P. Amoureux, *J. Magn. Reson.*, 2019, **303**, 28–41.
32 G. N. M. Reddy, D. S. Cook, D. Iuga, R. I. Walton, A. Marsh and S. P. Brown, *Solid State Nucl. Magn. Reson.*, 2015, **65**, 41–48.
33 Z. Gan, J. P. Amoureux and J. Trebosc, *Chem. Phys. Lett.*, 2007, **435**, 163–169.
34 S. Cavadini, *Prog. Nucl. Magn. Reson. Spectrosc.*, 2010, **56**, 46–77.
35 K. Maruyoshi, D. Iuga, O. N. Antzutkin, A. Alhalaweh, S. P. Velaga and S. P. Brown, *Chem. Commun.*, 2012, **48**, 10844–10846.
36 Y. l. Hong, T. Asakura and Y. Nishiyama, *ChemPhysChem*, 2018, **19**, 1841–1845.

This journal is © The Royal Society of Chemistry 2020

J. Mater. Chem. B, 2020, **8**, 6827–6836 | **6835**

37 A. S. Tatton, T. N. Pham, F. G. Vogt, D. Iuga, A. J. Edwards and S. P. Brown, *CrystEngComm*, 2012, **14**, 2654–2659.

38 A. S. Tatton, H. Blade, S. P. Brown, P. Hodgkinson, L. P. Hughes and S. O. N. Lill, *et al.*, *Cryst. Growth Des.*, 2018, **18**, 3339–3351.

39 D. Bernasconi, S. Bordignon, F. Rossi, E. Priola, C. Nervi and R. Gobetto, *et al.*, *Cryst. Growth Des.*, 2020, **20**, 906–915.

40 E. Vitaku, D. T. Smith and J. T. Njardarson, *J. Med. Chem.*, 2014, **57**, 10257–10274.

41 S. Cavadini, A. Abraham and G. Bodenhausen, *Chem. Phys. Lett.*, 2007, **445**, 1–5.

42 S. P. Brown, *High-resolution 1H 2D Magic-angle Spinning Techniques for Organic Solids. Modern Methods in Solid-state NMR*, A Practitioner's Guide: The Royal Society of Chemistry, 2018, ch. 2, pp. 39–74.

43 M. M. Lübtow, L. Hahn, M. S. Haider and R. Luxenhofer, *J. Am. Chem. Soc.*, 2017, **139**, 10980–10983.

44 T. Oas, R. Griffin and M. Levitt, *J. Chem. Phys.*, 1988, **89**, 692–695.

45 P. Costa, J. Gross, M. Hong and R. Griffin, *Chem. Phys. Lett.*, 1997, **280**, 95–103.

46 B. Fung, A. Khitrin and K. Ermolaev, *J. Magn. Reson.*, 2000, **142**, 97–101.

47 C. R. Morcombe and K. W. Zilm, *J. Magn. Reson.*, 2003, **162**, 479–486.

48 M. M. Lübtow, M. S. Haider, M. Kirsch, S. Klisch and R. Luxenhofer, *Biomacromolecules*, 2019, **20**, 3041–3056.

49 M. S. Haider, M. M. Lübtow, S. Endres, V. Aseyev, A.-C. Pöppler and R. Luxenhofer, *ACS Appl. Mater. Interfaces*, 2020, **12**, 24531–24543.

50 J. Deng, L. Huang and F. Liu, *Int. J. Pharm.*, 2010, **390**, 242–249.

51 D. Carnevale, X. Ji and G. Bodenhausen, *J. Chem. Phys.*, 2017, **147**, 184201.

6836 | *J. Mater. Chem. B*, 2020, **8**, 6827–6836

This journal is © The Royal Society of Chemistry 2020

Supporting Information

14N-1H HMQC solid-state NMR as a powerful tool to study amorphous formulations – an exemplary study of paclitaxel loaded polymer micelles

Marvin Grüne[a], Robert Luxenhofer[b], Dinu Iuga[c], Steven P. Brown[c], and Ann-Christin Pöppler*[a]

[a] Institute of Organic Chemistry, University of Würzburg, Am Hubland, 97074 Würzburg, Germany

[b] Lehrstuhl für Chemische Technologie der Materialsynthese, University of Würzburg, Röntgenring 11, 97070 Würzburg, Germany

[c] Department of Physics, University of Warwick, Coventry, CV4 7AL, United Kingdom

Supporting Information

Content:

SI 1: Calculation of the second-order isotropic quadrupolar shift[1]

For a quadrupolar nucleus, in addition to the isotropic chemical shift, there is an isotropic second-order quadrupolar shift: For the (m, $m-1$) transition, this is given in ppm as:[2, 3]

$$\delta_{iso}^{Q} = \left\{ -\frac{\frac{3}{40}\left(\frac{P_Q}{\nu_O}\right)^2 [I(I+1) - 9m(m-1) - 3]}{[I^2(2I-1)^2]} \right\} \times 10^6$$

where ν_0 is the Lamor frequency in Hz and the quadrupolar product, P_Q, is defined as:

$$P_Q = C_Q \sqrt{\left[1 + \frac{\eta_Q^2}{3}\right]}$$

The quadrupolar coupling constant, C_Q, and asymmetry, η_Q, depend on the principal components of the electric field gradient tensor that are ordered such that: $|V_{ZZ}| \geq |V_{YY}| \geq |V_{XX}|$. Specifically, the quadrupolar coupling constant, C_Q, (in units of Hz) is given by:

$$C_Q = \frac{V_{ZZ}eQ}{h} = \frac{e^2qQ}{h}$$

where Q is the nuclear quadrupole moment and q is the electric field gradient, and e and h are the charge of an electron and Planck's constant, repectively. The asymmetry is defined as:

$$\eta_Q = \frac{V_{XX} - V_{YY}}{V_{ZZ}}$$

SI 2: Pulse Sequence
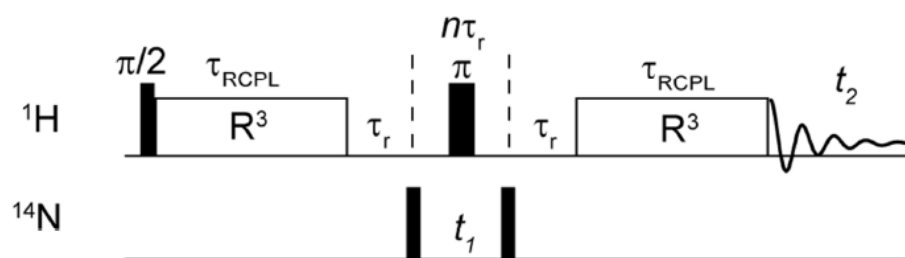
Figure S1: ^{14}N-^{1}H HMQC pulse sequence using the R³ rotary resonance sequence to recouple heteronuclear dipolar couplings.[1]

All NMR data of this manuscript is uploaded at the Warwick Research Archive Portal (WRAP). Thus, the full compiled pulse sequence as used for the experiments is available as a text document. For further information on practical aspects of ^{14}N-^{1}H HMQC experiments the reader is also referred to chapter 2 in the book "Modern Methods in Solid-state NMR: A Practitioner's Guide".[4]

SI 3: Preparation of the Paclitaxel (PTX)-Polymer Formulations and amorphous Paclitaxel

The three formulations with different drug load were prepared according to existing preparation protocols.[5] Throughout this manuscript, the formulations are referred to as POL-2-PTX, POL-4-PTX and POL-9-PTX. The numbers 2,4 and 9 describe the polymer to drug ratio (by weight) of the formulation. The different concentrations used for preparation and the median hydrodynamic radius (literature data) of the micelles are listed in Table S1.

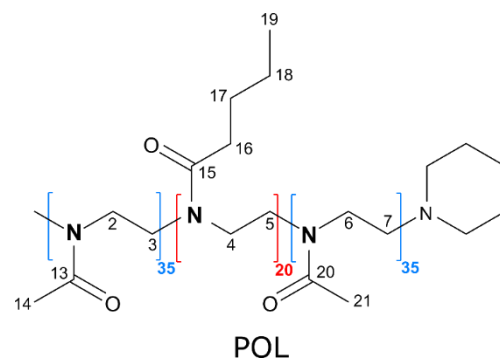| Formulation	Ratio (POL/PTX) (w/w)	% wt	Concentration POL (g/L)	Solubilized concentration PTX (g/L)	Median Hydrodynamic Radius (R_h)[6]
P2-2-PTX	10:2	17 %	10 g/L	2 g/L	6 nm
P2-4-PTX	10:4	29 %	10 g/L	4 g/L	8 nm
P2-9-PTX	10:9	47 %	10 g/L	9 g/L	11 nm

All three formulations were produced by combining the appropriate amount of ethanolic polymer and PTX solutions. Ethanol was then evaporated, the resulting thin film dissolved in H_2O and lyophilized to give a white powder.

Lyophilization was also used to prepare amorphous PTX. PXRD data shown in figure S4 confirmed the amorphicity.

SI 4: Chemical shifts of the Polymer (POL) in solution

Assignment of the ^{1}H and ^{13}C chemical shifts in solution, was carried out based on a standard set of 1D and 2D NMR experiments including ^{1}H-^{1}H COSY, ^{1}H-^{13}C HSQC and HMBC experiments. In CDCl$_3$, the individual polymer strands do not self-assemble, while in D$_2$O the amphiphilic triblock copolymer forms spherical and wormlike micellar structures.

C	CDCl$_3$ [ppm]	D$_2$O [ppm]		H of C	CDCl$_3$ [ppm]	D$_2$O [ppm]
2,3,6,7	48.1-43.7	46.3, 44.2,		2,3,6,7	3.49-3.25	3.51-3.47
4,5		47.2, 46.7		4, 5		3.63-3.57
13/20	171.5, 170.9	174.3				
14/21	21.3	20.2		14/21	2.14-2.08	2.09-2.02
15	174.0, 173.4	Not visible				
16	32.6	32.3		16	2.37-2.31,	2.36-2.26
17	27.4	27.3		17	1.61-1.53	1.51-1.47
18	22.7	22.0		18	1.39-1.30	1.34-1.27
19	14.1	13.3		19	0.93-0.90	0.89-0.85

Further discussion related to Figure 2b in the main manuscript:

1) **Assignment:** The ^{13}C chemical shifts in the solid state agreed well with the chemical shifts observed in solution and also with a structurally similar polymer with a propyl instead of a butyl sidechain (ref. 18). For the ^{1}H chemical shift assignment, NMR data in solution alongside [1]H-^{1}H NOESY-like solid-state NMR spectra in the solid state were used (Figure S2). At lowest mixing time (Figure S2a, 20 ms), the end group of the propyl chain (Me, 19) is in contact with the adjacent signal (17,18) and to a lesser extent with the next signal at higher ppm, while this signal (14,16,21) is the only one showing cross-peaks to the backbone of the polymer (arrow, 2-7). With increasing mixing time, first an additional signal between the CH$_2$ groups of the butyl chain (17,18) and the backbone (Figure S2b) and upon further increase finally to the Bu-CH$_3$ group (Figure S2c) is observed.
2) **Discussion of the HMQC signals:** Another interesting feature is the broadening of the backbone resonance upon increasing the mixing time. The backbone is the most rigid area of the triblock copolymer. Although the recoupling times in the HMQC are on a much shorter timescale, signal loss due to relaxation could be a possibility for the absence of N···H contacts to the backbone protons. Furthermore, even without guest molecules, the polymers form micellar nanoparticles. In these self-assembled systems, proximity between the butyl chain of one polymer block with a nitrogen atom

from a more distant repeating unit or a different polymer chain is more likely than a backfolding of the butyl chain to generate contact to the directly bound nitrogen.
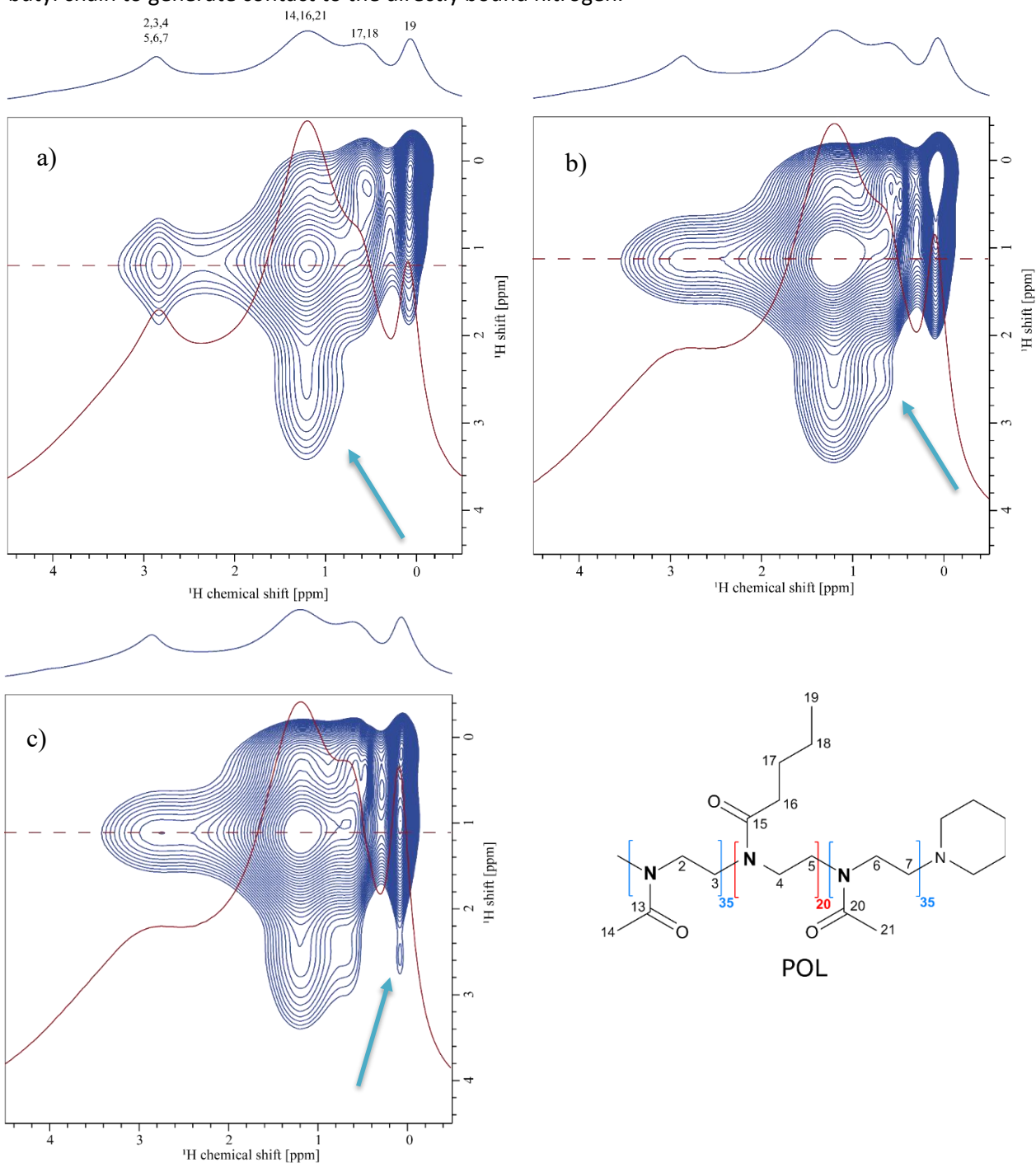
Figure S2: ^{1}H-^{1}H NOESY-like solid-state NMR spectrum recorded at 20 T and a MAS frequency of 60 kHz for POL (heated above T$_g$ prior to the measurement), using a mixing time of a) τ_{mix} = 20 ms, b) τ_{mix} = 50 ms and τ_{mix} = 100 ms. 178 t_1 FIDs increments were acquired for each experiment using a recycle delay of 1.8 s, each with 32 co-added transients. The base contour level is at 22% (a) and 40% (b, c) of the maximum peak height. The corresponding ^{1}H one-pulse MAS NMR spectrum is shown as external projection.

SI 5: NMR characterization of PTX in solution

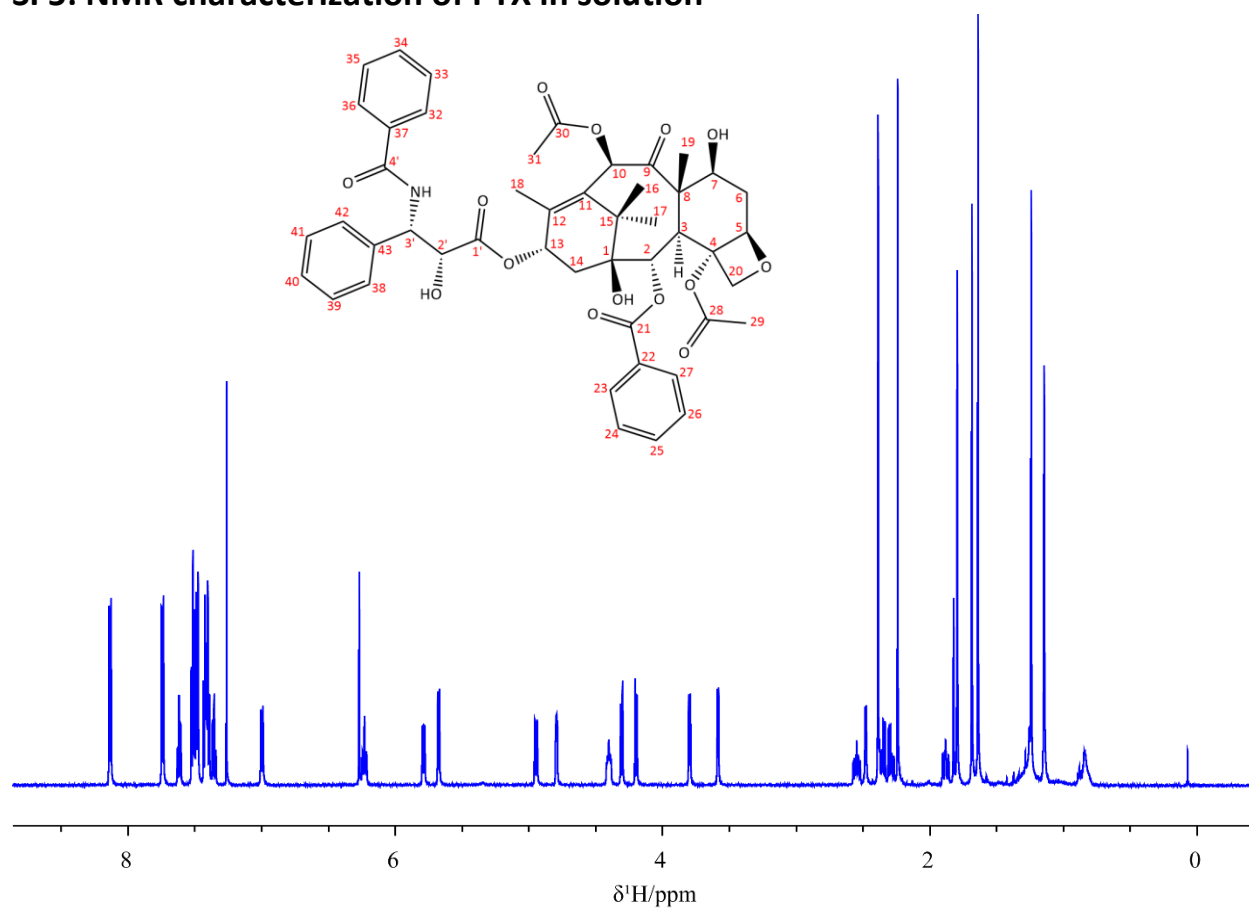**Figure S3a:** ^{1}H NMR spectrum of pure PTX (as received) in CDCl₃, recorded with 16 scans and a recycle delay of 5.8 s. The dataset was recorded on a Bruker Avance III HD 14.1 T spectrometer equipped with a 5 mm BBFO BB/19F-1H/D probe at 295.2 K. The temperature was calibrated using 4% MeOH in MeOD.

Figure S3b: $^{13}C/(^{1}H)$ NMR spectrum of pure PTX (as received) in CDCl$_3$, recorded with 8192 scans and a recycle delay of 2.8 s. The dataset was recorded on a Bruker Avance III HD 14.1 T spectrometer equipped with a 5 mm BBFO BB/19F-1H/D probe at 295.2 K. The temperature was calibrated using 4% MeOH in MeOD.
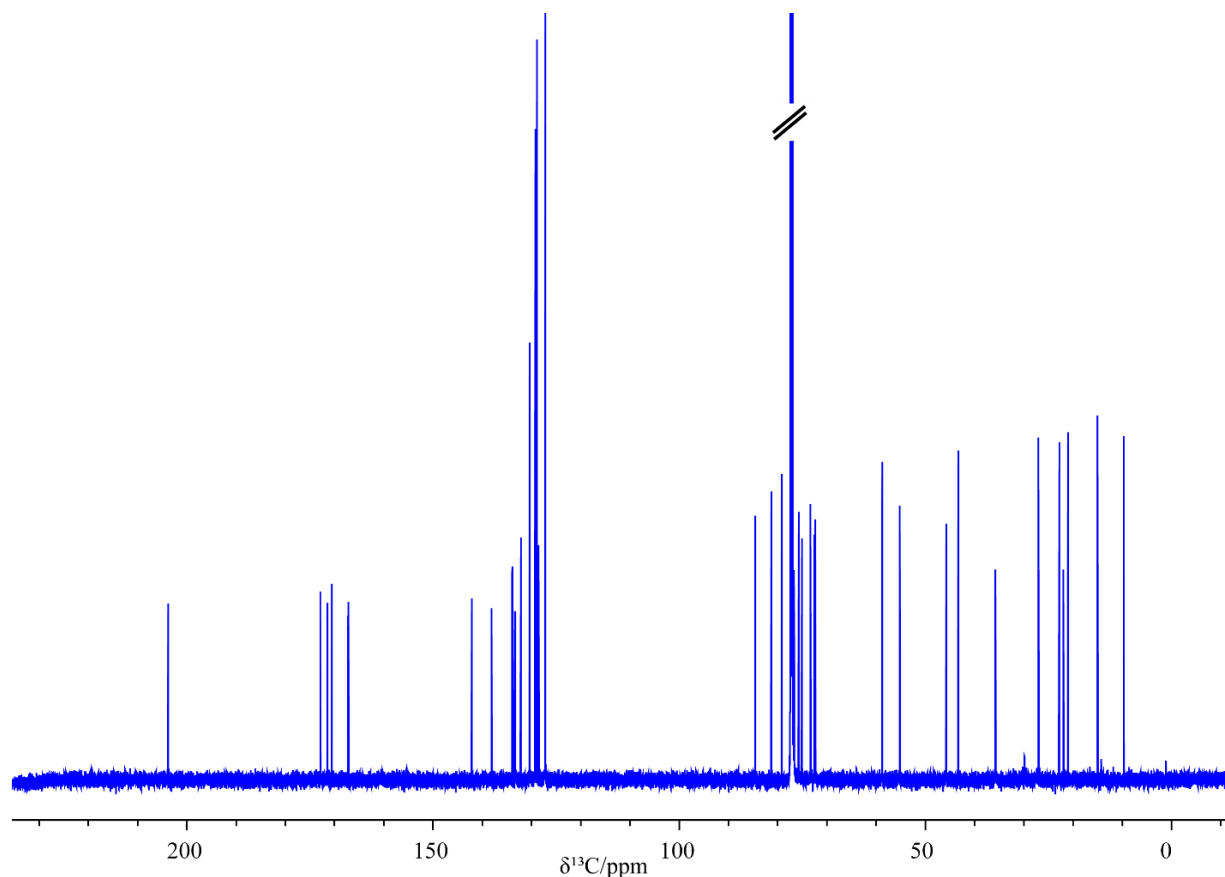
For clarity, the following ^{1}H NMR assignment for PTX uses the carbon numbering scheme from above in the way that, for example, C25, indicates the proton bound to carbon C25.

^{1}**H-NMR** (600.4 MHz, CDCl$_3$): δ = 8.13 (m, 2 H, CH, C23/27 (*o*)), 7.74 (m, 2 H, CH, C33/35 (*m*)), 7.61 (m, 1 H, CH, C25 (*p*)), 7.52-7.47 (m, 5 H, CH, C24/26 (*m*), C34(*p*), C38/42 (*o*)), 7.43-7.40 (m, 4 H, CH, C32/36 (*o*), C39/41 (*m*)), 7.35 (m, 1 H, CH, C40 (*p*)), 6.99 (d, 1 H, NH, $^{3}J_{C3'-NH}$ = 8.9 Hz, NH). 6.27 (s, 1 H, CH, C10), 6.23 (m, 1 H, CH, C13), 5.79 (dd, 1 H, CH, $^{3}J_{C2'-C3'}$ = 2.6 Hz, $^{3}J_{C3'-NH}$ = 8.9 Hz, C3'), 5.67 (d, 1 H, CH, $^{3}J_{C2-C3}$ = 7.0 Hz, C2), 4.95 (dd, 1 H, CH, $^{3}J_{C5-C6a}$ = 1.9 Hz, $^{3}J_{C5-C6e}$ = 9.6 Hz, C5), 4.79 (d, 1 H, CH, $^{3}J_{C2'-C3'}$ = 2.7 Hz, C2'), 4.40 (dd, 1 H, CH, $^{3}J_{C7-C6a}$ = 10.9 Hz, $^{3}J_{C7-C6e}$ = 6.8 Hz, C7), 4.31 (d, 1 H, CH$_2$, $^{2}J_{C20-C20}$ = 8.5 Hz, C20), 4.19 (d, 1 H, CH$_2$, $^{2}J_{C20-C20}$ = 8.5 Hz, C20), 3.80 (d, 1 H, CH, $^{3}J_{C2-C3}$ = 7.0 Hz, C3), 3.57 (s, 3 H, CH$_3$, C2'-OH), 2.59-2.48 (ddd, 1 H, CH, $^{2}J_{C6a-C6e}$ = 15.0 Hz, $^{3}J_{C5-C6e}$ = 9.7 Hz, $^{3}J_{C7-C6e}$ = 6.7 Hz, C6e), 2.47 (s, 1 H, OH, C7-OH), 2.39 (s, 3 H, CH$_3$, C29), 2.35 (dd, 1 H, CH, $^{2}J_{C14a-C14e}$ = 15.4 Hz, $^{3}J_{C13-C14e}$ = 9.0 Hz, C14e), 2.28 (dd, 1 H, CH, $^{2}J_{C14a-C14e}$ = 15.4 Hz, $^{3}J_{C13-C14a}$ = 9.0 Hz, C14a), 2.24 (s, 3 H, CH$_3$, C31), 1.92-1.85 (ddd, 1 H, CH, $^{2}J_{C6a-C6e}$ = 14.7 Hz, $^{3}J_{C5-C6a}$ = 2.3 Hz, $^{3}J_{C7-C6a}$ = 11.0 Hz, C6a), 1.79 (d, 3 H, CH$_3$, $^{4}J_{C18-C13}$ = 1.1 Hz, C18), 1.68 (s, 3 H, CH$_3$, C19), 1.24 (s, 3 H, CH$_3$, C16), 1.14 (s, 3 H, CH$_3$, C17) ppm.

13C-NMR (100.6 MHz, CDCl$_3$): δ = 203.8 (1 C, C$_q$, C9), 172.9 (1 C, C$_q$, C1'), 171.4 (1 C, C$_q$, C30), 170.5 (1 C, C$_q$, C28), 167.2 (1 C, C$_q$, C21), 167.2 (1 C, C$_q$, C4'), 142.1 (1 C, C$_q$, C12), 138.1 (2 C, C$_q$, C37/43), 133.9 (1 C, C$_q$, C22), 133.7 (1 C, CH, C25 (*p*)), 133.3 (1 C, C$_q$, C11), 132.1 (1 C, CH, C34 (*p*)), 130.4 (2 C, CH, C23/27 (*o*)), 129.3 (2 C, CH, C38/42 (*o*)), 129.2 (1 C, CH, C39/41 (*m*)), 128.88 (1 C, CH, C39/41 (*m*)), 128.86 (4 C, CH, C24/26 (*m*), C32/36 (*o*)), 128.5 (1 C, CH, C40 (*p*)), 127.2 (2 C, CH, C33/35 (*m*)), 127.2 (2 C, CH, C38/42 (*o*)), 84.6 (1 C, CH, C5), 81.3 (1 C, C$_q$, C4), 79.2 (1 C, C$_q$, C1), 76.7 (1 C, CH$_2$, C20), 75.7 (1 C, CH, C10), 75.1 (1 C, CH, C2), 73.3 (1 C, CH, C2'), 72.5 (1 C, CH, C13), 72.3 (1 C, CH, C7), 58.8 (1 C, C$_q$, C8), 55.2 (1 C, CH, C3'), 45.7 (1 C, CH, C3), 43.3 (1 C, C$_q$, C15), 35.8 (1 C, CH$_2$, C14), 35.7 (1 C, CH$_2$, C6), 27.0 (1 C, CH$_3$, C16a), 22.8 (1 C, CH$_3$, C29), 22.0 (1 C, CH$_3$, C17e), 21.0 (1 C, CH$_3$, C31), 15.0 (1 C, CH$_3$, C18), 9.7 (1 C, CH$_3$, C19) ppm.

SI 6: ^{1}H NMR spectra of unloaded and loaded polymer micelles in D$_2$O recorded with a cryoprobe
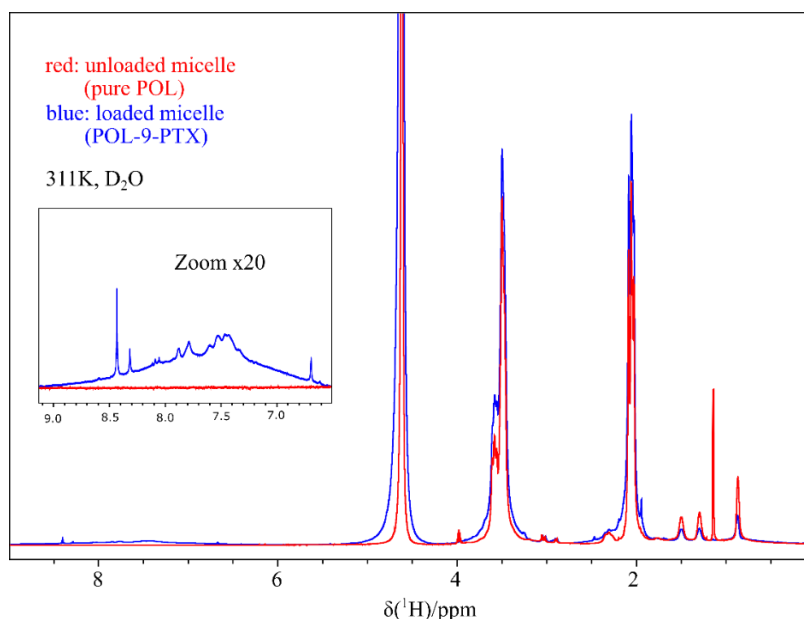
Figure S4a: ^{1}H NMR spectra of pure POL (red), forming an unloaded micelle in D$_2$O, and of a loaded micelle (POL-9-PTX) in D$_2$O (blue), recorded with a recycle delay of 5.8 s with 64 and 400 co-added transients, respectively. Both datasets were measured on a 14.1 T Bruker Avance III HD spectrometer equipped with a 5 mm ^{13}C/^{1}H cryoprobe at 311 K. The temperature was calibrated using 80% ethylene glycol in DMSO-d$_6$.
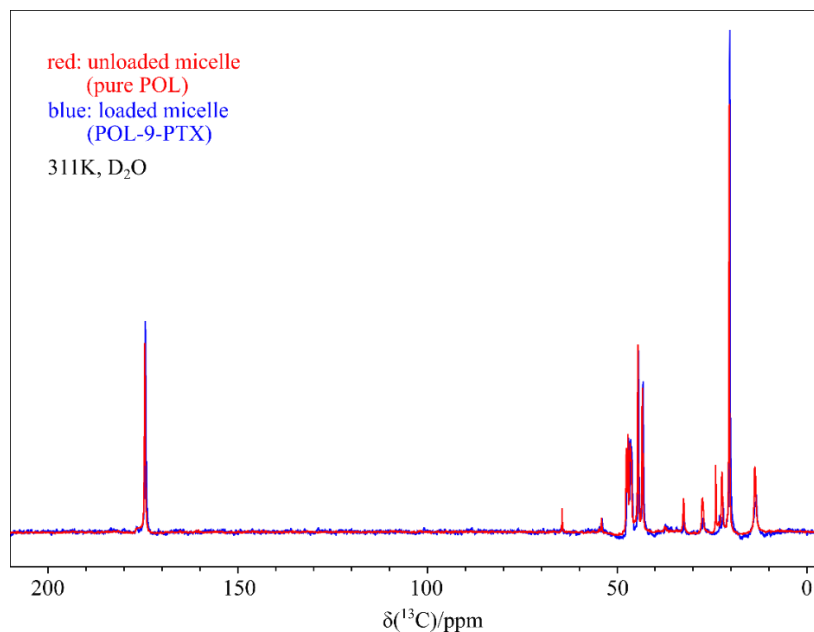
Figure S4b: Proton decoupled ^{13}C NMR spectra of pure POL (red), forming an unloaded micelle in D_2O, recorded with 26624 co-added transients and of the loaded micelle (POL-9-PTX) in D_2O (blue), recorded with 26562 co-added transients. Both datasets were measured for a recycle delay of 2.8 s on a 14.1 T Bruker Avance III HD spectrometer equipped with a 5 mm ^{13}C/^{1}H cryoprobe at 311 K. The temperature was calibrated using 80% ethylene glycol in DMSO-d_6.

Figure S3a and S3b show ^{1}H and ^{13}C NMR spectra of unloaded as well as of PTX-loaded polymer micelles. All spectra were recorded at 311K to mimic body temperature conditions in blood circulation. In Figure S3a, the aromatic region of the protons (enlarged region) is of particular interest. This region only contains PTX signals. Due to the low signal intensity and the broad line widths, it is challenging to investigate the incorporation of PTX into the micelles via ^{1}H NMR data in solution. Figure S3b demonstrates that even after recording more than 26000 scans for a ^{13}C NMR experiment in solution using a cryoprobe at 14.1 T, no visible signals of the PTX appear between 70 and 150 ppm. In this region, no POL peaks would be expected.

SI 7: PXRD measurements
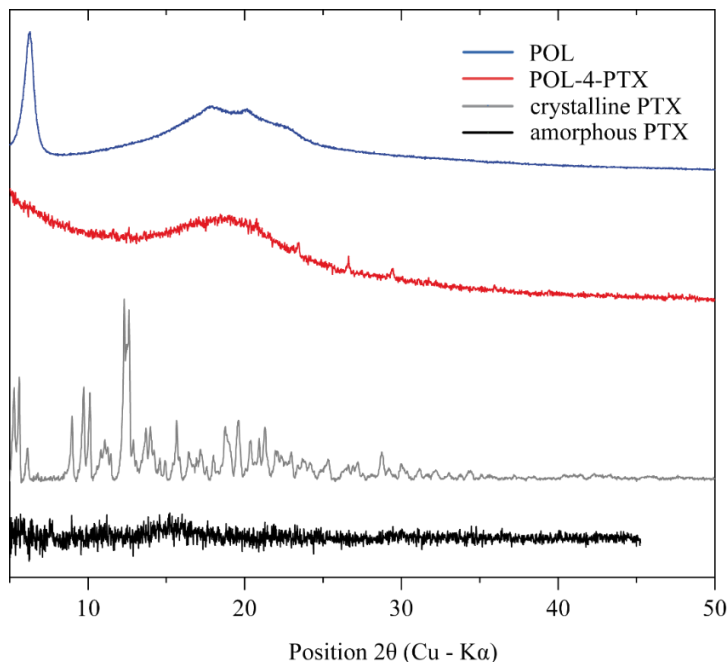
Figure S5: PXRD data of POL (blue), an exemplary formulation POL-4-PTX (red), crystalline PTX (grey) and amorphous PTX (black). Powder diffraction data was recorded on a Bruker Discover D8 powder diffractometer (Karlsruhe, Germany) using Cu Kα radiation (unsplit Kα1+Kα2 doublet, mean wavelength λ= 154.19 pm) at a power of 40 kV and 40 mA, a focusing Goebel mirror, and a 2.5° axial Soller slit. The scattered X-ray beam went through a receiving slit (3.3°). Detection was achieved with a LynxEye-1D-Detector (Bruker AXS) using the full detector range of 192 channels. Measurements were done in reflection geometry in coupled two theta/theta mode with a step size of 0.025° in the range 2θ of 5° to 45° (black) or 50° (blue, red, grey). The software package DIFFRAC.Suite (V2 2.2.690, BrukerAXS 2009–2011, Karlsruhe, Germany) was used for data collection. The diffraction data was subsequently converted into ASCII format and further handled with Origin (OriginLab, Massachusetts, USA).

POL-4-PTX mainly shows the expected amorphous character. The two peaks between 25-30° correspond to PTX, which still forms some small ordered phases within the formulation. Different PTX batches of the same company yielded slightly different phases, which is further discussed in SI 8.

SI 8: Solid-state NMR - ^{14}N-^{1}H HMQC of the Dipeptide β-Asp-Ala
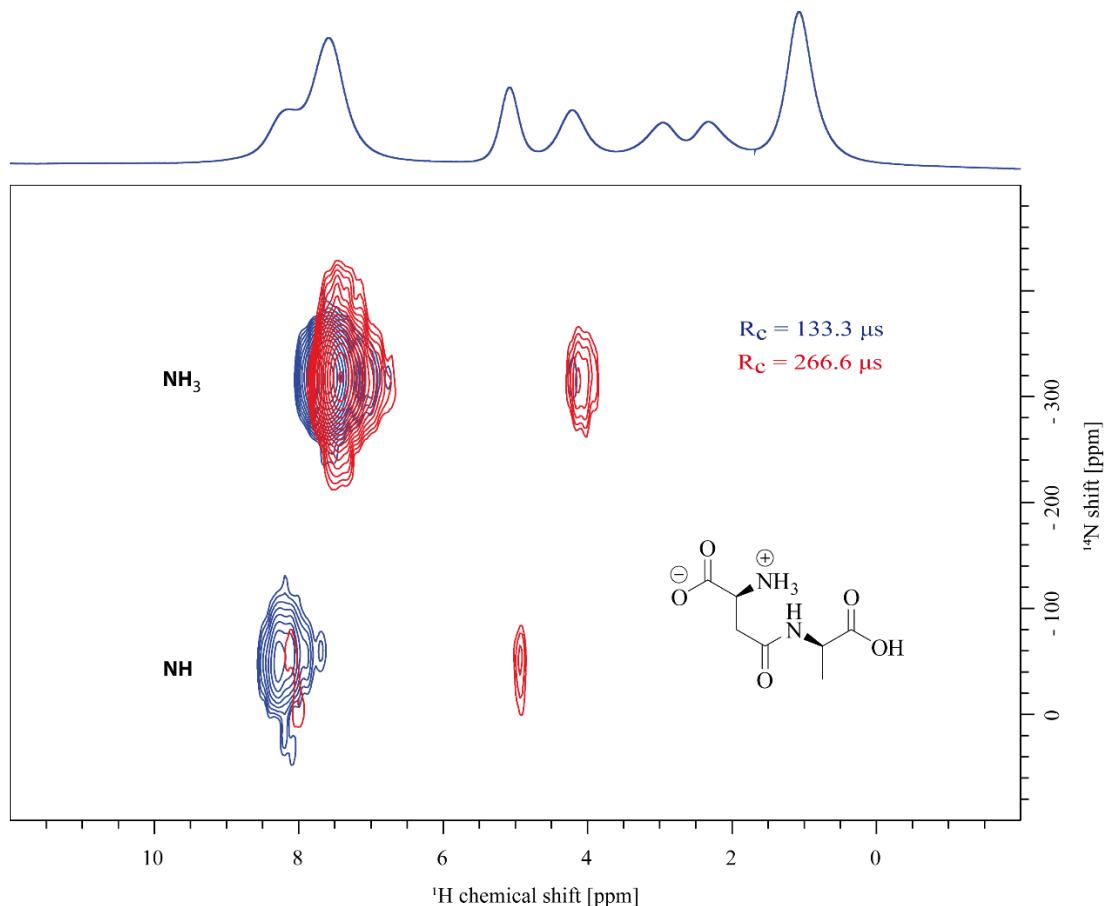
Figure S6: ^{14}N-^{1}H HMQC spectra recorded at 20 T and a MAS frequency of 60 kHz for the dipeptide β-AspAla using a recoupling time *(τ_{RCPL})* of $R_c = 133$ μs (blue) and $R_c = 266$ μs (red). 64 t_1 FIDs increments were acquired, each with 16 co-added transients and a recycle delay of 1.0 s. A ^{1}H one-pulse MAS NMR spectrum of β-AspAla is shown as external projection.

Figure S6 illustrates ^{14}N-^{1}H HMQC test measurements of the dipeptide β-Asp-Ala. By varying the recoupling time, it is possible to observe increasingly longer-range through-space proximities, e.g. longer recoupling times probing longer range intra- and intermolecular N···H proximities (see further investigations of this by Tatton et. al.[1]). Comparison of the red and blue spectra reveals that the increase in recoupling time yields additional N···H contacts and that the signal intensity of the directly bound NH decreases with increasing recoupling time.

SI 9: ^{14}N-^{1}H HMQC of amorphous PTX

PTX amorphous
R_C = 133.3 μs
R_C = 266.7 μs
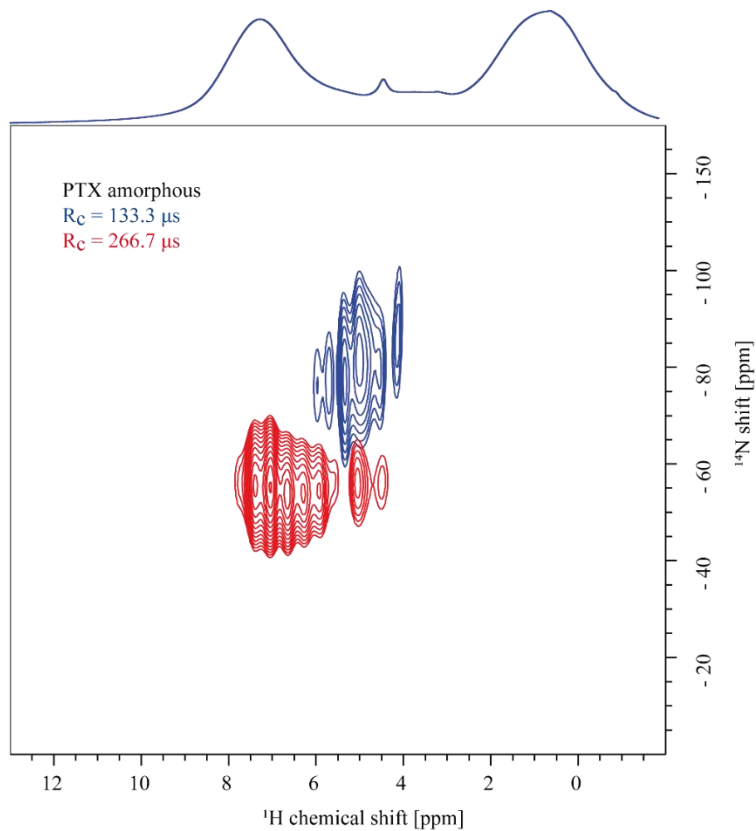
Figure S7: ^{14}N-^{1}H HMQC spectra recorded at 20 T and a MAS frequency of 60 kHz for amorphous paclitaxel using a recoupling time *(τ$_{RCPL}$)* of blue: $R_c = 133.3$ μ*s*, red: $R_c = 266.7$ μ*s*. 34 t_1 FIDs increments were acquired using a recycle delay of 2.0 s, each with 240 co-added transients resulting in an overall experimental time of 4 h 40 min. The corresponding ^{1}H one-pulse MAS NMR spectrum is shown as external projection.

SI 10: Crystal structure of PTX
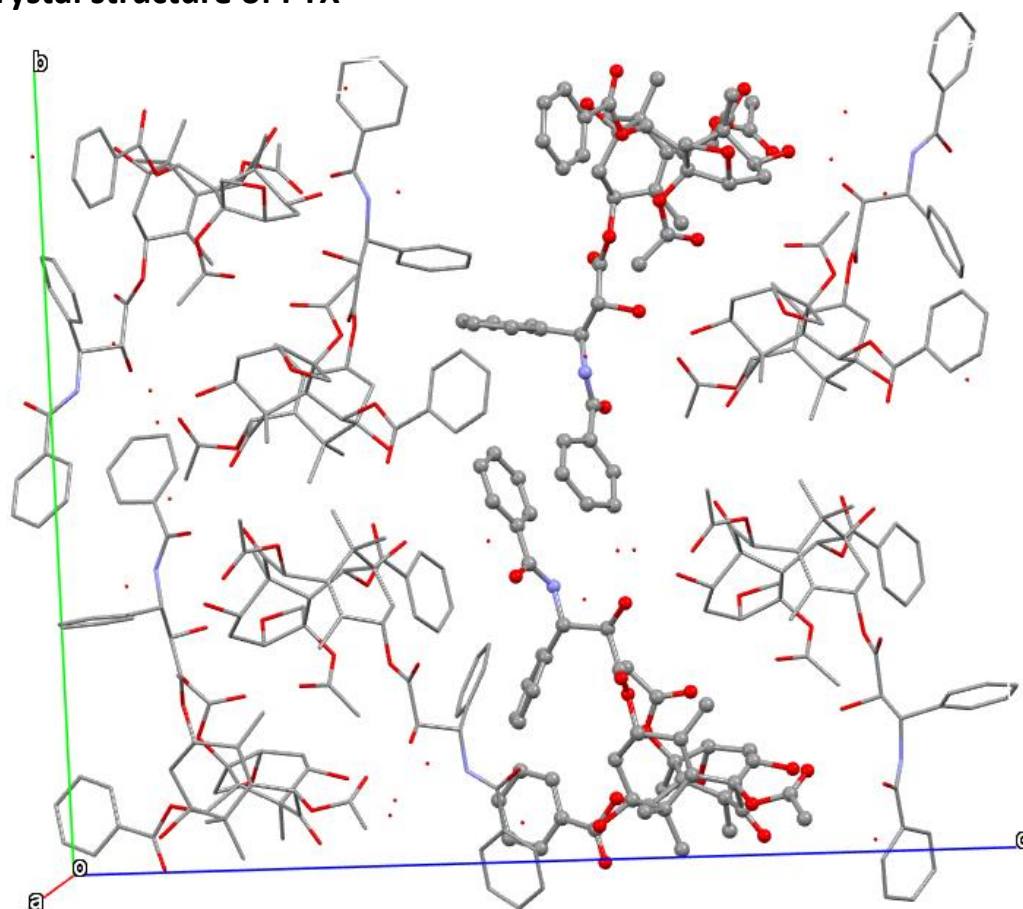
Figure S8: Unit cell of PTX. Hydrate structure of PTX published by Vella-Zarb et al.[7] with the CCDC name RIGKUP and CCDC number 912149. This structure contains two molecules of PTX in the asymmetric unit and six additional water molecules. The original structure was obtained by single-crystal synchrotron XRD data at a temperature of 120.15 K. The two individual PTX molecules in the asymmetric unit are highlighted above.

SI 11: References

1.   Tatton AS, Bradley JP, Iuga D, Brown SP. Z Phys Chem. 2012;**226(11-12)**,1187-204.
2.   Gan Z, Amoureux JP, Trebosc J. Chem Phys Lett. 2007;**435(1-3)**,163-9.
3.   Samoson A. Chem Phys Lett. 1985;**119(1)**,29-32.
4.   Brown SP. Chapter 2, High-resolution ^{1}H 2D Magic-angle Spinning Techniques for Organic Solids. Modern Methods in Solid-state NMR: A Practitioner's Guide: The Royal Society of Chemistry; 2018. p. 39-74.
5.   Luxenhofer R, Schulz A, Roques C, Li S, Bronich TK, Batrakova EV, et al. Biomaterials. 2010;**31(18)**,4972-9.
6.   Schulz A, Jaksch S, Schubel R, Wegener E, Di Z, Han Y, et al. ACS nano. 2014;**8(3)**,2686-96.
7.   Vella-Zarb L, Baisch U, Dinnebier RE. J Pharm Sci. 2013;**102(2)**,674-83.

Manuscript 2:

Insights into the loading-dependent assembly of poly(2-oxazoline) based paclitaxel formulations using solid-state NMR spectroscopy

Marvin Grüne[a], Stefanie Klisch[a], Michael Lübtow[b], Robert Luxenhofer[b], and Ann-Christin Pöppler[a]*

[a] Institute of Organic Chemistry, University of Würzburg, Am Hubland, 97074 Würzburg, Germany
[b] Lehrstuhl für Chemische Technologie der Materialsynthese, University of Würzburg, Röntgenring 11, 97070 Würzburg, Germany

Introduction

Approximately 40 % of the currently marketed drugs[1] and even up to 75 % of the compounds under development are poorly soluble in water.[2] A very well-known representative of this group is paclitaxel (PTX, **Schema 1**), which is one of the most important and relevant drugs to combat breast and ovarian cancer. The discoverer themselves published a detailed overview of the development of this drug over the several decades until the mid-1990s.[3] While its use for breast and ovarian cancers is already established, it is currently going through clinical trials for use against other cancers as well,[4] which is hampered by the limiting factor of its poor aqueous solubility. A combination of Cremophor El with dehydrated ethanol is used to administer the drug intravenously.[5] Since both of these substances are also pharmacologically active, additional clinical problems arise.[6]

One efficient way to overcome this solubility issue is the incorporation of the drug into polymer micelles which often results in higher solubility of the drug. Poly(2-oxazoline) (POx) micelles are of particular interest as they show low toxicity, high loading capacity and durability.[7] Poly(2-methyl-2-oxazoline)-*block*-poly(2-butyl-2-oxazoline)-*block*-poly(2-methyl-2-oxazoline) (POL) is a triblock copolymer of the ABA type with both the hydrophilic and hydrophobic repeating units featuring amide-groups (**Scheme 1**). The high loading capacity, particularly for polar drugs, may be due to the absence of hydrogen-bond donors in each repeating unit of the backbone which limits inter- and intra-molecular interaction between polymer chains and therefore favours the hydration of the polymer backbone.[7a, 8] Due to the short butyl groups in the hydrophobic block, the environment within the micelle remains relatively polar, possibly still providing good interactions with the polar groups of water insoluble drugs like PTX. Although it is only proved that micelles exist in their particular solvent, there are strong indications for micelles to exist in their solid-state form as well. For a similar system to the one investigated in this work, it has been shown that the micelles can be lyophilized and subsequently redispersed in water without a change in drug loading, particle size or the *in vitro* drug activity.[7a]

Schulz *et al.*[7b] examined the drug-induced morphology switch of an aqueous PTX/Poly(2-oxazoline) system. They have found that the replacement of the butyl side chain of this polymer by a much more hydrophobic nonyl group results in a loading of only half the capacity for PTX and lower stability of the system. Using SANS, DLS, and cryo-TEM, they observed that the investigated triblock copolymers partially form wormlike micelles in aqueous solution and loading with PTX leads to a morphology switch to exclusively spherical micelles. In addition, they report that an increasing PTX concentration results in the formation of PTX domains at the core-shell interface with a raspberry-like structure. Furthermore, Lübtow *et al.*[8b] investigated this polymer together with PTX and the natural product curcumin and found that a migration of a methylene group from the polymer side chain to the polymer main chain, forming a polymer of the class of poly(2-oxazine), leads to a strongly altered specific drug load. These two publications form the basis for the current study but did not investigate the interactions of POL and PTX in detail. Therefore, the goal of the present study is to gain insights into the local structure of such micelle-drug systems at an atomic level using NMR spectroscopy, complementary to the images obtained with cryo-TEM and SANS. The broadening caused by the strongly reduced mobility of encapsulated drugs within this system makes a characterization by NMR in solution impossible and therefore, solid-state NMR is used as the main experimental technique.[9] Furthermore, the success of such solid-state NMR studies on larger and more chemically complex substances could promote future NMR spectroscopic investigations due to their easier accessibility compared to SANS measurements and their complementary nature to diffraction based methods in general.

The complexity of the PTX molecules leads to pronounced overlapping of the NMR signals in the solid state (Manuscript 1: Crystalline PTX). The use of heteronuclear correlations reduces this complexity. In an earlier publication, Grüne *et al*. studied these amorphous drug-polymer formulations with the help of ^{14}N-^{1}H HMQC solid-state NMR.[9] These experiments yielded well-separated signals, which are spread over a large ^{14}N shift range, providing information on the symmetry of the nitrogen environments and probing ^{14}N-^{1}H through-space proximities. Those results represent a valuable puzzle piece containing information about ^{14}N and ^{1}H that helps to improve the structural understanding of PTX containing drug-polymer formulations at an atomic level.

The previous chapters were able to get structural information of the nitrogen environments by focussing on special measurements observing the nitrogen atoms in these systems. The chapter focusing on the investigation of crystalline PTX itself contains important results regarding the characterisation of the active ingredient by solid-state NMR as well as X-ray powder diffraction. In the current chapter, the mentioned results will be extended to obtain a more uniform model through the investigation of ^{13}C solid state NMR data of POL/PTX formulations with

different loadings. With the absence of quadrupolar broadening (as compared to ^{14}N) as well as weaker dipolar broadening and a larger chemical shift range than ^1H, this ^{13}C investigation promises further insights into the structural understanding of these paclitaxel loaded polymer micelles despite the complexity and significant spectral overlap observed for these data.
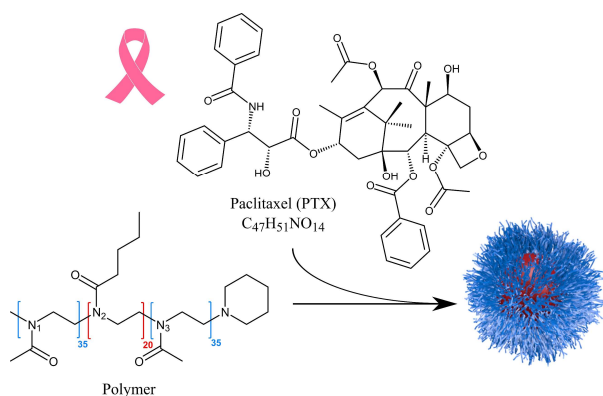
Scheme 1: Structural formulas of the components used in this study and schematic drawing of a micelle: The amphiphilic block copolymer poly(2-methyl-2-oxazoline)-block-poly(2-n-butyl-2-oxazoline)-block-poly(2-methyl-2-oxazoline) (POL) encapsulates paclitaxel (PTX) by self-assembly into polymeric micelles. Reprinted with the permission from ref.[9] Copyright 2020 Royal Society of Chemistry.

Experimental section

Materials

Paclitaxel in its crystalline form was purchased from LC Laboratories and used without further purification. The ABA triblock polymer poly(2-methyl-2-oxazoline)-block-poly(2-n-butyl-2-oxazoline)-block-poly(2-methyl-2-oxazoline) (POL) was synthesized according to previously published protocols.[8b] Subsequent preparation of differently loaded PTX-POL formulations also followed the literature known procedures.[7] Resulting drug loadings were determined using HPLC analysis.

Amorphous Paclitaxel (PTX)

Lyophilization was used to prepare amorphous paclitaxel. The ^{13}C solid-state NMR spectrum in **Figure 1** as well as PXRD measurements, shown in Grüne *et al.*[9], confirmed the amorphicity.

POL sample

The polymer POL itself as well as all the differently loaded formulations used in this work contain the same polymer. To compare the spectra of POL to those of the formulations, pure POL was heated above its T_g (T_g(POL) = 56 °C)[10]. After this treatment, POL shows narrower, more defined peaks (**Figure S1**), comparable to those seen in the formulations.

PTX-Polymer Formulations

Throughout this manuscript, the formulations are referred to as POL-2-PTX, POL-4-PTX and POL-9-PTX. The numbers 2, 4 and 9 describe the composition of the formulations according to **Table 1**. The different concentrations used for preparation and the median hydrodynamic radius[7b] of the micelles, determined by DLS, are listed in **Table 1** as well.

Table 1: Formulations, compositions, concentrations used for preparation and median hydrodynamic radii of the micelles.

Formulation	Ratio (POL/PTX) (w/w)	wt% PTX	mol% PTX to monomer units of POL	Solubilized concentration POL (g/L)	Solubilized concentration PTX (g/L)	Median Hydro-dynamic Radius (R_h)[7b]
POL-2-PTX	10:2	17	2.2	10 g/L	2 g/L	6 nm
POL-4-PTX	10:4	29	4.5	10 g/L	4 g/L	8 nm
POL-9-PTX	10:9	47	10.1	10 g/L	9 g/L	11 nm

All three formulations were produced by combining the appropriate amount of ethanolic polymer and PTX solutions. Ethanol was then evaporated, the resulting thin film dissolved in H_2O and lyophilized to give a white powder.

NMR

The ^{13}C NMR data were measured with a Bruker Avance III HD 600 MHz (14.1 T) spectrometer and a 3.2 mm double-channel (^{15}N-^{31}P/^{1}H-^{19}F) MAS probe. The duration of the 90° ^{1}H pulses was 2.50 µs in the ^{13}C CP MAS with ramped cross-polarization conditions optimized with α-glycine using a ramp from 90 % to 100 % with 100 increments and a contact time of 2.5 ms. SPINAL-64[11] heteronuclear decoupling was applied during an acquisition period of 23 ms at a ^{1}H *rf* nutation frequency of 100 kHz, with an optimized 180° pulse length of 4.8-5.1 µs. KBr was used for magic angle calibration. ^{13}C Chemical shifts were referenced to the methylene carbon signal of adamantane at 38.48 ppm.[12] All ^{13}C direct excitation spectra were obtained with a 90° ^{13}C pulse duration of 4.0 µs. The temperature of the probe was regulated to 296.4 K corresponding to a calibrated temperature of 340 K of the sample for 24 kHz MAS spinning rate and to 324 K for 20 kHz. The additional warming is the result of frictional heating due to

MAS. Further information about the temperature calibration for this specific 3.2 mm probe can be found in "Manuscript 1: Crystalline PTX" of this dissertation.

In addition, a ^{1}H(SQ)-^{1}H(DQ) BABA spectrum obtained at 700 MHz/16.4 T with a 0.7 mm MAS probe (chapter **SI 2**) was recorded to obtain information about the spatial proximity of the protons. Furthermore, a ^{1}H-^{13}C HETCOR spectrum obtained at 600 MHz/14.1 T with the 3.2 mm MAS probe described above (chapter **SI 3**) was measured to investigate spatial proximities between POL and PTX.

Results
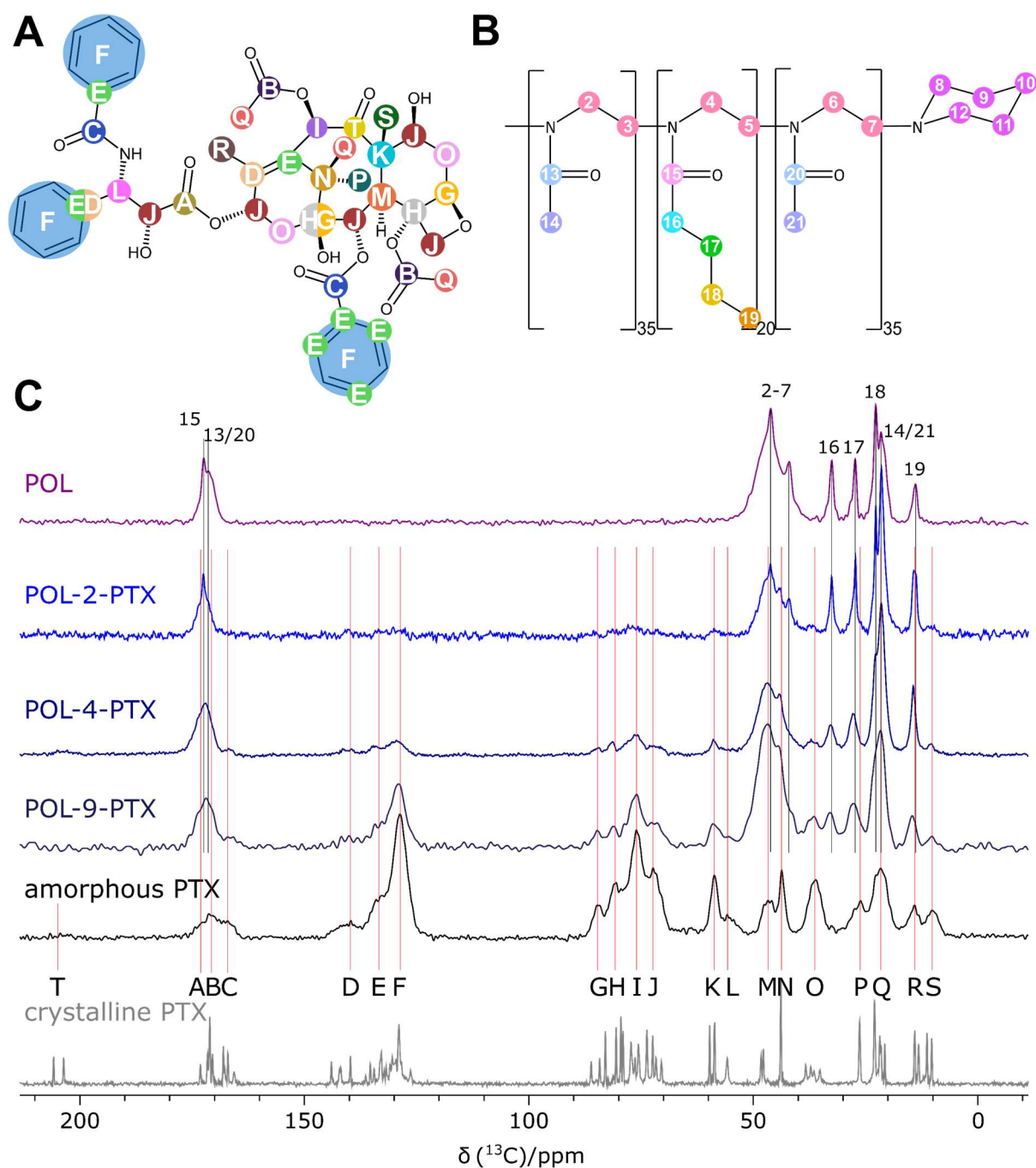
Figure 1A: PTX signal regions labeled in Figure 1C, related to the chemical structure of PTX.

Figure 1B: POL peaks labeled in Figure 1C, assigned to the chemical structure of POL.

Figure 1C: ^{13}C CP MAS NMR spectra of the pure polymer POL (purple), three different formulations POL-2-PTX, POL-4-PTX, POL-9-PTX (different shades of blue), amorphous PTX (black), and crystalline PTX (grey). Partial assignment of relevant peak areas for the discussion is indicated with numbers belonging to POL signals and capital letters to PTX peak areas. All spectra were recorded at 14.1 T and 24 kHz MAS spinning rate (except for POL-9-PTX at 20 kHz) with a contact time of 2.5 ms and the following parameters (co-added transients/recycle delay): 2889/2.0 s (POL), 4096/2.0 s (POL-2-PTX), 10240/2.0 s (POL-4-PTX), 1024/3.0 s (POL-9-PTX), 23532/2.5 s (amorphous PTX) and 1756/2.5 s (crystalline PTX). The line broadening is set to 30 Hz for each spectrum except for crystalline PTX (0 Hz).

This work focuses on the ^{13}C solid-state MAS NMR investigation of the three differently loaded formulations containing 17 wt% (POL-2-PTX), 29 wt% (POL-4-PTX) and 47 wt% (POL-9-PTX) PTX, especially on ^{13}C CP MAS data (**Figure 1**). Chapters **SI 4** and **SI 5** summarize the results of the ^{1}H and ^{13}C NMR characterization of pure POL and pure PTX in solution. For the investigated system, the detection of interactions via dipolar couplings between protons is hampered by a strong broadening of the signals which is shown in some additional ^{1}H data (^{1}H(DQ)-^{1}H(SQ) BABA MAS and ^{1}H-^{13}C HETCOR MAS) of exemplary samples in **Figures S2** and **S3**. This broadening of the ^{1}H signals in the formulations prevents a closer investigation of this complex system regarding distinct proton interaction. For amorphous PTX (existing in the formulations), an assignment of carbon nuclei to the corresponding peaks is difficult due to spectral overlap of the signals (**Figure 1C**) which results in a decrease of the total peak number from 55 resolved signals in the ^{13}C CP MAS spectrum of crystalline PTX to 19 distinguishable signals for amorphous PTX. Therefore, PTX signals are grouped into the peak regions visible in the ^{13}C CP MAS spectrum of crystalline PTX and named using capital letters as summarized in **Figure 1A**. The assignments themselves are based on the work in "Manuscript 1: Crystalline PTX". Each peak includes a certain number of signals that, if addressed in the specific discussions, are indicated in the chemical structure of PTX. **Figure 1** also shows the numbers of the carbon atoms of the chemical structure of POL assigned to the peaks in the ^{13}C CP MAS spectrum. For better visibility of the aliphatic region for further investigation, an enlarged section of the range from 0 to 65 ppm of the spectra of **Figure 1** is shown in **Figure S8.**

Changes of chemical shift for PTX signals

Since some peaks visible in the formulations are made up of PTX and POL signals of similar chemical shift, peaks that can be analyzed with regard to changes in chemical shift should be those consisting of only PTX or POL. For amorphous PTX, such signals correspond to aromatic, alcohol, and ether carbon atoms between 160 and 55 ppm and two additional peaks at 37 and 11 ppm (**Figures 1** and **S8**). These chemical shifts are listed in **Table S1** and plotted in **Figure 2A.**
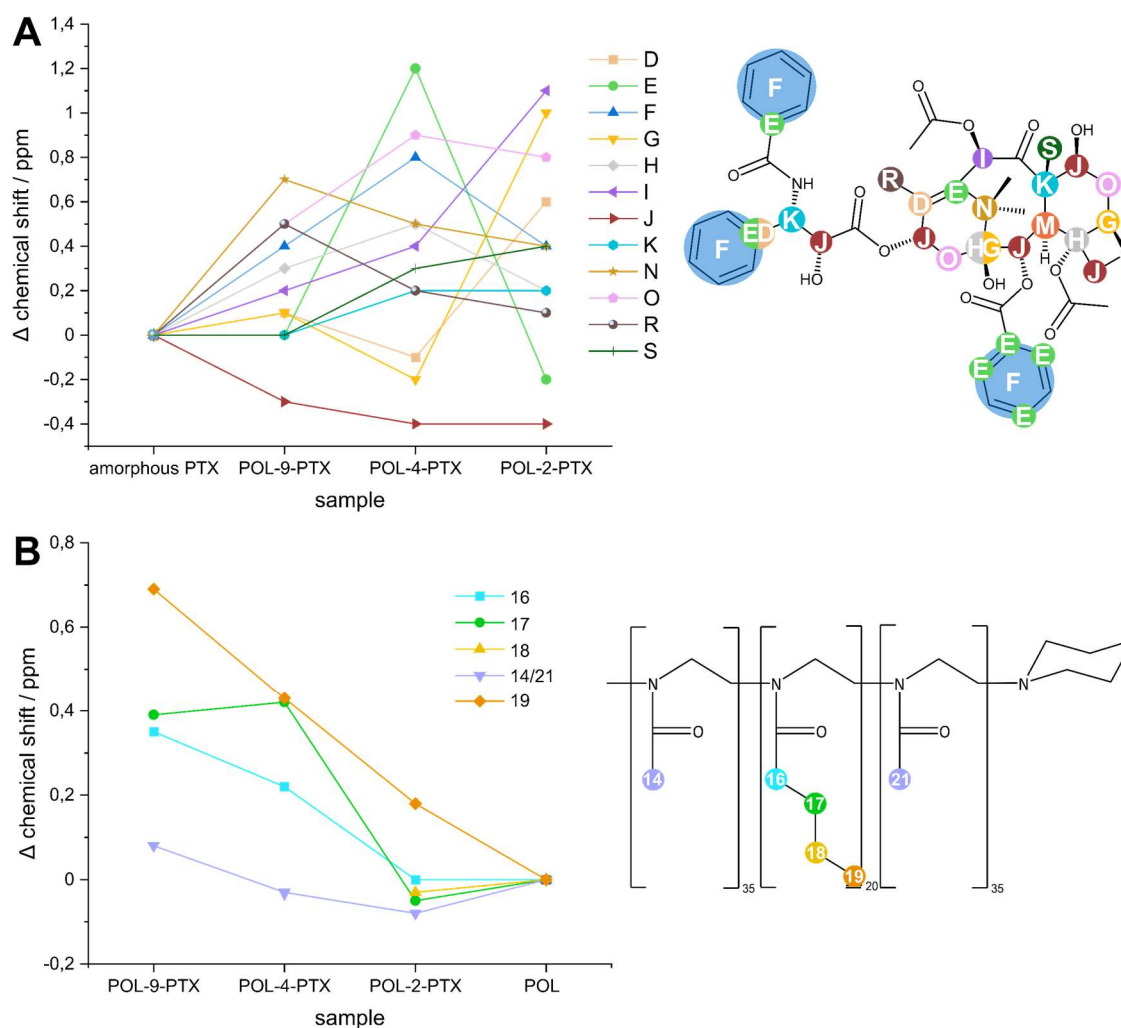
Figure 2A: Left) Change of ^{13}C chemical shifts (ppm) of the PTX peak regions starting from amorphous PTX as reference. Related ^{13}C signal regions are assigned in the spectra of Figure 1. **Right)** PTX carbon atoms displayed in Figure 2A left.

Figure 2B: Left) Change of chemical shifts (ppm) of the POL peak regions starting from amorphous POL as reference. Related ^{13}C signals are assigned in the spectra of Figure 1. **Right)** POL carbon atoms displayed in Figure 2B left.

Peak J belonging to carbon atoms adjacent to OH- or OR-groups changes to a lower chemical shift between amorphous PTX and POL-9-PTX and continues this tendency between POL-9-PTX and POL-4-PTX whereas it does not change from POL-4-PTX to POL-2-PTX. Overall, it is the only signal with continuously decreasing chemical shift. All atoms assigned to signal area J are directly bound to an oxygen. As shown by Grüne *et al.*[9] for this system and Pöppler *et al.*[13] for a similar system, OH groups of PTX likely act as hydrogen bond donors, as shown for interactions of OH of the PTX to amide groups of POL or within PTX. Signals D, G, I, and O show the largest shift change resulting from the establishment of the micellar environment (PTX to POL-2-PTX), all shift to positive ppm values and all are part of the baccatin core. Interestingly, peak E shows a strong increase of chemical shift by reducing the drug loading from POL-9-PTX to POL-4-PTX and an even larger decrease from POL-4-PTX to POL-2-PTX. This signal experiences a comparably small overall shift change (as compared to amorphous

PTX) upon formation of the micelle. Peak F shows the same tendency, but less pronounced. One difference between signals E and F is the overall shift change by forming a micelle (POL-2-PTX): The chemical shift of E decreases and that of F increases as compared to pure amorphous PTX. Both signals E and F correspond to aromatic groups which may be likely to react to the change in the amount of PTX molecules due to effects such as π-stacking. In the formulation POL-4-PTX, the peaks E, F, H, N, and O show the highest shift changes as compared to amorphous PTX. The carbon assigned to peak H is bound to oxygen and that of signal O is situated in the periphery of the baccatin core.

Changes of chemical shift for POL signals

The same approach is now applied to the polymer. The evaluated ^{13}C chemical shifts of POL are listed in **Table S2** and plotted in **Figure 2B.** Peak 16 is the only POL signal that does not also contain a PTX signal contribution in the formulations. However, if one focuses on the POL-only peak 16 as well as peak 17 which only contains a small contribution from PTX, it can be seen that only an increase of the drug loading affects the chemical shift whereas the peaks remain unshifted by introducing a small amount of PTX. POL is expected to behave differently as compared to the previous evaluation of the change of PTX chemical shifts (**Figure 2**). Amorphous PTX incorporated into the micelle with lowest drug loading to POL-2-PTX results in a new micellar environment[7b] and thus to distinct structural changes for the amorphous PTX. On the other hand, pure POL already forms micelles without any incorporated PTX. Therefore, the initial addition of PTX is not expected to change as much in the environment of POL and vice versa. This is confirmed by the observed behaviour of the change in chemical shifts of the POL peaks 16 and 17.

Signal 18 is excluded for investigation of POL-4-PTX and POL-9-PTX due to the large overlap (**Figures 1** and **S8**)**.** Signal 19 of POL strongly overlaps with peak R of PTX (**Figures 1** and **S8**). Since POL-2-PTX only contains 2.2 mol% PTX per monomeric unit of the POL (**Table 1**), resulting in 9.9 mol% PTX per unit of block B of POL, a correspondingly small contribution of this overlapping signal has to be attributed to the carbon atoms R (PTX) compared to 19 (POL). Therefore, this peak 19/R is mainly dominated by the POL 19 signal. As the chemical shift of this envelope changes to values higher than the pure PTX peak and the pure POL signal, it can be concluded that there is strong interaction in this region of the polymer, changing with different drug loading.

With increasing PTX loading, the peaks belonging to the butyl chain show more pronounced chemical shift changes and thus changes in the local environment than the more hydrophilic carbon atoms 14/21 whose changes are smaller than 0.1 ppm throughout the compositions. During the establishment of the micellar environment, 16, 17, and 19 show similar trends in

chemical shift towards higher ppm values. However, while the chemical shifts of 16 and 17 are less influenced by a low loading as compared to a medium and high PTX content (the shift change of 18 from POL to POL-2-PTX is negligible as well), 19 does show a linear increase already from a low amount of incorporated PTX through the different steps of loading.

Mobility Aspects – ^{13}C direct excitation spectra

In addition to the dependence of the chemical shifts on the composition of the formulation, changes of the line widths (Full-Width-Half-Maximum, FWHM) as well as of the intensities in ^{13}C CP MAS spectra can give additional information about changes in the local environment of specific sites on the PTX and POL molecules. However, the change of the intensities depends on different variables. On the one hand – the preferred variable for evaluating possible interaction – it scales with the strength of the dipolar interactions of protons in spatial proximity. The other aspect is the influence of the mobility on the intensity, a higher mobility decreases the efficiency of the ^{1}H-^{13}C magnetisation transfer during CP and thus affects the peak intensity.[14] Furthermore, the spin-lattice relaxation times T_1 depend on the mobility as well.[15] To exclude the CP efficiency as a reason for intensity changes, ^{13}C direct excitation MAS spectra with a 90° excitation pulse and a short recycle delay of 0.8 s were recorded (**Figure S9**). In this type of spectra, the ^{13}C spin-lattice relaxation times T_1 are the main factor determining the signal intensity. The results can be summarized as follows: The carbonyl functions 15 and 13/20 of POL as well as A, B, and C of PTX are barely visible or not detectable, respectively. This can be attributed to long relaxation times T_1 as the carbonyl carbons are not attached to any protons or to low mobility of these carbons. Peaks in the ^{13}C direct excitation spectrum of POL are clearly visible for the mobile side chains at shifts below 50 ppm. The relative intensities of these signals change only insignificantly upon PTX loading. At the same time, the expected gradual increase of PTX peaks due to a higher PTX content can be recognized. Thus, it can be concluded that there is only a small change in mobility with increasing loading and therefore this has only a small effect on the intensities of the ^{13}C CP MAS spectra.

Changes of ^{13}C line widths

In this subchapter, the changes of the FWHM of the individual peaks of the investigated ^{13}C CP MAS spectra are evaluated (see chapter **SI 8** for peak fitting). Changes in interactions which correspond to the same chemical environment visible by a common peak can average out themselves which increases the complexity of the evaluation. **Figure 3** shows the change of the absolute FWHM of the different signals of PTX and POL with the composition of the formulation. For POL, only the aliphatic signals 14/21, 16, 17, and 18 of the sidechains were
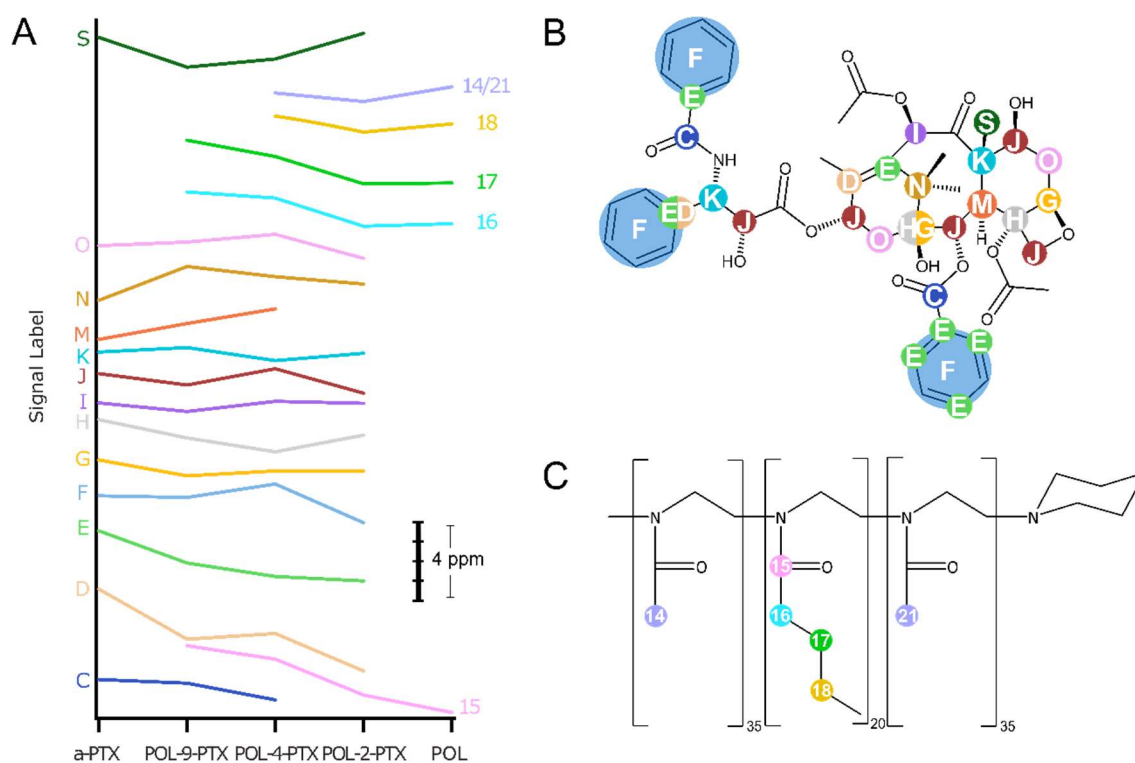
Figure 3A: Change of FWHM of PTX as well as POL signals with the composition of the formulation. a-PTX stands for amorphous PTX. Related ^{13}C signals are assigned in Figure 1.
Figure 3B: PTX carbon atoms displayed in Figure 3A.
Figure 3C: POL carbon atoms displayed in Figure 3A.

investigated. Due to the low molar proportion of PTX in the formulations (**Table 1**), the influence of PTX signal contributions on the POL data of Figure 3 is negligible. For all its remaining signals, deconvolution is not meaningful due to overlap with other signals, what is also found for peaks 18 and 14/21 of POL-9-PTX. Strong signal overlap is additionally observed for the PTX signals A, B, M, N, P, Q, and R.

For POL, all investigated peaks show the lowest FWHM in the POL-2-PTX formulation, rather than in pure POL. As a general trend, the FHWM of signals belonging to POL enlarges with increasing PTX load. All polymer carbon atoms seem to be affected by the presence of PTX in a similar magnitude. With a FWHM of 129 Hz, 132 Hz, and 114 Hz, the line widths of peaks 16, 17, and 18 of the POL-2-PTX formulation are comparably low which suggests higher mobility or an increased degree of order for these carbons. In pure POL, the same peaks show a FWHM of 147 Hz, 138 Hz and 177 Hz, respectively. The largest change from pure POL to formulation is observed for 18, the CH_2 group with the largest distance from the carbonyl function. The decrease in FWHM of the polymer signals from POL to POL-2-PTX can be attributed to the finding of Schulz *et al.*[7b] that after incorporation of PTX, the number of spherical micelles increases and the proportion of worm-like micelles decreases. Furthermore, the thermodynamic driving forces increase for higher loading which leads to a more pronounced separation

of the hydrophilic and hydrophobic parts of POL. Altogether, this results in an increased order. The subsequent enhancement in FWHM of these signals with increasing drug loading indicates that the hydrophobic butyl chain containing 16 through 18 and the hydrophilic side chain containing the methyl groups 14/21 are possible sites of interaction between PTX and the POL micelle.

On the opposite end of the composition, half of the PTX peaks (5 out of 11) display the highest FWHM in pure amorphous PTX. In contrast to POL, the PTX peaks do not reveal a common change throughout the differently loaded formulations. However, it is noticeable that 5 out of 11 PTX signals show their lowest value at POL-2-PTX, corresponding to the lowest amount of amorphous PTX in the investigated formulations.

Discussion and conclusion

Solid-state NMR investigation of the complex polymer-drug formulations in the present study could show their amorphicity as well as significant spectral changes as compared to the pure materials POL and PTX. This demonstrates the possibility to study interactions even for such complex systems by this approach.
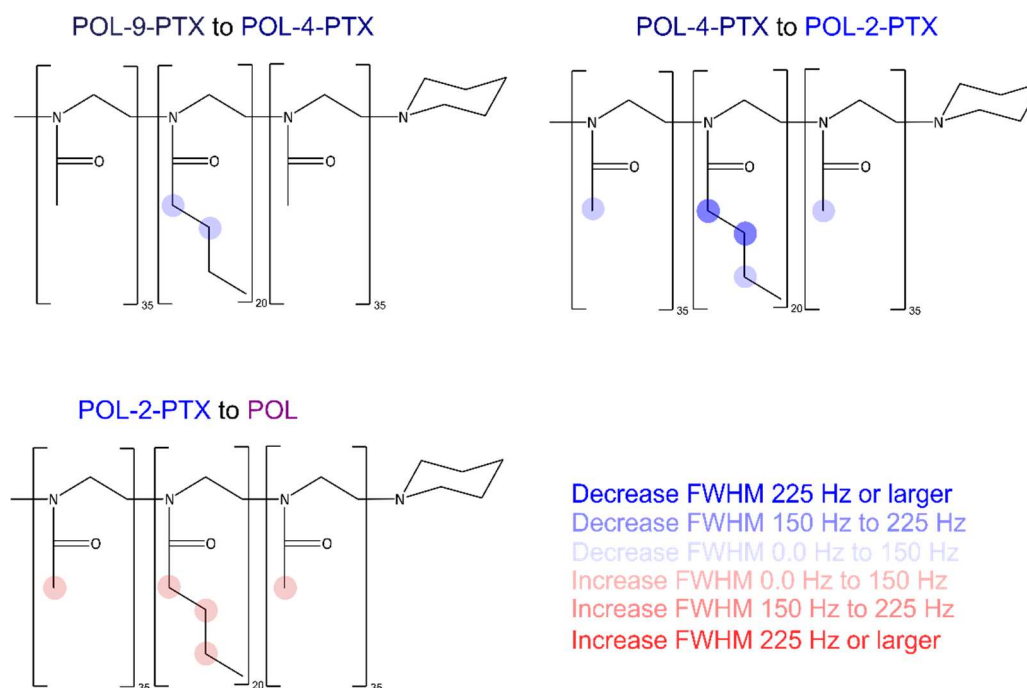

Figure 4: Size of changes in FWHM for chosen POL peaks. From POL-9-PTX to POL-4-PTX, the decrease in FWHM for all visible POL peaks lies between 150 Hz and 225 Hz. From POL-4-PTX to POL-2-PTX, decreases in FWHM start from 0 Hz and reach a value above 225 Hz. From POL-2-PTX to POL, all peaks increase in FWHM by a value below 150 Hz.
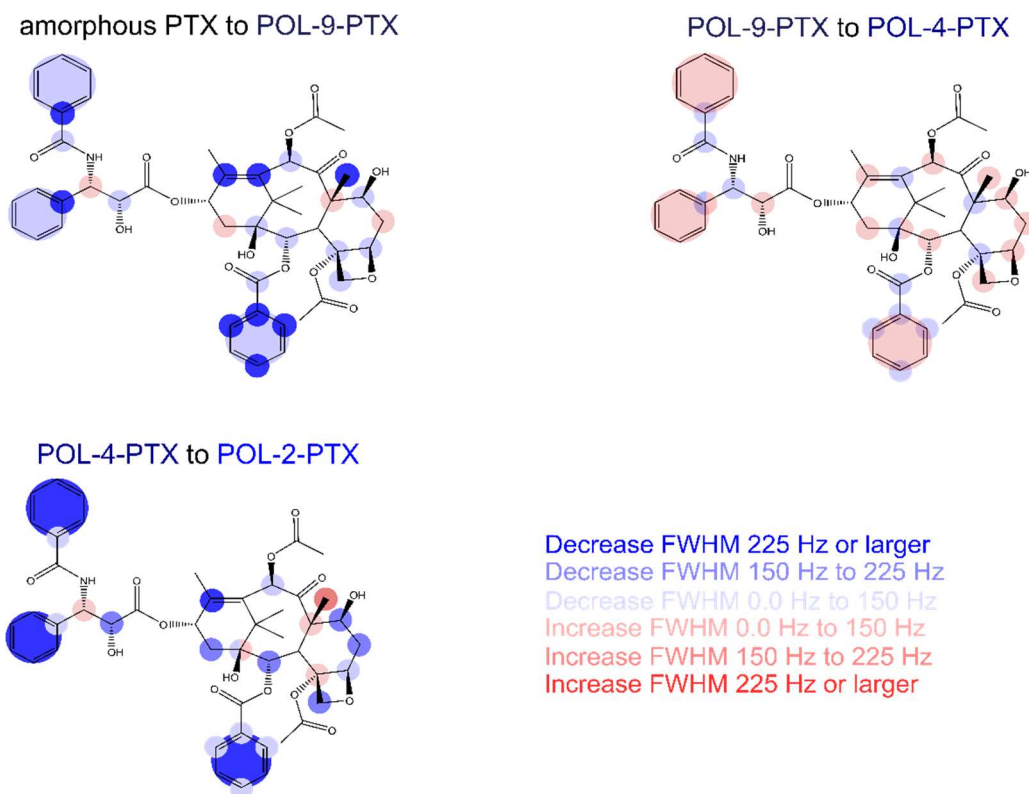
Figure 5: Size of changes in FWHM for all chosen PTX peaks. From amorphous PTX to POL-9-PTX, most peaks show a decrease in FWHM. From POL-9-PTX to POL-4-PTX, about half of the chosen peaks increase in FWHM while the other half decrease. From POL-4-PTX to POL-2-PTX, most peaks decrease in FWHM.

Figures 4 and **5** illustrate the investigated changes in FWHM for POL and PTX throughout the different compositions. One can assume that a change of FWHM results from interaction between PTX and POL leading to a modified distribution of ^{13}C environments and thus also of ^{13}C chemical shifts because not all PTX molecules present in the amorphous formulation are supposed to interact with POL in the same way. The information available from changes of chemical shift and of FWHM with the composition of the formulation can now be combined to determine possible sites of interaction in PTX. Peaks D through G show the largest alterations of chemical shift as a consequence to changes in drug load. Similarly, the dependence of FWHM on the composition of the formulation is largest for peaks D to F. Both results together suggest interactions between POL and PTX for these mainly aromatic carbons. For the ^{13}C POL signals, the FWHM along the butyl chain and of the methyl groups 14/21 generally enlarge with increasing drug loading in a similar magnitude, thus corroborating the increased interactions discussed above.

Therefore, the terminal phenyl groups of PTX seem to be most involved in interaction by the establishment of the micelle in POL-2-PTX and they are likely to react to the change in the amount of PTX molecules as well. The reason for this can be effects such as π-stacking.[9]

Schulz *et al.*[7b] used DLS, AFM, cryo-TEM, and SANS techniques for the investigation of this system. SANS data revealed a raspberry-like structure of the loaded micelles instead of homogeneous spheres. But nevertheless, as all the mentioned techniques, SANS also cannot look "into the micelles". The data of Schulz *et al.*[7] may be extended to an atomic level by the results of the present solid-state NMR study in the following way: The interactions observed between PTX and POL (in particular from changes of chemical shifts and FWHM of both POL and PTX ^{13}C signals) support the incorporation of PTX in the region of the core-shell interface determined from SANS data and specific sites of interaction can be specified. The experimental result that the ^{13}C chemical shift changes of the POL butyl group increase in the order 19 $\rightarrow$ 17 $\rightarrow$ 16 (signal 18 could not be evaluated due to signal overlap) with increasing PTX load whereas the ^{13}C chemical shifts of the methyl groups 14 and 21 are nearly independent of drug loading is consistent with the following model: For the lowest PTX content (POL-2-PTX), PTX is mainly located in the inner part of the micelles as they only interact with the final methyl groups 19 of the hydrophobic block B but neither significantly to the methylene groups of the butyl unit nor to the methyl groups of the hydrophilic blocks A. Upon further increasing of the loading, the PTX progressively extends towards the outer part of the micelle indicated by the increased interactions with the CH_2 carbons of the butyl chains (^{13}C chemical shift changes) proceeding versus the polymer backbone. In the context of this model, one has to keep in mind that even a single PTX molecule is much larger than the length of a butyl side chain. Therefore, the solid-state NMR results indicate that in fact the PTX molecules start to locate in the middle of the micelle for lowest loading and, due to their molecular size, they partially reach the surface of the micelle. This result is supported both by the small influence of the PTX on the methyl side chain and by the DLS and SANS data of Schulz *et al.*[7b] Their DLS results reveal a diameter of the micelles of 6 nm for POL-2-PTX and their SANS data show PTX clusters at the core-shell in regions A (containing the acetyl side chains) of the ABA block polymer already for POL-2-PTX becoming more pronounced with increasing PTX load.

In an earlier publication by Grüne *et al.*[9], complementary results were obtained by ^{14}N-^{1}H HMQC spectra that support the current model: Measurements of N-H proximities had shown interactions between the amide nitrogen of the polymer and NH and OH groups of PTX for POL-4-PTX. In the mentioned investigation, this contact could not be excluded for POL-2-PTX as well but was very unlikely to be detected due to the low PTX content. Additionally, the results indicated a more symmetric nitrogen environment upon increasing PTX loading, visible by a decreasing quadrupolar shift of these amide nitrogens which can be explained by a transformation of the trigonal planar coordination of the amide nitrogens in pure POL towards a tetrahedral environment upon the addition of PTX. This can be induced by the formation of hydrogen bonds between the amide nitrogens and OH groups of PTX and supports the model of a

PTX loading from the inner towards the outer part of the micelle.

In conclusion, the present study shows how structural information of very complex drug-polymer systems can be obtained at an atomic level by solid-state NMR. The latter thus represents a complementary experimental method to SANS, cryo-TEM and AFM. In addition, solid-state NMR instrumentation is much more and easier accessible than SANS or TEM equipment. Due to the huge size of the examined drug-polymer complex, it is furthermore concluded that solid-state NMR can be used as a basis for investigations on other pharmaceutical formulations. For other drugs or excipients, this technique might therefore even be able to give further insights on loading models if the limitations by broad NMR signals due to the amorphicity of the samples are reduced.

References

[1]   S. Kalepu, V. Nekkanti, *Acta Pharm. Sin. B* **2015**, *5*, 442-453.

[2]   M. Rodriguez-Aller, D. Guillarme, J.-L. Veuthey, R. Gurny, *J. Drug Delivery Sci. Technol.* **2015**, *30*, 342-351.

[3]   M. E. Wall, M. C. Wani, *J. Ethnopharmacol.* **1996**, *51*, 239-254.

[4]   a) R. T. Liggins, W. Hunter, H. M. Burt, *J. Pharm. Sci.* **1997**, *86*, 1458-1463; b) L. Mu, S. Feng, *J. Controlled Release* **2001**, *76*, 239-254; c) R. Cavalli, O. Caputo, M. R. Gasco, *Eur. J. Pharm. Sci.* **2000**, *10*, 305-309.

[5]   S. Nobili, D. Lippi, E. Witort, M. Donnini, L. Bausi, E. Mini, S. Capaccioli, *Pharmacol. Res.* **2009**, *59*, 365-378.

[6]   L. Vella-Zarb, U. Baisch, R. E. Dinnebier, *J. Pharm. Sci.* **2013**, *102*, 674-683.

[7]   a) R. Luxenhofer, A. Schulz, C. Roques, S. Li, T. K. Bronich, E. V. Batrakova, R. Jordan, A. V. Kabanov, *Biomaterials* **2010**, *31*, 4972-4979; b) A. Schulz, S. Jaksch, R. Schubel, E. Wegener, Z. Di, Y. Han, A. Meister, J. Kressler, A. V. Kabanov, R. Luxenhofer, *ACS nano* **2014**, *8*, 2686-2696.

[8]   a) R. Hoogenboom, H. M. Thijs, D. Wouters, S. Hoeppener, U. S. Schubert, *Soft Matter* **2008**, *4*, 103-107; b) M. M. Lübtow, L. Hahn, M. S. Haider, R. Luxenhofer, *J. Am. Chem. Soc.* **2017**, *139*, 10980-10983.

[9]   M. Grüne, R. Luxenhofer, D. Iuga, S. P. Brown, A.-C. Pöppler, *J. Mater. Chem. B* **2020**, *8*, 6827-6836.

[10]   M. M. Lübtow, M. S. Haider, M. Kirsch, S. Klisch, R. Luxenhofer, *Biomacromolecules* **2019**, *20*, 3041-3056.

[11]   B. M. Fung, A. K. Khitrin, K. Ermolaev, *J. Magn. Reson.* **1999**, *142*, 97-101.

[12]   C. R. Morcombe, K. W. Zilm, *J. Magn. Reson.* **2003**, *162*, 479-486.

[13]   A. C. Pöppler, M. M. Lübtow, J. Schlauersbach, J. Wiest, L. Meinel, R. Luxenhofer, *Angew. Chem. Int. Ed.* **2019**, *58*, 18540-18546.

[14]   W. Kolodziejski, J. Klinowski, *Chem. Rev.* **2002**, *102*, 613-628.

[15]   N. Bloembergen, E. M. Purcell, R. V. Pound, *Phys. Rev.* **1948**, *73*, 679.

Supporting Information

Insights into the loading-dependent assembly of poly(2-oxazoline) based paclitaxel formulations using solid-state NMR spectroscopy

Marvin Grüne[a], Stefanie Klisch[a], Michael Lübtow[b], Robert Luxenhofer[b], and Ann-Christin Pöppler*[a]

[a] *Institute of Organic Chemistry, University of Würzburg, Am Hubland, 97074 Würzburg, Germany*
[b] *Lehrstuhl für Chemische Technologie der Materialsynthese, University of Würzburg, Röntgenring 11, 97070 Würzburg, Germany*

Supporting Information

Content:

SI 1: Comparison of POL above and below T$_g$

Figure S1: Comparison of ^{13}C-CP MAS as well as ^{13}C-direct excitation spectra before (green) and after (purple) heating the POL sample above its T$_g$. The spectra were recorded at 14.1 T and 24 kHz MAS. For the ^{13}C CP MAS data, 2k and 2889 transients were added to yield the final spectrum for POL before and after heating to T$_g$, respectively. For the ^{13}C direct excitation spectra, 2k and 9k scans were added to yield the final spectrum for POL before and after heating to T$_g$, respectively. The resulting spectra for all samples were processed with a line broadening value of 30 Hz.

SI 2: ^{1}H(SQ)-^{1}H(DQ) BABA MAS spectrum of POL-9-PTX
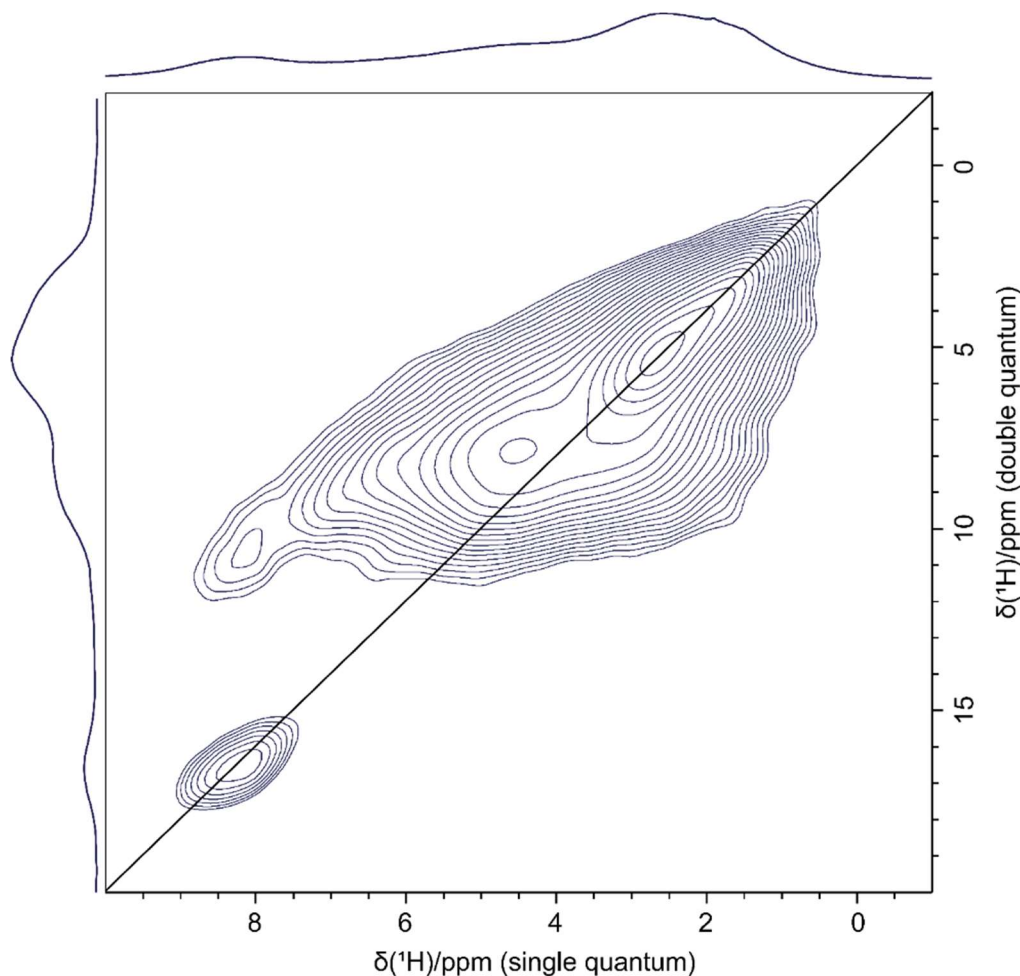
Figure S2: ^{1}H(SQ)-^{1}H(DQ) BABA MAS NMR spectrum of POL-9-PTX (diagonal line indicates the F_1 = $2F_2$ DQ-SQ diagonal) recorded with a 0.7 mm double-channel BB/^{1}H MAS probe at 16.4 T and a MAS frequency of 70 kHz using one rotor period of BABA recoupling. 180 t_1 FID increments were acquired using a recycle delay of 1.52 s, each with 16 co-added transients. The corresponding ^{1}H one-pulse MAS spectrum at 70 kHz is shown as external F2 projection. F1 projection illustrates the internal projection of this spectrum.

Figure S2 shows an ^{1}H(DQ)-^{1}H(SQ) BABA MAS NMR spectrum of an exemplary formulation, in this case POL-9-PTX. "Manuscript 1: Crystalline PTX" about the investigation of the single component crystalline PTX shows the same kind of 2D spectrum at 100 kHz MAS frequency. While the line widths steadily decrease with increasing MAS frequency for crystalline PTX up to 100 kHz spinning rate, no further narrowing is observed for POL-9-PTX upon increasing the spinning frequency above 60 kHz. This result shows that the distribution of environments and thus of ^{1}H chemical shifts in the amorphous formulation is the limiting factor of line narrowing with increasing MAS spinning rate.

SI 3: ^{1}H-^{13}C HETCOR MAS spectra of POL-9-PTX

Figure S3 shows a ^{1}H-^{13}C HETOR MAS spectrum of POL-9-PTX with $50\,\mu s$ contact time (top) and with $5000\,\mu s$ contact time (bottom). The signal highlighted in red shows with a high probability a proximity of either an amide of POL to aromatic protons of PTX or an intramolecular proximity of ester or amide in PTX to aromatic protons. This shows again the complexity of the system.
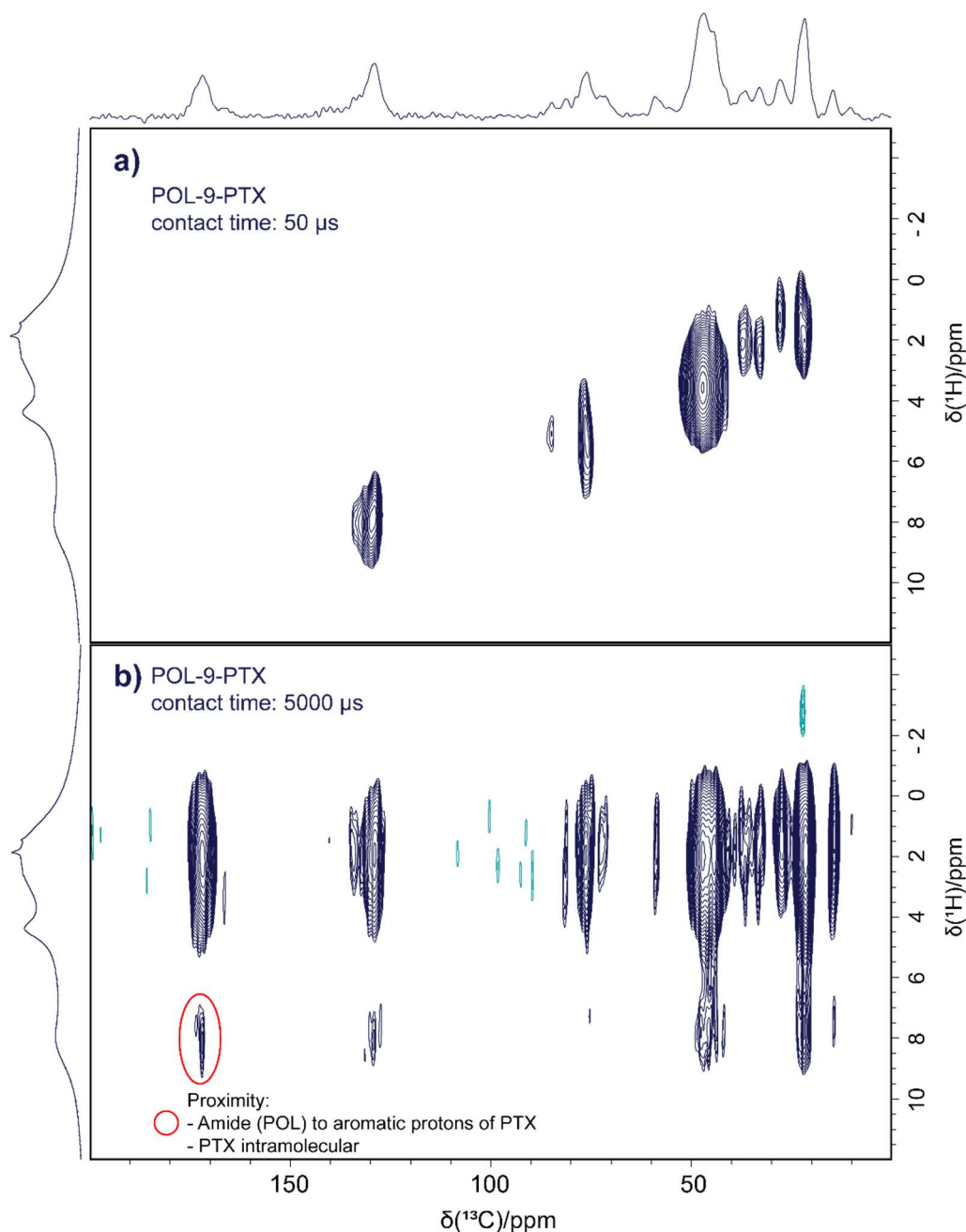
Figure S3: ^{1}H-^{13}C HETCOR MAS spectrum of POL-9-PTX recorded with a 3.2 mm double-channel (^{15}N-^{31}P/^{1}H-^{19}F) MAS probe at 14.1 T and a MAS spinning rate of 20 kHz, using a mixing time of a) $\tau_{mix} = 50\,\mu s$ and b) $\tau_{mix} = 5000\,\mu s$. 100 t_1 FID increments were acquired using a recycle delay of 2.03 s, each with 512 co-added transients. The corresponding ^{1}H one-pulse MAS and ^{13}C CP MAS NMR spectra are shown as external projections.

SI 4: Chemical shifts of the polymer (POL) in solution

This chapter is reprinted with the permission from ref.[1] Copyright 2020 Royal Society of Chemistry. Assignment of the ^{1}H and ^{13}C chemical shifts in solution was done based on a standard set of 1D and 2D NMR experiments including ^{1}H, proton-decoupled ^{13}C, ^{13}C DEPT, ^{1}H-^{1}H COSY, ^{1}H-^{13}C HSQC, and ^{1}H-^{13}C HMBC experiments. In CDCl$_3$, the individual polymer strands do not self-assemble, while in D$_2$O the amphiphilic triblock copolymer forms spherical and wormlike micellar structures. Corresponding ^{13}C and ^{1}H spectra in D$_2$O spectra are shown in **Figures S4** and **S5**, recorded at 311 K to mimic body temperature conditions.

POL

C	CDCl$_3$ [ppm]	D$_2$O [ppm]		H of C	CDCl$_3$ [ppm]	D$_2$O [ppm]
2,3,6,7	48.1-43.7	46.3, 44.2,		**2,3,6,7**	3.49-3.25	3.51-3.47
4,5		47.2, 46.7		**4, 5**		3.63-3.57
13/20	171.5, 170.9	174.3				
14/21	21.3	20.2		**14/21**	2.14-2.08	2.09-2.02
15	174.0, 173.4	Not visible				
16	32.6	32.3		**16**	2.37-2.31,	2.36-2.26
17	27.4	27.3		**17**	1.61-1.53	1.51-1.47
18	22.7	22.0		**18**	1.39-1.30	1.34-1.27
19	14.1	13.3		**19**	0.93-0.90	0.89-0.85

Figure S4: ^{1}H NMR spectrum of pure POL in D_2O recorded with a recycle delay of 5.8 s with 400 co-added transients. The dataset was recorded on a 14.1 T Bruker Avance III HD spectrometer equipped with a 5 mm DCH ^{13}C/^{1}H/^{2}H cryoprobe at 311 K. The temperature was calibrated using 80% ethylene glycol in DMSO-d_6.
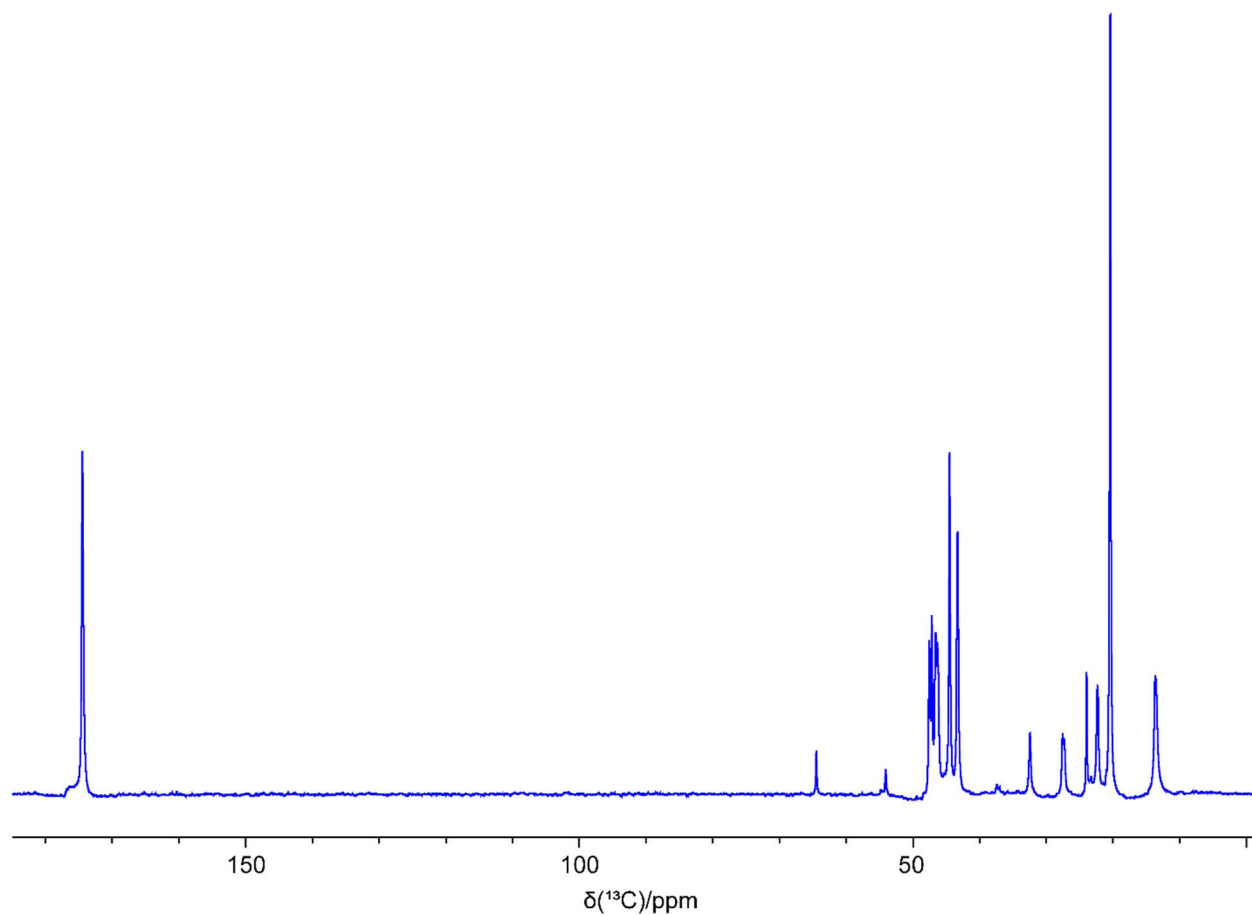
Figure S5: Proton decoupled ^{13}C NMR spectrum of pure POL in D$_2$O recorded with a recycle delay of 2.8 s with 26624 co-added transients. The dataset was recorded on a 14.1 T Bruker Avance III HD spectrometer equipped with a 5 mm DCH ^{13}C/^{1}H/^{2}H cryoprobe at 311 K. The temperature was calibrated using 80% ethylene glycol in DMSO-d$_6$.

For the ^{1}H chemical shift assignment of the solid-state MAS spectra of the pure polymer, NMR data in solution together with ^{1}H-^{1}H NOESY-like solid-state NMR spectra were used.[1]

SI 5: NMR characterization of Paclitaxel (PTX) in solution
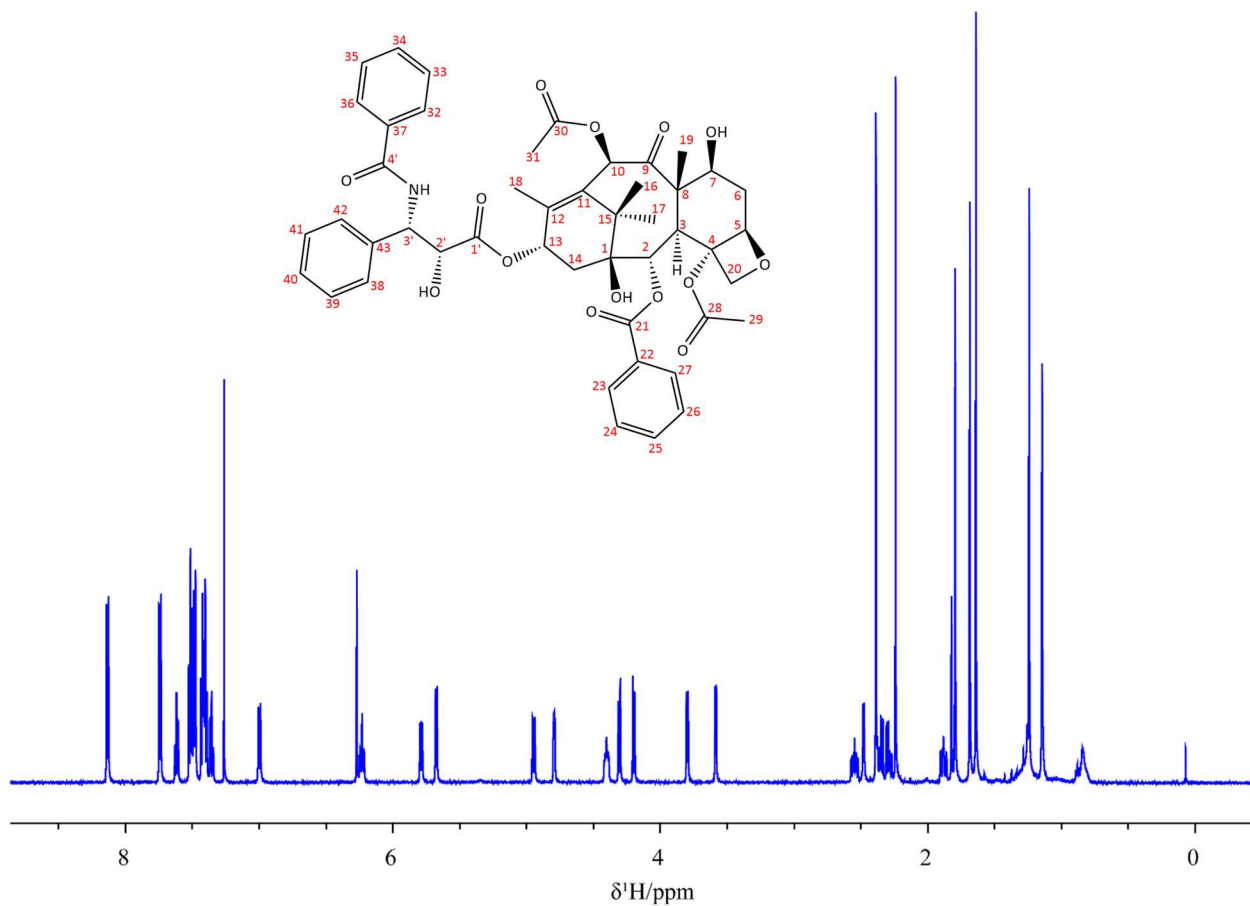
Figure S6: ^{1}H NMR spectrum of pure PTX (as received) in CDCl$_3$, recorded with 16 co-added transients and a recycle delay of 5.8 s. The dataset was recorded on a Bruker Avance III HD 14.1 T spectrometer equipped with a 5 mm BBFO BB/^{1}H/D probe at 295 K. The temperature was calibrated using 4% MeOH in MeOD.
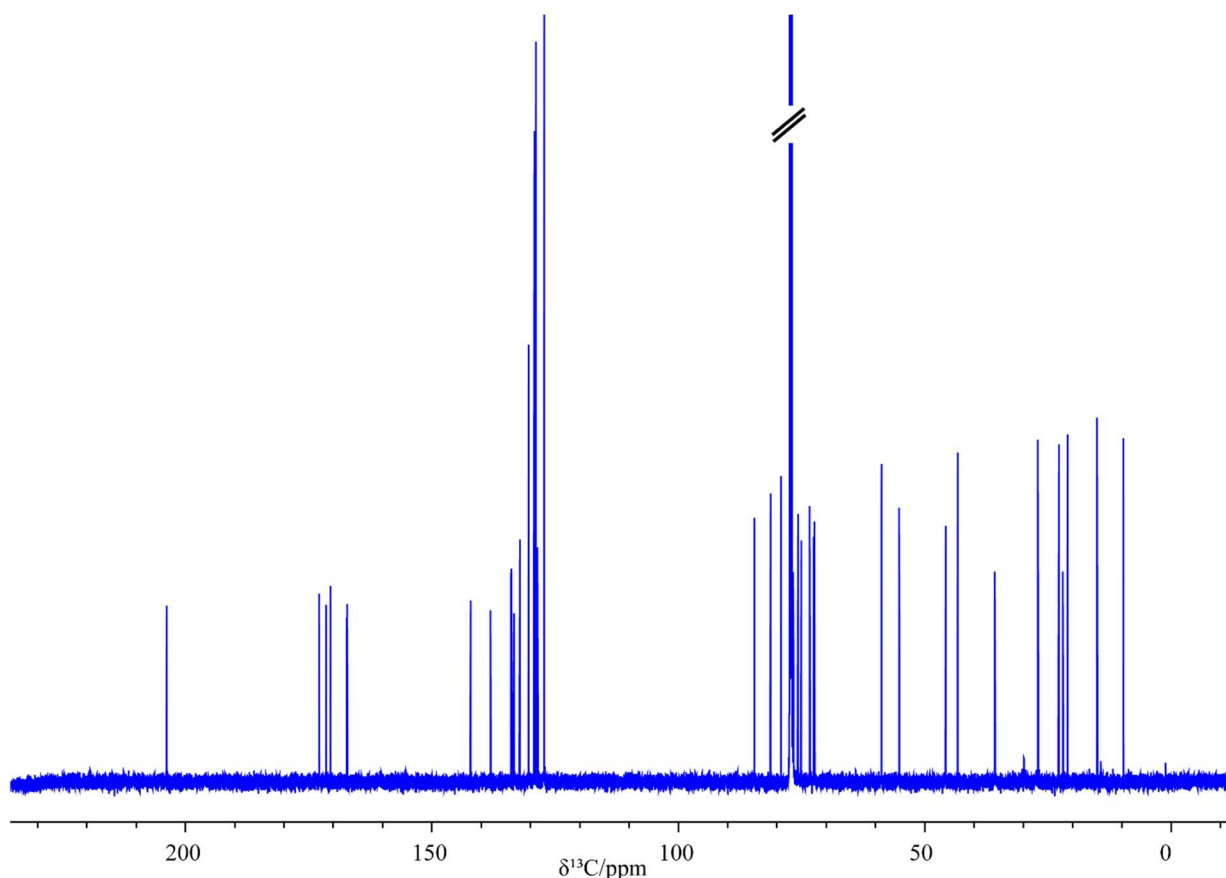
Figure S7: Proton decoupled ^{13}C NMR spectrum of pure PTX (as received) in CDCl$_3$, recorded with 8192 co-added transients and a recycle delay of 2.8 s. The dataset was recorded on a Bruker Avance III HD 14.1 T spectrometer equipped with a 5 mm BBFO BB/^{1}H/D probe at 295 K. The temperature was calibrated using 4% MeOH in MeOD.

Assignment of the ^{1}H and ^{13}C chemical shifts in solution was done based on a standard set of 1D and 2D NMR experiments including ^{1}H, proton-decoupled ^{13}C, ^{1}H-^{1}H COSY, ^{1}H-^{1}H NOESY, ^{1}H-^{13}C HSQC and ^{1}H-^{13}C HMBC experiments in CDCl$_3$. Corresponding ^{1}H and ^{13}C spectra are shown in **Figure S6** and **S7**, recorded at a calibrated temperature of 295 K.

The following ^{1}H NMR assignment for PTX uses the carbon numbering scheme shown above in the way that, for example, C25, indicates the proton bound to carbon C25.

^{1}H-NMR (600.4 MHz, CDCl$_3$): δ = 8.13 (m, 2 H, CH, C23/27 (*o*)), 7.74 (m, 2 H, CH, C33/35 (*m*)), 7.61 (m, 1 H, CH, C25 (*p*)), 7.52-7.47 (m, 5 H, CH, C24/26 (*m*), C34(*p*), C38/42 (*o*)), 7.43-7.40 (m, 4 H, CH, C32/36 (*o*), C39/41 (*m*)), 7.35 (m, 1 H, CH, C40 (*p*)), 6.99 (d, 1 H, NH, $^3J_{C3'-NH}$ = 8.9 Hz, NH). 6.27 (s, 1 H, CH, C10), 6.23 (m, 1 H, CH, C13), 5.79 (dd, 1 H, CH, $^3J_{C2'-C3'}$ = 2.6 Hz, $^3J_{C3'-NH}$ = 8.9 Hz, C3'), 5.67 (d, 1 H, CH, $^3J_{C2-C3}$ = 7.0 Hz, C2), 4.95 (dd, 1 H, CH, $^3J_{C5-C6a}$ = 1.9 Hz, $^3J_{C5-C6e}$ = 9.6 Hz, C5), 4.79 (d, 1 H, CH, $^3J_{C2'-C3'}$ = 2.7 Hz, C2'), 4.40 (dd, 1 H, CH, $^3J_{C7-C6a}$ = 10.9 Hz, $^3J_{C7-C6e}$ = 6.8 Hz, C7), 4.31 (d, 1 H, CH$_2$, $^2J_{C20-C20}$ = 8.5 Hz, C20), 4.19 (d, 1 H, CH$_2$, $^2J_{C20-C20}$ = 8.5 Hz, C20), 3.80 (d, 1 H, CH, $^3J_{C2-C3}$ = 7.0 Hz, C3), 3.57 (s,

3 H, CH$_3$, C2'-OH), 2.59-2.48 (ddd, 1 H, CH, $^2J_{C6a-C6e}$ = 15.0 Hz, $^3J_{C5-C6e}$ = 9.7 Hz, $^3J_{C7-C6e}$ = 6.7 Hz, C6e), 2.47 (s, 1 H, OH, C7-OH), 2.39 (s, 3 H, CH$_3$, C29), 2.35 (dd, 1 H, CH, $^2J_{C14a-C14e}$ = 15.4 Hz, $^3J_{C13-C14e}$ = 9.0 Hz, C14e), 2.28 (dd, 1 H, CH, $^2J_{C14a-C14e}$ = 15.4 Hz, $^3J_{C13-C14a}$ = 9.0 Hz, C14a), 2.24 (s, 3 H, CH$_3$, C31), 1.92-1.85 (ddd, 1 H, CH, $^2J_{C6a-C6e}$ = 14.7 Hz, $^3J_{C5-C6a}$ = 2.3 Hz, $^3J_{C7-C6a}$ = 11.0 Hz, C6a), 1.79 (d, 3 H, CH$_3$, $^4J_{C18-C13}$ = 1.1 Hz, C18), 1.68 (s, 3 H, CH$_3$ C19), 1.24 (s, 3 H, CH$_3$, C16), 1.14 (s, 3 H, CH$_3$, C17) ppm.

^{13}C-NMR (100.6 MHz, CDCl$_3$): δ = 203.8 (1 C, C$_q$, C9), 172.9 (1 C, C$_q$, C1'), 171.4 (1 C, C$_q$, C30), 170.5 (1 C, C$_q$, C28), 167.2 (1 C, C$_q$, C21), 167.2 (1 C, C$_q$, C4'), 142.1 (1 C, C$_q$, C12), 138.1 (2 C, C$_q$, C37/43), 133.9 (1 C, C$_q$, C22), 133.7 (1 C, CH, C25 (*p*)), 133.3 (1 C, C$_q$, C11), 132.1 (1 C, CH, C34 (*p*)), 130.4 (2 C, CH, C23/27 (*o*)), 129.3 (2 C, CH, C38/42 (*o*)), 129.2 (1 C, CH, C39/41 (*m*)), 128.88 (1 C, CH, C39/41 (*m*)), 128.86 (4 C, CH, C24/26 (*m*), C32/36 (*o*)), 128.5 (1 C, CH, C40 (*p*)), 127.2 (2 C, CH, C33/35 (*m*)), 127.2 (2 C, CH, C38/42 (*o*)), 84.6 (1 C, CH, C5), 81.3 (1 C, C$_q$, C4), 79.2 (1 C, C$_q$, C1), 76.7 (1 C, CH$_2$, C20), 75.7 (1 C, CH, C10), 75.1 (1 C, CH, C2), 73.3 (1 C, CH, C2'), 72.5 (1 C, CH, C13), 72.3 (1 C, CH, C7), 58.8 (1 C, C$_q$, C8), 55.2 (1 C, CH, C3'), 45.7 (1 C, CH, C3), 43.3 (1 C, C$_q$, C15), 35.8 (1 C, CH$_2$, C14), 35.7 (1 C, CH$_2$, C6), 27.0 (1 C, CH$_3$, C16a), 22.8 (1 C, CH$_3$, C29), 22.0 (1 C, CH$_3$, C17e), 21.0 (1 C, CH$_3$, C31), 15.0 (1 C, CH$_3$, C18), 9.7 (1 C, CH$_3$, C19) ppm.

SI 6: Aliphatic signals of the ^{13}C CP MAS spectra of all investigated samples
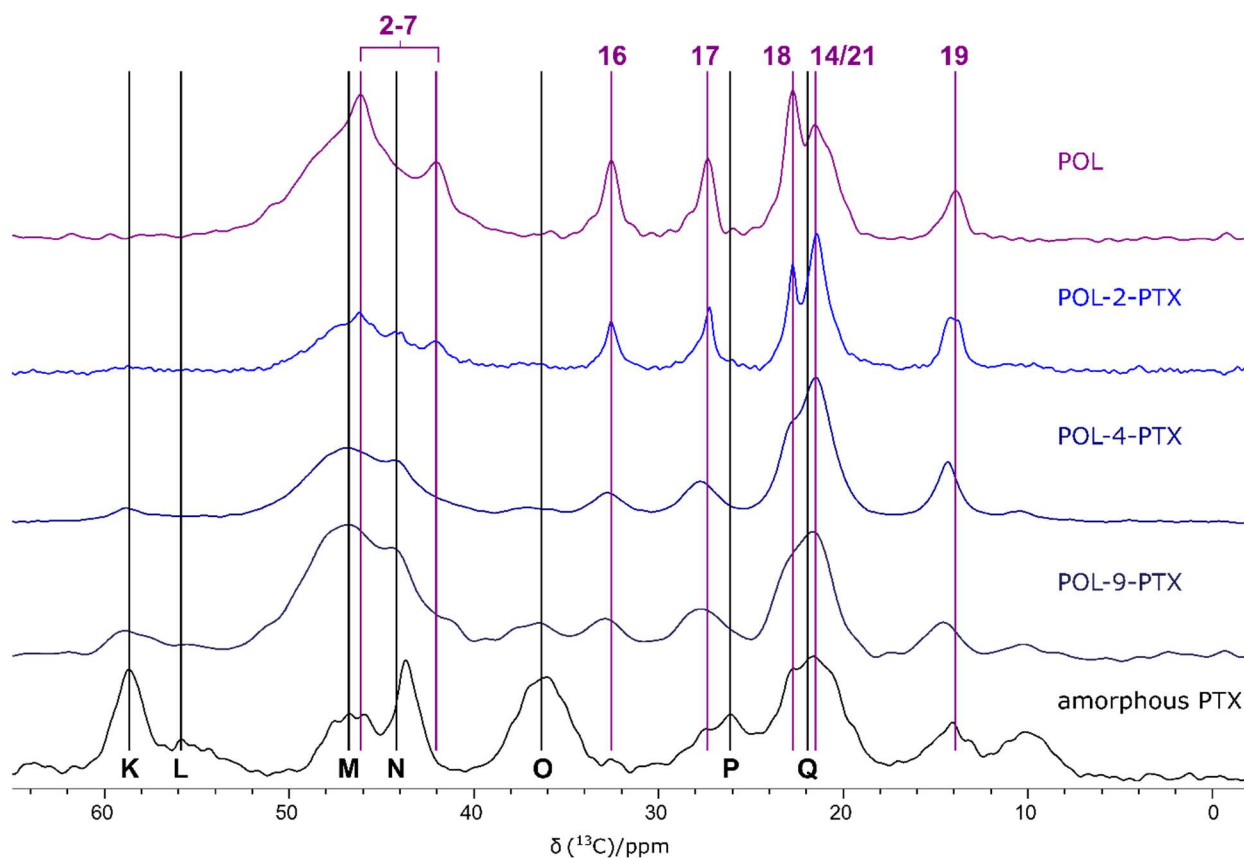
Figure S8: Section of the spectra of Figure 1 of the main manuscript.

SI 7: Mobility Aspects – ^{13}C direct excitation spectra
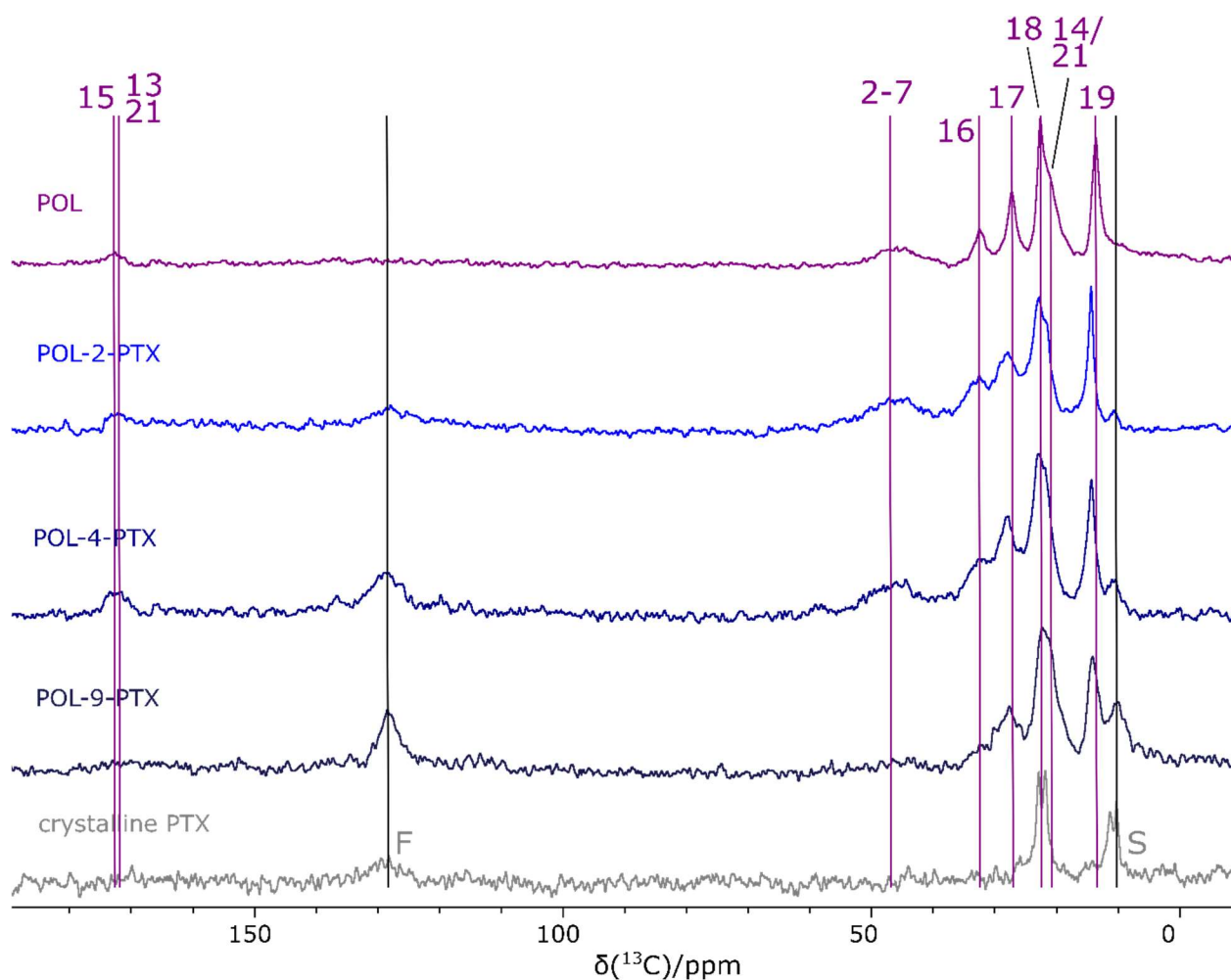
Figure S9: ^{13}C direct excitation MAS NMR spectra of the pure Polymer POL (purple), three differently loaded formulations POL-2-PTX, POL-4-PTX, POL-9-PTX (different blue tones), and crystalline PTX (black). Partial assignment of relevant peaks for the discussion is indicated with numbers belonging to POL signals and capital letters to PTX peak regions. All spectra were recorded at 14.1 T and 24 kHz MAS (except for POL-9-PTX which was spun at 20 kHz), with a recycle delay of 0.8 s and the following number of co-added transients: 17852 (POL), 6144 (POL-2-PTX), 6144 (POL-4-PTX), 7195 (POL-9-PTX).

SI 8: Line broadening with MNOVA

The line broadening (LB) value was chosen based on the ability to pick peaks in the amorphous PTX spectrum, as even small changes in LB resulted in changes in full width at half maximum (FWHM). An LB value of 30 Hz was determined for optimal peak picking with low changes in FWHM.

To determine the FWHM of a signal, the peak position was placed in such a way, that the peak fitting feature in MNOVA could be used to measure FWHM of the signal. As a result, the peak may not be at the highest point of the multiplet as seen in **Figure S10**.
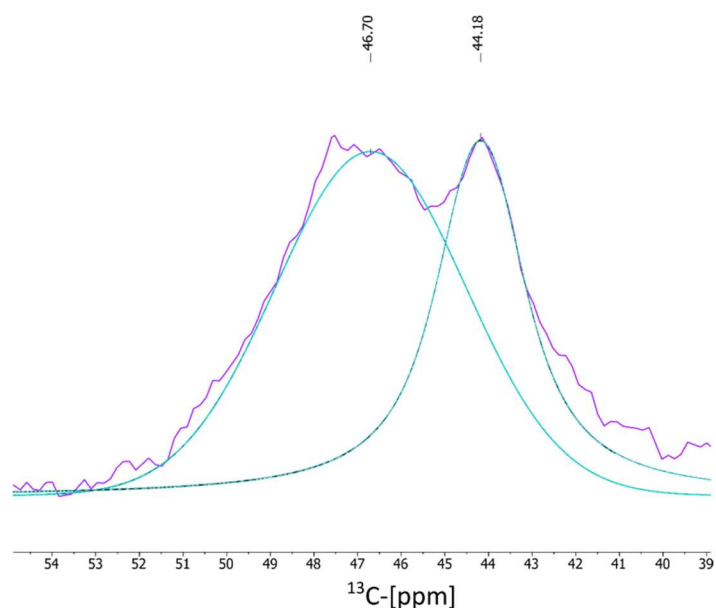
Figure S10: Example of the FWHM measurement using Mestrelab's peak fitting feature. The peak on the right is an example of a fit as used to measure changes in chemical shift. The peak on the left is fitted for use in measurement of change in FWHM.

SI 9: Changes of chemical shift of PTX and POL peaks

Table S1: The table shows changes of the ^{13}C chemical shift for the investigated PTX peaks. Δ is the change of chemical shift between the two samples to the left of each Δ column.

PN	Amorphous PTX	POL-9-PTX	Δ	POL-9-PTX	POL-4-PTX	Δ	POL-4-PTX	POL-2-PTX	Δ	
D	139.7	139.8	0.1	139.8	139.6	-0.2	139.6	140.3	0.8	
E	133.1	133.1	0.0	133.1	134.3	1.2	134.3	132.9	-1.4	
F	128.7	129.1	0.4	129.1	129.5	0.4	129.5	129.1	-0.4	
G	84.6	84.7	0.1	84.7	84.4	-0.3	84.4	85.6	1.2	
H	80.9	81.2	0.3	81.2	81.4	0.2	81.4	81.1	-0.3	Chemical Shift [ppm]
I	76.0	76.2	0.2	76.2	76.4	0.2	76.4	77.1	0.7	
J	72.3	72.0	-0.3	72.0	71.9	-0.1	71.9	71.9	0.0	
K	58.7	58.7	0.0	58.7	58.9	0.2	58.9	58.9	0.0	
N	43.7	44.4	0.7	44.4	44.2	-0.2	44.2	44.1	-0.1	
O	36.3	36.8	0.5	36.8	37.2	0.4	37.2	37.1	-0.1	
R	14.1	14.6	0.5	14.6	14.3	-0.3	14.3	14.2	-0.1	
S	10.2	10.2	0.0	10.2	10.5	0.3	10.5	10.6	0.1	

(Row label at left: Peak Number (PN))

Table S2: The table shows changes of the ^{13}C chemical shift for the investigated POL peaks. Δ is the change of chemical shift between the two samples to the right of each Δ column. The values are listed with a high precision to avoid unnecessary errors in calculations due to rounding.

PN	Δ	POL-9-PTX	POL-4-PTX	Δ	POL-4-PTX	POL-2-PTX	Δ	POL-2-PTX	POL	
16	0.23	33.00	32.77	0.22	32.77	32.55	0.0	32.55	32.55	
17	-0.03	27.71	27.74	0.47	27.74	27.27	-0.05	27.27	27.32	Chemical Shift [ppm]
18	0.30	22.99	22.69	-0.02	22.69	22.71	-0.03	22.71	22.74	
14/21	0.11	21.61	21.50	0.05	21.50	21.45	-0.08	21.45	21.53	
19	0.26	14.59	14.33	0.25	14.33	14.08	0.18	14.08	13.90	

(Row label at left: Peak (PN))

SI 10: Information about investigated PTX and POL peaks

This section lists the results of all the different peak regions of PTX and POL that were used to study the changes in FWHM with MNOVA.

Table S3: The table lists information about the ^{13}C chemical shift (CS) and the Full-Width-Half-Maximum (FWHM) of the investigated peaks (PN) of PTX (letters) and POL (numbers). The values are listed with a high precision to avoid unnecessary errors in calculations due to rounding.

PN	A_PTX			POL-9-PTX			POL-4-PTX			POL-2-PTX			POL		
	CS [ppm]	FWHM [Hz]	FWHM [ppm]	CS [ppm]	FWHM [Hz]	FWHM [ppm]	CS [ppm]	FWHM [Hz]	FWHM [ppm]	CS [ppm]	FWHM [Hz]	FWHM [ppm]	CS [ppm]	FWHM [Hz]	FWHM [ppm]
A	172.9	404.4	2.70												
15				172.0	642.0	4.28	172.3	603.8	4.03	172.4	328.2	2.19	172.4	194.0	1.29
B	170.5	571.7	3.79												
C	167.1	447.8	2.97	166.9	412.5	2.75	166.9	290.1	1.93						
D	139.9	848.9	5.62	140.1	465.7	3.10	140.3	508.1	3.39	140.3	219.7	1.46			
E	132.9	785.7	5.20	133.1	533.0	3.55	134.2	435.6	2.90	132.9	403.5	2.69			
F	128.8	553.2	3.66	129.1	535.0	3.57	129.7	643.6	4.29	129.1	345.9	2.31			
G	84.5	420.6	2.79	84.7	305.0	2.03	84.8	337.5	2.25	85.6	337.5	2.25			
H	80.8	500.2	3.31	81.2	360.0	2.40	81.5	254.6	1.70	81.1	381.7	2.54			
I	76.0	589.1	3.90	76.2	529.0	3.53	76.4	602.0	4.01	77.1	586.2	3.91			
J	72.3	627.8	4.16	72.0	547.0	3.65	72.0	664.3	4.43	72.5	477.5	3.18			
K	58.6	312.8	2.07	58.7	350.0	2.33	58.8	245.5	1.64	58.5	302.4	2.02			
L	55.8	741.6	4.91												
M	46.5	554.3	3.67	47.0	675.0	4.50	46.8	790.3	5.27						
2-7										46.5	506.4	3.38	46.2	571.4	3.81
N	43.7	219.8	1.46	44.4	487.0	3.25	44.2	403.2	2.69	44.3	346.1	2.31			
										42.2	264.4	1.76	42.1	267.8	1.79
O	36.3	496.2	3.29	36.8	520.0	3.47	36.9	583.0	3.89	37.1	399.7	2.66			
16				33.0	388.0	2.59	32.8	342.8	2.29	32.6	128.6	0.86	32.6	147.2	0.98
17				22.7	466.0	3.11	27.8	339.4	2.26	27.4	131.5	0.88	27.3	137.8	0.92
P	26.1	740.3	4.90												
18							22.8	236.1	1.57	22.7	114.3	0.76	22.7	177.1	1.18
Q	21.8	582.8	3.86	21.6	356.0	2.37									
14/21							21.5	284.9	1.90	21.4	219.9	1.47	21.5	331.7	2.21
R	14.2	463.4	3.07	14.6	266.0	1.77	14.3	178.9	1.19	14.1	191.4	1.28			
19													13.9	162.6	1.08
S	10.2	439.2	2.91	10.2	214.0	1.43	10.5	273.4	1.82	10.6	467.7	3.12			

SI 11: References

[1]   M. Grüne, R. Luxenhofer, D. Iuga, S. P. Brown, A.-C. Pöppler, *J. Mater. Chem. B* **2020**, *8*, 6827-6836.

Summary and outlook

Paclitaxel (PTX) is one of the leading drugs against breast and ovarian cancer. Due to its low solubility, treatment of the patients with this drug requires a very well-suited combination with a soluble pharmaceutical excipient to increase the bioavailability and reduce the strong side effects. One efficient way to achieve this in the future could be the incorporation of PTX into polymeric micelles composed of poly(2-oxazoline) based triblock copolymers (POL) which enables PTX loadings of up to 50 wt.%. However, structural information at an atomic level and thus the knowledge of interaction sites within these promising but complex PTX-POL formulations were not yet available. Such results could support the future development of improved excipients for PTX and suitable excipients for other pharmaceutical drugs. Therefore, a solid-state MAS NMR investigation of these amorphous formulations with different POL-PTX compositions was performed in this thesis as this gives insights of the local structure at an atomic level in its solid state. NMR in solution showed very broad ^{13}C signals of PTX for this system due to the reduced mobility of the incorporated drug which exclude this as an analytical method.

In a first study, crystalline PTX was structurally characterized by solid-state NMR as no complete ^{13}C spectrum assignment and no ^{1}H NMR data existed for the solid state. In addition, the asymmetric unit of the PTX crystal structure consists of two molecules (Z'=2) that can only be investigated in its solid state. As crystalline PTX in total has about 100 different ^{13}C and ^{1}H chemical shifts with very small differences due to Z'=2, and furthermore, its unit cell consisting of more than 900 atoms, accompanying GIPAW (CASTEP) calculations were required for NMR signal assignments. These calculations were performed using the first three available purely hydrous and anhydrous PTX structures, which were determined by XRD and published by Vella-Zarb et al. in 2013.[1] Within this thesis, is was discovered that two investigated batches of commercially available PTX from the same supplier both contained an identical and so far unknown PTX phase that was elucidated by PXRD as well as solid-state NMR data. One of the two batches consists of an additional phase that was shown to be very similar to a known hydrated phase published in 2013.[1] By heating the batch with the mixture of the two phases under vacuum, it is transformed completely to the new dry phase occurring in both PTX batches. Since the drying conditions to obtain anhydrous PTX in-situ on the PXRD setup described by Vella-Zarb et. al.[1] were much softer than ours, we identify our dry phase as a relaxed version of their published anhydrate structure. The PXRD data of the new anhydrate phase was transferred into a new structural model, which currently undergoes geometry optimization. Based on solid-state NMR data at MAS spinning frequencies up to 100 kHz, a ^{13}C and a partial ^{1}H signal assignment for the new anhydrous structure were

achieved. These results provided sufficient structural information for further investigations of the micellar POL-PTX system.

In a second study, the applicability and benefit of two-dimensional solid-state ^{14}N-^{1}H HMQC MAS NMR spectra[2] for the characterization of amorphous POL-PTX formulations was investigated. The mentioned technique has never been applied to a system of similar complexity before and was chosen because around 84% of the small-molecule drugs contain at least one nitrogen atom. In addition, the number of nitrogen atoms in both POL and PTX is much smaller than the number of carbons or hydrogens, which significantly reduces the spectral complexity. ^{14}N has a natural abundance of 99.6% but leads to quadrupolar broadening due to its nuclear spin quantum number $I = 1$. While this is usually undesirable due to broadening in the resulting 1D ^{14}N NMR spectra, this effect is explicitly used in the 2D ^{14}N-^{1}H HMQC MAS experiment. The indirect ^{14}N measurement can avoid the broadening while maintaining the advantage of the high natural abundance and making use of the much more dispersed signals due to the additional quadrupolar shifts as compared to ^{15}N.

This measurement method could be successfully applied to the complex amorphous POL-PTX mixtures. With increasing PTX loading of the formulations, additional peaks arise as spatial proximities of the amide nitrogens of POL to NH or OH groups of PTX. In addition, the ^{14}N quadrupolar shift of these amide nitrogens decreases with increasing PTX content indicating a more symmetric nitrogen environment. The latter can be explained by a transformation of the trigonal planar coordination of the tertiary amide nitrogen atoms in pure POL towards a more tetrahedral environment upon PTX loading induced by the formation of hydrogen bonds with NH/OH groups of PTX.

In the third and last project, the results of the two abovementioned studies were used and extended by solid state ^{13}C and two-dimensional ^{1}H-^{13}C as well as ^{1}H-^{1}H MAS NMR data with the aim to derive a structural model of the POL-PTX formulations at an atomic level. The knowledge of the NMR signal assignments for crystalline PTX was transferred to amorphous PTX (present in the micelles of the formulations). The ^{13}C solid-state NMR signals were evaluated concerning changes in chemical shifts and full widths of half maximum (FWHM) for the different PTX loadings. In this way, the required information about possible interaction sites at an atomic level becomes available. Due to the complexity of these systems, such proximities often cannot be assigned to special atoms, but more to groups of atoms, as the individual developments of line widths and line shifts are mutually dependent. An advantageous aspect for this analysis was that pure POL already forms unloaded micelles. The evaluation of the data showed that the terminal phenyl groups of PTX seem to be most involved in the interaction by the establishment of the micelle for lowest drug loading and that they are likely

to react to the change in the amount of PTX molecules as well. For the incorporation of PTX in the micelles, the following model could be obtained: For lowest drug loading, PTX is mainly located in the inner part of the micelles. Upon further increasing of the loading, it progressively extends toward the micellar shell. This could be well shown by the increasing interactions of the hydrophobic butyl chain of POL and PTX, proceeding in the direction of the polymer backbone with rising drug load. Furthermore, due to the size of PTX and the hydrodynamic radius of the micelles, even at the lowest loading, the PTX molecules partially reach the core-shell interface of the micelle. Upon increasing the drug loading, the surface coverage with PTX clusters increases based on the obtained model approach. The latter result is supported by DLS and SANS data of this system.[3] The abovementioned results of the [14]N-^{1}H HMQC MAS investigation of the POL-PTX formulations support the outlined model.

As an outlook, the currently running geometry optimization and subsequently scheduled calculation of the chemical shieldings of the newly obtained anhydrous PTX crystal structure can further improve the solid-state NMR characterization through determination of further spatial proximities among protons using the existing 2D [1]H(DQ)-[1]H(SQ) solid-state MAS NMR spectrum at 100 kHz rotor spinning frequency. The 2D [14]N-^{1}H HMQC MAS NMR experiments were shown to have great potential as a technique for the analysis of other disordered and amorphous drug delivery systems as well. The results of this thesis should be subsequently applied to other micellar systems with varying pharmaceutical excipients or active ingredients with the goal of systematically achieving higher drug loadings (e.g., for the investigated PTX, the similar drug docetaxel or even different natural products). Additionally, it is planned to transfer the knowledge to another complex polymer system containing poly(amino acids) which offers hydrogen bonding donor sites for additional intermolecular interactions. Currently, the POL-PTX system is investigated by further SANS studies that may provide another puzzle piece to the model as complementary measurement method in the future. In addition, the use of MD simulations might be considered in the future. This would allow a computerized linking of the different pieces of information with the aim to determine the most likely model.

References

[1] L. Vella-Zarb, U. Baisch, R. E. Dinnebier, *J. Pharm. Sci.* **2013**, *102*, 674-683.

[2] A. S. Tatton, J. P. Bradley, D. Iuga, S. P. Brown, *Z. Phys. Chem.* **2012**, *226*, 1187-1204.

[3] A. Schulz, S. Jaksch, R. Schubel, E. Wegener, Z. Di, Y. Han, A. Meister, J. Kressler, A. V. Kabanov, R. Luxenhofer, *ACS nano* **2014**, *8*, 2686-2696.

Zusammenfassung und Ausblick

Paclitaxel (PTX) ist eines der führenden Medikamente gegen Brust- und Eierstockkrebs. Aufgrund seiner geringen Löslichkeit erfordert die Behandlung der Patienten mit diesem Medikament eine sehr gut geeignete Kombination mit einem löslichen pharmazeutischen Hilfsstoff, um die Bioverfügbarkeit zu erhöhen und die starken Nebenwirkungen zu reduzieren. Ein effizienter Weg, dies in Zukunft zu erreichen, könnte der Einbau von PTX in polymere Mizellen sein, die aus Poly(2-oxazolin)-basierten Triblock-Copolymeren (POL) bestehen und PTX-Beladungen von bis zu 50 Gew.-% ermöglichen. Strukturelle Informationen auf atomarer Ebene und damit die Kenntnis von Wechselwirkungen innerhalb dieser vielversprechenden, aber komplexen PTX-POL-Formulierungen waren jedoch bisher nicht verfügbar. Solche Ergebnisse könnten die zukünftige Entwicklung von verbesserten Hilfsstoffen für PTX und von geeigneten Hilfsstoffen für andere pharmazeutische Wirkstoffe unterstützen. Aus diesem Grund wurden in der vorliegenden Dissertation Festkörper-NMR-Untersuchungen an diesen amorphen Formulierungen mit unterschiedlichen POL-PTX Zusammensetzungen durchgeführt, weil damit Einblicke in die lokale Struktur auf atomarer Ebene im festen Zustand erhalten werden können. Aufgrund der verringerten Mobilität des eingebrachten Wirkstoffs in diesem System ergeben NMR-Messungen in Lösung sehr breite ^{13}C-PTX-Signale, was diese Technik als Analysemethode ausschließt.

In einer ersten Studie wurde kristallines PTX mittels Festkörper-NMR charakterisiert, da keine vollständige ^{13}C-Zuordnung des Spektrums sowie keine ^{1}H-NMR-Daten für den festen Zustand dieser Struktur vorlagen. Zudem besteht die asymmetrische Einheit der PTX-Kristallstruktur aus zwei Molekülen (Z'=2), die nur im festen Zustand untersucht werden kann. Da das kristalline PTX insgesamt ca. 100 verschiedene ^{13}C und ^{1}H chemische Verschiebungen aufweist, die sich aufgrund von Z'=2 nur sehr geringfügig unterscheiden, und außerdem seine Einheitszelle aus mehr als 900 Atomen besteht, waren begleitende GIPAW (CASTEP)-Rechnungen für NMR-Signalzuordnungen erforderlich. Diese Berechnungen wurden mit den ersten drei verfügbaren PTX-Strukturen durchgeführt, die nur Wasser als zusätzliche eingelagerte Komponente enthalten bzw. wasserfrei sind. Sie wurden durch XRD bestimmt und von Vella-Zarb et al. 2013 veröffentlicht.[1] Im Rahmen der vorliegenden Dissertation wurde herausgefunden, dass zwei untersuchte Chargen von kommerziell verfügbarem PTX desselben Lieferanten eine identische und bisher unbekannte PTX-Phase enthalten, die durch PXRD- sowie Festkörper-NMR-Daten aufgeklärt wurde. Eine der beiden Chargen besteht aus einer zusätzlichen Phase, bei der sich eine große Ähnlichkeit zu einer bekannten, 2013 publizierten Hydratphase ergeben hat.[1] Durch Erhitzen unter Vakuum der Charge, die das Gemisch der beiden Phasen enthält, wird diese vollständig in die neue, trockene Phase umgewandelt, die in beiden PTX-

Chargen enthalten ist. Da die Trocknungsbedingungen, um wasserfreies PTX in-situ mit dem von Vella-Zarb et al.[1] beschriebenen PXRD-Setup zu erhalten, weniger intensiv waren als unsere, identifizieren wir unsere Phase als eine relaxierte Version ihrer veröffentlichten Anhydratstruktur. Anhand von PXRD-Daten der neuen wasserfreien Phase wurde eine neue Kristallstruktur ermittelt, die derzeit noch geometrieoptimiert wird. Basierend auf Festkörper-NMR-Daten bei MAS-Rotationsfrequenzen bis zu 100 kHz wurden eine ^{13}C- und eine partielle ^{1}H-Signalzuordnung für die neue wasserfreie Struktur ermittelt. Diese Ergebnisse lieferten ausreichende strukturelle Informationen für darüber hinausgehende Untersuchungen des mizellaren POL-PTX-Systems.

In einer zweiten Studie wurde die Anwendbarkeit und die Aussagekraft von zweidimensionalen ^{14}N-^{1}H-HMQC-MAS-NMR-Spektren[2] im festen Aggregatszustand für die Charakterisierung von amorphen POL-PTX Formulierungen untersucht. Die genannte Messmethode wurde bisher noch nie auf ein System ähnlicher Komplexität angewandt und wurde ausgewählt, weil etwa 84 % der niedermolekularen Arzneimittel mindestens ein Stickstoffatom enthalten. Darüber hinaus ist die Anzahl der Stickstoffatome sowohl in POL als auch in PTX wesentlich geringer als die Anzahl der Kohlenstoffe oder Wasserstoffe, was die spektrale Komplexität deutlich reduziert. ^{14}N hat eine natürliche Häufigkeit von 99,6 %, führt aber aufgrund seiner Kerndrehimpuls-Quantenzahl $I = 1$ zu quadrupolarer Verbreiterung. Während Letztere in den resultierenden 1D-^{14}N-NMR-Spektren i. Allg. unerwünscht ist, wird dieser Effekt im 2D-^{14}N-^{1}H-HMQC-MAS-Experiment explizit genutzt. Durch die indirekte ^{14}N-Messung kann die Verbreiterung vermieden werden, wobei der Vorteil der hohen natürlichen Häufigkeit erhalten bleibt. Darüber hinaus führt die für ^{14}N zusätzlich vorliegende quadrupolare Verschiebung im Vergleich zu ^{15}N zu einer wesentlich erhöhten Dispersion der Signale.

Diese Messmethode konnte erfolgreich auf die komplexen amorphen POL-PTX-Systeme angewendet werden. Mit zunehmender PTX-Beladung der Formulierungen entstehen zusätzliche Kreuzsignale, die räumlichen Nähe der Amid-Stickstoffe des Polymers zu den NH- oder OH-Gruppen des PTX anzeigen. Darüber hinaus nimmt die ^{14}N-Quadrupolverschiebung dieser Amid-Stickstoffe mit zunehmendem PTX-Gehalt ab, was auf eine symmetrischere Stickstoffumgebung hinweist. Letzteres lässt sich durch eine Umwandlung der trigonal-planaren Koordination der tertiären Amid-Stickstoffatome in reinem POL in eine eher tetraedrische Umgebung bei PTX-Beladung erklären, die durch die Bildung von Wasserstoffbrückenbindungen mit NH/OH-Gruppen des PTX induziert wird.

Im dritten und letzten Projekt wurden die Ergebnisse der beiden oben genannten Studien verwendet und um ^{13}C-, zweidimensionale ^{1}H-^{13}C- sowie ^{1}H-^{1}H-Festkörper-MAS-NMR-Daten erweitert mit dem Ziel, ein Strukturmodell der POL-PTX-Formulierungen auf atomarer Ebene zu

ermitteln. Die Kenntnis der NMR-Signalzuordnungen für kristallines PTX wurde auf amorphes PTX (liegt in den Mizellen der Formulierungen vor) übertragen. Die ^{13}C-Festkörper-NMR-Signale wurden hinsichtlich der Änderungen der chemischen Verschiebungen und der Halbwertsbreiten (FWHM) für die verschiedenen PTX-Beladungen ausgewertet. Auf diese Weise werden die benötigten Informationen über mögliche Wechselwirkungsstellen auf atomarer Ebene zugänglich. Aufgrund der Komplexität dieser Systeme kann so ermittelte räumliche Nähe oft nicht einzelnen Atomen, sondern eher Gruppen von Atomen zugeordnet werden, da sich die individuellen Entwicklungen der Linienbreiten und Signalverschiebungen gegenseitig bedingen. Es erwies sich als vorteilhaft für diese Analyse, dass reines POL bereits unbeladene Mizellen bildet. Die Auswertung der Daten ergab, dass die terminalen Phenylgruppen des PTX bei der Formulierung der Mizelle bei geringster Wirkstoffbeladung am stärksten an der Wechselwirkung beteiligt zu sein scheinen und auch bevorzugt auf die Veränderung des PTX-Anteils reagieren. Für die Einlagerung von PTX in die Mizellen konnte schließlich folgendes Modell aufgestellt werden: Bei geringer Wirkstoffbeladung befindet sich PTX hauptsächlich im inneren Teil der Mizellen. Mit weiterer Erhöhung der Beladung breitet es sich zunehmend in Richtung der Schalen der Mizellen aus. Letzteres konnte gut durch die zunehmenden Wechselwirkungen der hydrophoben Butylkette von POL mit PTX gezeigt werden, die mit steigender Wirkstoffbeladung in Richtung des Polymerrückgrats stärker wurden. Außerdem erreichen die PTX-Moleküle aufgrund ihrer Größe und des hydrodynamischen Radius der Mizellen selbst bei der geringsten Beladung teilweise die Kern-Schale-Grenzfläche der Mizelle. Bei Erhöhung der Wirkstoffbeladung nimmt die Oberflächenbedeckung mit PTX-Clustern basierend auf dem erhaltenen Modell zu. Das letztere Ergebnis wird durch DLS- und SANS-Daten dieses Systems unterstützt.[3] Die oben genannten Ergebnisse der ^{14}N-^{1}H-HMQC-MAS-Untersuchung der POL-PTX-Formulierungen unterstützen das skizzierte Modell ebenso.

Als Ausblick können die derzeit laufende Geometrieoptimierung und die anschließend geplante Berechnung der chemischen Abschirmungen der neu erhaltenen wasserfreien PTX-Kristallstruktur die Festkörper-NMR-Charakterisierung durch die Bestimmung weiterer Protonen in räumlicher Nähe unter Verwendung des vorliegenden 2D-^{1}H(DQ)-^{1}H(SQ)-Festkörper-MAS-NMR-Spektrums bei 100 kHz MAS-Rotationsfrequenz weiter verbessern. Es konnte gezeigt werden, dass die 2D-^{14}N-^{1}H-HMQC-MAS-NMR-Experimente ein großes Potential als Methode für die Charakterisierung auch anderer ungeordneter und amorpher Wirkstoffsysteme haben. Die Ergebnisse dieser Arbeit sollen daher auf andere mizellare Systeme mit variierenden pharmazeutischen Hilfsstoffen oder Wirkstoffen angewendet werden mit dem Ziel, systematisch höhere Beladungen zu erreichen (z.B. für das untersuchte PTX, das ähnliche Medikament Docetaxel oder auch verschiedene Naturstoffe). Zusätzlich ist geplant, die Erkenntnisse auf ein weiteres komplexes Polymersystem aus Poly-Aminosäuren zu übertragen, das

Wasserstoffbrücken-Donatoren für zusätzliche intermolekulare Wechselwirkungen bietet. Derzeit wird das POL-PTX-System durch zusätzliche SANS-Studien untersucht, die in Zukunft als ergänzende Messmethode weitere Details zum Modell liefern könnten. Darüber hinaus wird die Durchführung von MD-Simulationen in Erwägung gezogen. Dies würde eine computergestützte Verknüpfung der verschiedenen Informationen ermöglichen mit dem Ziel, das wahrscheinlichste Modell zu ermitteln.

References

[1]   L. Vella-Zarb, U. Baisch, R. E. Dinnebier, *J. Pharm. Sci.* **2013**, *102*, 674-683.

[2]   A. S. Tatton, J. P. Bradley, D. Iuga, S. P. Brown, *Z. Phys. Chem.* **2012**, *226*, 1187-1204.

[3]   A. Schulz, S. Jaksch, R. Schubel, E. Wegener, Z. Di, Y. Han, A. Meister, J. Kressler, A. V. Kabanov, R. Luxenhofer, *ACS nano* **2014**, *8*, 2686-2696.

Erklärung

Die vorliegende Arbeit wurde unter der wissenschaftlichen Betreuung von Jun.-Prof. Dr. Ann-Christin Pöppler von April 2017 bis Dezember 2020 an der Fakultät für Chemie und Pharmazie der Julius-Maximilians-Universität Würzburg angefertigt.

Hiermit versichere ich, dass ich die vorliegende Arbeit ohne unzulässige Hilfe Dritter und ohne Benutzung anderer als der angegebenen Hilfsmittel angefertigt habe. Die aus fremden Quellen direkt oder indirekt übernommenen Gedanken sind als solche kenntlich gemacht. Die Arbeit wurde bisher weder im Inland noch im Ausland in gleicher oder ähnlicher Form einer anderen Prüfungsbehörde vorgelegt.

Würzburg, den 21.12.2020

Marvin Grüne

Eigenanteil

"^{14}N-^{1}H HMQC solid-state NMR as a powerful tool to study amorphous formulations – an exemplary study of paclitaxel loaded polymer micelles"

Marvin Grüne*, Robert Luxenhofer, Dinu Iuga, Steven P. Brown, and Ann-Christin Pöppler[†]
J. Mater. Chem. B, **2020**, *8*, 6827-6836

Autor 1 (M. G.), Autor 2 (R. L.), Autor 3 (D. I.), Autor 4 (S. P. B.), Autor 5 (A.-C. P.)						
Autor	**A1**	**A2**	**A3**	**A4**	**A5**	∑ in Prozent
NMR experiments	7		2	1	5	15
Data analysis and interpretation	28		2		10	40
Manuscript planning	5				5	10
Manuscript writing	20			2	5	27
Correction of manuscript	2	1	1	1	3	8
Sum	**62**	**1**	**5**	**4**	**28**	**100**

"New anhydrous crystalline phase of paclitaxel revealed by solid-state NMR spectroscopy, powder X-ray diffraction and complementary quantum chemical calculations"

Marvin Grüne*, Dominik Heuler, Klaus Müller-Buschbaum, and Ann-Christin Pöppler[†]
Unpublished manuscript

Autor 1 (M. G.), Autor 2 (D. H.), Autor 3 (K. M.-B.), Autor 4 (A.-C. P.)					
Autor	**A1**	**A2**	**A3**	**A4**	**∑ in Prozent**
NMR experiments performance	4			3	7
PXRD experiments performance	1	4			5
CASTEP calculations	10				10
Data analysis and interpretation of NMR experiments	30			8	38
Data analysis and interpretation of PXRD experiments	2	3			5
Manuscript planning	3			2	5
Manuscript writing	10	2		8	20
Correction of manuscript	2		3	5	10
Sum	**62**	**9**	**3**	**26**	**100**

"Insights into the loading-dependent assembly of poly(2-oxazoline) based paclitaxel formulations using solid-state NMR spectroscopy"

Marvin Grüne*, Stefanie Klisch, Michael Lübtow, Robert Luxenhofer, and Ann-Christin Pöppler[†]
Unpublished manuscript

Autor 1 (M. G.), Autor 2 (S. K.), Autor 3 (M. L.), Autor 4 (R. L.), Autor 5 (A.-C. P.)						
Autor	**A1**	**A2**	**A3**	**A4**	**A5**	**∑ in Prozent**
Preparation of formulations			2			2
NMR experiments performance	8					8
Data analysis and interpretation of NMR experiments	45	10		5	10	70
Manuscript writing	15					15
Correction of thesis chapter	2				3	5
Sum	**70**	**10**	**2**	**5**	**13**	**100**

"Geometrical and Structural Dynamics of Imatinib within Biorelevant Colloids"

Johannes Wiest*, Marco Saedtler, Bettina Böttcher, Marvin Grüne, Maude Reggane, Bruno Galli, Ulrike Holzgrabe, and Lorenz Meinel[†]
Mol. Pharmaceutics **2018,** *15(10)*, 4470-4480

Autor 1 (J. W.), Autor 2 (M. S.), Autor 3 (B. B.), Autor 4 (M. G.), Autor 5 (M. R.), Autor 6 (B. G.), Autor 7 (U. H.), Autor 8 (L. M.)								
Autor	**A1**	**A2**	**A3**	**A4**	**A5**	**A6**	**A7**	**A8**
Preparation of imatinib free base	X	X						
DOSY NMR measurements				X				
NOESY NMR measurements	X							
Aggregation assay	X							
Solubility measurements		X						
X-Ray powder diffractometry	X	X						
Dynamic light scattering measurements	X	X						
Cryo-electron microscopy			X					
Study design/concept development	X	X						X
Data analysis and interpretation	X	X			X	X	X	X
Manuscript planning	X						X	X
Manuscript writing	X	X			X	X	X	X
Correction of manuscript	X	X						X